

Nonlinear Control Design and Stability Analysis of Power Inverters in Modern Smart Grids

by

Seyfullah Dedeoglu



The
University
Of
Sheffield.

A thesis submitted in partial fulfillment of the requirements for the
degree of Doctor of Philosophy

The University of Sheffield
Faculty of Engineering
Department of Automatic Control and Systems Engineering

November 2021

Acknowledgments

First of all, I would like to express my sincerest gratitude to my supervisor Dr. George C. Konstantopoulos for accepting me in his research group and giving me the opportunity to study in this excellent university and city. Without his continuous guidance, assistance, support, invaluable and encouraging advices throughout my PhD, it would have not been possible to complete this research. I am indebted to him not only for helping me to improve all aspects of my academic skills, but also giving me priceless life advices that will guide me through my entire life.

I want to thank my fellow research group members Dr. Alexandros G. Paspatis, Dr. Andrei-Constantin Braitor, and Mr. Panagiotis Skentzos for their collaboration in experimental studies, and Dr. Pablo R. Baldivieso-Monasterios, Mr. Fernando Genis Mendoza, and Mr. Grigoris Michos for their valuable contributions in our group discussions and journal club meetings. I also offer my thanks to Mr. Jack Powell for helping me in the designs of experimental benches.

Furthermore, I would like to thank Prof. Hasan Komurcugil for the productive collaboration and his valuable guidance.

I would also like to offer my deepest appreciations to my wife Pinyi for her unconditional love, support, and company even in the insufferable times.

Last but not least, I am thankful to the Republic of Turkey Minister of National Education for giving me the invaluable opportunity to complete my MSc and PhD educations in this great university. I would also appreciate my family for their endless support and care in my entire life.

At the end, I want to quote a sentence that helps me try to understand the meaning of life from Mevlana Jalaladdin Rumi:

“Yesterday I was clever, so I wanted to change the world. Today I am wise, so I am changing myself.”

Abstract

Due to environmental concerns, the rise of renewable energy units is causing a paradigm change in the modern electric power system since bulky synchronous generators are being replaced by power electronic converters whose control algorithms are flexible but have low or no inertia. The inertia is a key concept for the power systems as it ensures frequency stability by balancing the generated and consumed power in case of system disturbances. To deal with the inertia problem in power electronic converters, research efforts have led to the formation of various control algorithms, such as droop control, virtual synchronous control, synchronverter, and virtual oscillator control. In addition, since the number of active players involved in power production significantly increases, system stability is another critical issue that should be considered for seamless power converter-based operations. Furthermore, power electronic converters are composed of semiconductor switches, which can be damaged if sudden changes, such as grid voltage sags and short-circuits, occur in the system. Therefore, advanced controllers are required to protect the power converter devices by limiting the key system states, i.e., currents and voltages, without increasing the total system cost.

In this thesis, the main aims are to propose novel nonlinear control algorithms that can ensure reliable operation of grid-connected inverter-fed units and microgrids via system state limitation without additional protection schemes for both single and parallel-connected three-phase inverters, investigate the system stability, and provide the analytic stability conditions that can guide the prospective designers. The proposed controllers are tested both in grid-connected and stand-alone modes for power inverter and microgrid systems considering several system faults including voltage sags and short-circuits. Initially, for the three-phase grid-connected inverters, inverter current limitation is achieved by embedding droop control dynamics into both nonlinear bounded integral controller (BIC) and state-limiting PI (sl-PI) controllers, the closed-loop system stability is examined, and the analytic stability conditions are provided. Furthermore, an improved virtual synchronous control structure is proposed by coupling DC-link voltage and AC frequency dynamics and applied to three-phase

grid-connected inverters. Finally, a nonlinear droop controller that can guarantee the current-limiting property and avoid the undesired circulating current issue in AC microgrids with parallel three-phase inverters is designed. The performances of proposed controllers are verified via simulation, experimental and hardware-in-the-loop studies considering both grid-connected and stand-alone modes. In all of the above cases, the proposed controllers are directly compared with the state-of-the-art control methods under both normal and abnormal (faulty) grid conditions to highlight the advantages of the proposed control frameworks in practice, in addition to the rigorous stability analysis.

Keywords: Nonlinear control, three-phase inverters, droop control, current limitation, stability analysis, virtual synchronous control, DC-link voltage control, grid faults, microgrids, circulating current, parallel inverter operation, grid-connected state, stand-alone state.

Contents

Acknowledgments	i
Abstract	iii
Contents	ix
1 Introduction	1
1.1 Background and research motivation	1
1.1.1 Background	1
1.1.2 Research motivation and scope	4
1.2 Challenges and contributions	5
1.2.1 Challenges	5
1.2.2 Contributions	6
1.3 List of published papers	7
1.3.1 Journal publications	7
1.3.2 Conference publications	7
1.4 Thesis organisation	8
2 Literature review	10
2.1 The future of power grid systems	10
2.1.1 Smart grid and microgrid concepts	10
2.1.1.1 Smart grid	10
2.1.1.2 Microgrid	12
2.1.2 Power interface devices	13
2.1.2.1 DC/DC converters	13
2.1.2.2 DC/AC converters	15
2.1.3 Control strategies and grid code requirements in smart power systems	16
2.1.3.1 Control strategies	16

2.1.3.2	Grid code requirements	18
2.2	The forthcoming inertia problem	20
2.2.1	Droop control	21
2.2.2	Virtual synchronous machines	23
2.2.3	Synchronverter	24
2.2.4	Virtual oscillator control	25
2.2.5	Virtual synchronous control	26
2.3	The protection of power interface devices	27
2.3.1	Existing current limitation strategies	28
2.3.1.1	Reference current saturation	28
2.3.1.2	Virtual impedance-based algorithm	29
2.3.1.3	d -axis priority-based saturation method	29
2.3.2	Circulating current prevention strategies	30
2.4	Stability and control issues in power converter-based DER systems . . .	30
2.5	Open challenges in the existing literature	33
3	Nonlinear control of three-phase grid-connected inverters	35
3.1	Nonlinear current-limiting controller for three-phase inverters	36
3.1.1	Background and motivations	36
3.1.2	Problem statement and system modeling	37
3.1.3	Controller design and analysis	38
3.1.3.1	Inner PI control loops	39
3.1.3.2	Proposed nonlinear controller (Outer loop)	39
3.1.4	Stability analysis and current-limiting proof	42
3.1.5	Simulation results	44
3.2	PLL-less three-phase inverters with current-limiting property	47
3.2.1	Background and motivations	47
3.2.2	Problem definition and system dynamics	49
3.2.3	Proposed nonlinear controller	51
3.2.4	Current-limiting property and closed-loop stability analysis . . .	52
3.2.4.1	Current-limiting property	52
3.2.4.2	Small-signal stability analysis	54
3.2.5	Simulation results	56
3.3	Three-phase inverters with inherent RMS current limitation	59
3.3.1	Background and motivations	59

3.3.2	Dynamic system modeling and problem statement	61
3.3.3	Proposed nonlinear controller and RMS current-limiting property	63
3.3.3.1	Proposed nonlinear controller	63
3.3.3.2	RMS current-limiting property	65
3.3.4	Closed-loop stability analysis	67
3.3.5	Performance comparison with the existing methods	74
3.3.6	Experiment results	76
3.3.6.1	Normal grid operation	77
3.3.6.2	Operation under balanced grid voltage sags	79
3.4	Conclusions	82
4	Virtual synchronous control of three-phase inverters considering DC-link voltage dynamics	84
4.1	Three-phase inverters with virtual inertia and current limitation capabilities	85
4.1.1	Background and motivations	85
4.1.2	Dynamic system modeling and necessary definitions	86
4.1.3	Proposed nonlinear controller, RMS current limitation, and ViSynC integration	88
4.1.3.1	Proposed nonlinear controller and current limitation	88
4.1.3.2	ViSynC integration	89
4.1.4	Small-signal stability analysis	90
4.1.5	Simulation results	92
4.2	Current-limiting virtual synchronous control and stability analysis considering DC-link dynamics	95
4.2.1	Background and motivations	95
4.2.2	Closed-loop stability analysis	97
4.2.2.1	Closed-loop system	98
4.2.2.2	Boundary layer analysis	99
4.2.2.3	Reduced system analysis	100
4.2.3	Comparison with the existing methods	102
4.2.4	Experimental studies	107
4.2.4.1	Hardware-in-the-loop (HIL) results	107
4.2.4.2	Comparison studies via HIL results	112
4.3	Conclusions	115

5	Avoiding circulating current in AC microgrids	116
5.1	Background and motivations	116
5.2	Microgrid modeling	118
5.3	The proposed current-limiting and DC-link controllers	120
5.4	Closed-loop small-signal stability analysis	121
5.5	Simulation results	123
5.6	Conclusions	128
6	Conclusions and future work	129
6.1	Conclusions	129
6.2	Future work	131
	Bibliography	133

List of Figures

1.1	Main components of smart grid systems.	2
1.2	A typical example of a microgrid.	3
2.1	A microgrid with several DERs.	12
2.2	Unidirectional DC/DC converters.	14
2.3	Bidirectional DC/DC converters.	14
2.4	DC/AC inverters.	15
2.5	Hierarchical control layers in future power systems.	17
2.6	FRT curves required by German and Danish grid codes [77].	18
2.7	RE sourced SG and VSG based power plants.	19
2.8	Basic virtual inertia concept.	20
2.9	Droop control dynamics considering different types of inverter output impedance.	22
2.10	VSM inertia model, and voltage controller using reactive power droop.	24
2.11	Controller stage of synchronverter.	25
2.12	Van der Pol oscillator based VOC with active and reactive power regulation capability.	26
2.13	Reference current saturation concept.	28
2.14	Virtual impedance based current limitation concept.	29
2.15	Classification of stability concepts in microgrids.	31
2.16	Commonly used cascaded inverter control scheme.	32
3.1	Grid-connected three-phase inverter with an LCL filter.	37
3.2	System active and reactive powers.	45
3.3	d - and q -axis grid currents.	45
3.4	d -axis capacitor voltage.	46
3.5	q -axis capacitor voltage.	46
3.6	The trajectories of the controller states E_d , E_{dq} , E_q , and E_{qq}	46

3.7	Three-phase grid-connected inverter with an L filter.	48
3.8	Axis transformation.	49
3.9	Implementation diagram of the proposed controller.	52
3.10	Closed-loop system eigenvalues as a function of controller gain c_d with $0.1 \leq c_d \leq 50$	55
3.11	RMS voltage.	57
3.12	Active and reactive power.	57
3.13	d - and q -axis currents.	57
3.14	Response of the controller states.	58
3.15	Grid-connected three-phase inverter.	61
3.16	Implementation diagram of the proposed controller.	64
3.17	Regions for selecting P_{set} and Q_{set} to ensure closed-loop stability. . . .	71
3.18	Performance comparison between the Benchmark Ctrl 1 (a)-(b) and the Proposed controller (c)-(d) under a three-phase short-circuit fault. . . .	74
3.19	Performance comparison between the Benchmark Ctrl 2 (a)-(b) and the Proposed controller (c)-(d) under a 30% balanced grid voltage sag. . . .	75
3.20	Experimental setup.	76
3.21	Grid-supporting inverter operation under the proposed controller during normal grid conditions.	78
3.22	Grid-supporting inverter response under the proposed controller when a balanced voltage sag $110 V \rightarrow 70 V$ occurs.	80
3.23	Grid-supporting inverter response under the proposed controller when a balanced voltage sag $110 V \rightarrow 55 V$ occurs.	81
4.1	DER-sourced grid-connected VSC system	86
4.2	Vector diagram of local (dq) and global (DQ) PCC frames.	87
4.3	Implementation diagram of the proposed controller integrated with the ViSynC.	90
4.4	Closed-loop eigenvalue spectrum as a function of K_D (a), K_J (b), K_T (c), and c (d).	92
4.5	Active and reactive power.	93
4.6	Inverter i_d and i_q currents.	93
4.7	DC-link voltage.	94
4.8	RMS voltage.	94
4.9	Regions for selecting P_s and Q_{set} to ensure closed-loop stability.	102

4.10	Performance comparison of the original [116] and the proposed controller. (a), (b), (c), and (d) with $K_J = 10 \text{ kgm}^2$, (e), (f), (g), and (h) with $K_J = 50 \text{ kgm}^2$, while $K_T = 4 \text{ Nm/V}^2$ and $K_D = 2500 \text{ Nms}$	104
4.11	Performance comparison of the original [116], with (orig.) and without (naw) anti-windup techniques, and the proposed controller in case of a short-circuit (a), (b), (c), and (d) with $K_J = 10 \text{ kgm}^2$, (e), (f), (g), and (h) with $K_J = 50 \text{ kgm}^2$, while $K_T = 4 \text{ Nm/V}^2$ and $K_D = 2500 \text{ Nms}$. . .	105
4.12	Frequency comparison of the original [116], with (orig.) and without (naw) anti-windup techniques, and the proposed controller in case of entire scenario (a) with $K_J = 10 \text{ kgm}^2$ (b) with $K_J = 50 \text{ kgm}^2$, and in case of a 40% balanced grid fault (c) with $K_J = 10 \text{ kgm}^2$ (d) with $K_J = 50 \text{ kgm}^2$, while $K_T = 4 \text{ Nm/V}^2$ and $K_D = 2500 \text{ Nms}$	106
4.13	HIL experimental setup.	107
4.14	HIL results of a DER-sourced inverter under the proposed controller with different K_D gains.	109
4.15	HIL results of a DER-sourced inverter under the proposed controller with different K_J and K_T gains.	110
4.16	HIL results of a DER-sourced inverter under the proposed controller in case of a balanced voltage sag (a) $110 \text{ V} \rightarrow 70 \text{ V}$ and recovery (b) $70 \text{ V} \rightarrow 110 \text{ V}$	111
4.17	HIL results of a DER-sourced inverter under the proposed controller when the grid frequency (ω_g) changes.	112
4.18	HIL results of a DER-sourced inverter under the proposed controller when the stability condition (4.32) is tested.	113
4.19	HIL comparison results of a DER-sourced inverter under proposed and conventional current-limiting methods ([26] and [123]) when $K_D = 30000 \text{ Nms}$, $K_J = 10 \text{ kgm}^2$, and $K_T = 10 \text{ Nm/V}^2$	114
5.1	The microgrid system under consideration.	118
5.2	Closed-loop eigenvalue spectrum of inverter 1 as a function of active power droop coefficient $n_1 : \frac{0.01\sqrt{2}E^*}{S_{max}} \leq n_1 \leq \frac{0.3\sqrt{2}E^*}{S_{max}}$	122
5.3	Active power outputs of three parallel-connected three-phase inverters .	124
5.4	Reactive power outputs of three parallel-connected three-phase inverters	124
5.5	RMS currents of three parallel-connected three-phase inverters	125
5.6	dq frame currents of three parallel-connected three-phase inverters . . .	125
5.7	Frequencies of three parallel-connected three-phase inverters	126

5.8	DC voltages of three parallel-connected three-phase inverters	126
5.9	The maximum value of the PCC voltages of three parallel-connected three-phase inverters	127

List of Tables

- 2.1 Comparison of existing and future power grid systems 11
- 3.1 System and controller parameters for the examined inverter system . . 44
- 3.2 System and controller parameters for the simulation studies 56
- 3.3 System hardware and control parameters for experimental studies . . . 70
- 3.4 Three-phase inverter system and controller parameters for comparison
studies 73
- 4.1 DER-based simulated inverter system and controller parameters 91
- 4.2 DER-based inverter system and controller parameters for comparison
and HIL studies 103
- 5.1 Simulated AC-MG system and controller parameters 122

Chapter 1

Introduction

1.1 Background and research motivation

1.1.1 Background

Starting from the beginning of 20th century, power generation is accepted as one of the most significant accomplishments that is achieved by humankind and affects societies from political, economic, and technological perspectives [1]. Due to the increasing speed of electricity-dependent technological advancements in recent decades, power production and management have become the most critical priorities in global communities. However, since the initial power generation tools utilize mainly fossil fuels, such as coal, gas, and petroleum, the CO₂ release into the atmosphere has reached detrimental levels and started threatening human life by causing natural disasters. Therefore, the green energy concept has gained universal popularity around the world in the last decades, and it is claimed that the decarbonization efforts can lead to ‘The Third Industrial Revolution’ [2].

Renewable energy sources (RESs), e.g., wind and solar photovoltaics, based distributed energy resources (DERs) are considered as best solutions to meet the ever-increasing power demand due to their green and sustainable characteristics. Therefore, both United Nations and European Union encourage and take measures to increase the percentage of DERs in total power production to achieve a considerable decrease of greenhouse gases by 2050 [3]. Nevertheless, as the traditional power generation systems, which have been used for over 100 years, are based on bulky synchronous generators (SGs), have obsolete infrastructures, and serve only as unidirectional sources, the integration of distributed energy resources (DERs) into the existing power system constitutes a significant challenge in terms of system reliability, and stability [4, 5, 6].

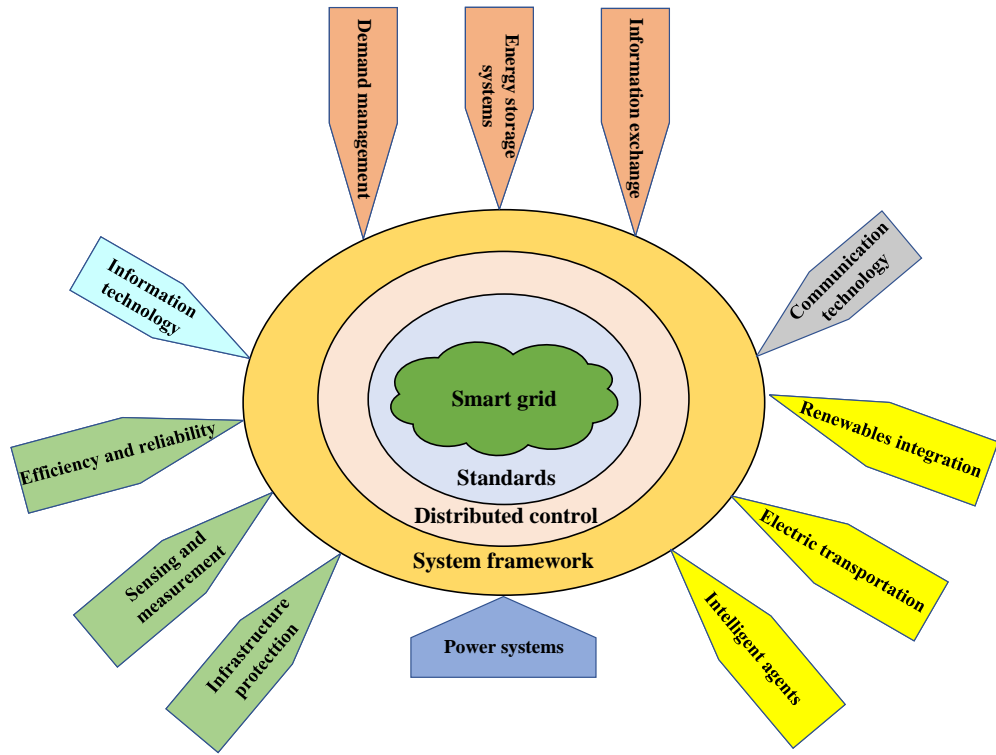


Figure 1.1: Main components of smart grid systems.

In order to deal with the issues mentioned above, the smart grid concept has emerged as a promising solution [1].

A smart grid is an intelligent interconnected electric system, which can integrate DERs into the existing power grid with high efficiency, allow bidirectional data transfer between customers and utility companies, dispatch energy storage systems in case of system faults with the help of information and communications technologies (ICTs) [6, 7, 8] as illustrated in Figure 1.1 [6]. Although the smart grid is the generic concept for the future power grid system, the main units to achieve a seamless, reliable, and economic transition from traditional to the smart grid are microgrids (MGs). After being introduced in [9], MGs have gained a great deal of attention in power electronics and control system communities since they can work both in grid-connected and stand-alone modes, appear in low and medium voltage applications, and contain DERs, energy storage systems (ESSs), and local loads [10, 11]. Therefore, it is important to examine the dynamics of MGs and their subsystems, and design proper control algorithms for them.

Since MGs are complex engineering systems that can include many DERs with power interface converters, AC and DC loads, as shown in Figure 1.2 [12], advanced

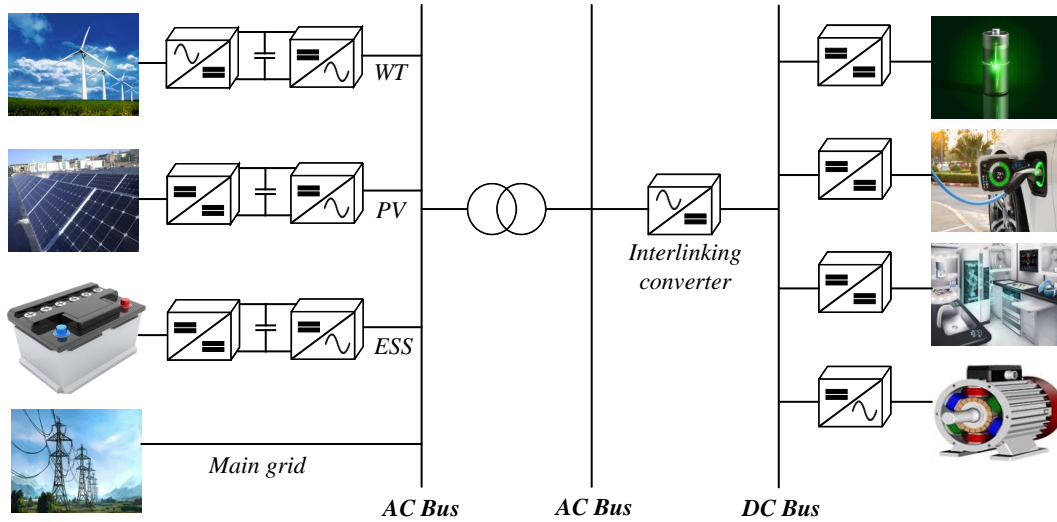


Figure 1.2: A typical example of a microgrid.

control systems should be designed to guarantee a reliable MG operation. As opposed to the traditional grid systems, which employ centralized controllers, the control algorithms of MGs are generally decentralized in the primary level, and they adopt a hierarchical structure [13]. This hierarchical architecture includes primary, secondary, and tertiary control layers, and every level has particular objectives to achieve in different time intervals [14, 15]. At the primary level, MG voltage and frequency are controlled via well-known droop and emerging virtual synchronous controllers without using communication infrastructures, while in secondary control, the voltage and frequency deviations caused by the converter output impedance differences are restored. In tertiary control, optimal power flow between the MG companies and grid utilities is aimed at considering economic benefits [16, 17, 18].

In modern power systems, primary control is responsible for the working principle imitation of conventional synchronous generators (SGs), and this is generally achieved using droop controllers [13]. However, traditional droop controllers, especially in grid-connected mode, may not guarantee the frequency stability in case of variable DC-link voltages and system disturbances [19, 20]. Therefore, virtual inertia based algorithms, such as synchronverter, virtual synchronous machine (VISMA), and synchronous power controller (SPC), are proposed for stability improvement, and smooth MG operations [21, 22].

The key elements of MGs are DC/DC, DC/AC, and AC/DC power converters as shown in Figure 1.2, since they work as interface devices between DER units and utility grid/loads [23, 24]. Power converters can be designed as grid-following, grid-

supporting, and grid-forming structures, and each structure is used to carry out specific tasks, such as active and reactive power control, synchronization, fault-ride through, current, voltage and frequency regulation [8, 25]. In order to achieve these tasks and guarantee a reliable MG application, the stability of MGs is mainly investigated in the primary layer, which requires the fastest control actions, through individual power converter dynamics [11, 26]. However, the stability is generally examined via eigenvalue analysis techniques without providing analytic stability conditions that can guide potential users in their designs [26, 27]. Besides, since power converters contain electronic switching components, such as IGBTs and MOSFETs, which have low fault voltage and current thresholds, proper protection algorithms should be designed without additional system costs [28, 29]. These algorithms should ensure that there will be no unnecessary protection trip due to over-current and over-voltage even in the cases of bidirectional operation, circulating current flow, and short-circuits in both grid-connected and islanded modes.

1.1.2 Research motivation and scope

Future power grids will include hundreds of thousands of power converter based DERs, and even single converter failure can cause local MG failures and power cuts. Therefore, special efforts are needed to model and analyse the power interface devices. The key topics that will lead us to the smart grid concept are summarised and the importance of advanced controller design for power converters to ensure stable and reliable MG operation is emphasized in the previous subsection.

In the present literature, linear controllers are generally used for nonlinear power converter systems and the closed-loop stability analysis of the system is generally examined considering a specific operating point, which is valid only for the given system parameters. The system stability may not be guaranteed if this operating point changes due to the different power reference values chosen by the operators or unexpected system disturbances. Therefore, nonlinear controllers should be designed to guarantee the system stability under large system faults. Besides, the existing stability analysis techniques may not result in analytic stability conditions that can guide the designers for choosing controller and system parameters. In addition, over-current protection is another critical aspect for power converter-based DERs, since power converters include semiconductor switches that can be damaged if exposed to high currents in case of faults, such as grid voltage sags and short-circuits. This issue is usually handled by using saturation blocks to limit the reference values, employing virtual impedances in

controller design process, and modifying the control algorithm structure when a fault occurs. However, these methods may require system parameter information and lead to the well-known integrator windup problem, system instability and current limit violation under severe faults.

In this thesis, advanced nonlinear controllers are proposed to ensure closed-loop system stability, inherent current-limiting and anti-windup properties in power converter-based DER applications. The proposed controllers are applied to single and parallel-connected three-phase inverters in both grid-connected and islanded modes. Opposed to the existing approaches that ignore detailed stability analysis, theoretical stability proofs are provided, and analytic conditions for stability are obtained to guide the potential users in their designs.

1.2 Challenges and contributions

1.2.1 Challenges

An efficient and reliable MG application can be achieved when easily implementable controllers are designed for the power interface converters. While designing these controllers, it should be considered that the mathematical models of power converters include nonlinear expressions, so their closed-loop system becomes nonlinear. In the existing literature, since linear controllers are generally employed for the nonlinear power converter systems, the closed-loop stability cannot be guaranteed when a large system fault, such as voltage sag and short-circuit, occurs. Thus, advanced nonlinear controllers are required to ensure fail-safe DER operations.

Below, a list of major challenges related to power converter control in future smart grids is provided.

- Linear controllers are designed for nonlinear power inverter systems, and therefore the system stability and grid synchronization may not be ensured during the entire operation, e.g., grid connection and disconnection, mode transitions, and large voltage sags.
- State-of-the-art controllers are examined via root locus and bode analysis, which are valid only for the given system parameters, without providing analytic stability conditions. Besides, these methods do not provide rigorous closed-loop system stability analysis.
- The existing power converter modeling techniques complicate the closed-loop

stability analysis by increasing the number of system states. New control techniques are required to decrease the number of system states and lead to easier implementation.

- Current limitation issue, which is critical for power converter protection, is generally realised using additional saturation units with PI controllers by ignoring the negative effect of integrator windup. However, unresolved integrator windup issue can cause system instability due to high integrator energy in case of faults.
- A composite virtual synchronous control method, which can inherently achieve both virtual inertia and current limitation features in power converter applications even under severe system faults and provide a rigorous closed-loop stability analysis with parameter selection guidance, is missing in the literature.
- In parallel-connected inverter applications, there are some controllers to prevent circulating current flow in the literature. However, a combined method that can avoid the current limit violation and circulating current, and ensure closed-loop system stability for individual inverters is needed for reliable microgrid operations.

1.2.2 Contributions

The main contributions of this thesis are outlined as below;

- Considering the nonlinear power converter dynamics, advanced nonlinear controllers that can guarantee current-limiting property, closed-loop stability, and grid synchronization under both normal and abnormal system conditions are proposed. Besides, the integrator windup issue is inherently solved via unique structure of the proposed controllers.
- The proposed controllers are designed in a distinctive way to decrease the complexity of power converter modeling. Therefore, the implementation can be easily achieved.
- Rigorous closed-loop stability analysis for the power converter systems is realised, and analytic stability conditions are provided without assuming specific set of system parameters.
- A unified method that combines droop dynamics and virtual synchronous control and ensures current-limiting property under severe grid voltage sags is proposed,

and detailed closed-loop stability analysis and analytic stability conditions are provided to guide the prospective designers.

- Circulating current issue in AC MGs with parallel-connected inverters is examined, and a controller is designed to avoid circulating current between inverters, protect individual inverters against over-currents, and ensure the closed-loop system stability.
- Comparison studies are realised to verify that the performances of proposed controllers are better than the existing methods.

1.3 List of published papers

1.3.1 Journal publications

1. S. Dedeoglu, G. C. Konstantopoulos and H. Komurcugil, “Current-limiting Virtual Synchronous Control and Stability Analysis Considering DC-link Dynamics Under Normal and Faulty Grid Conditions,” *IEEE Journal of Emerging and Selected Topics in Power Electronics*, doi: 10.1109/JESTPE.2021.3103830.
2. S. Dedeoglu, G. C. Konstantopoulos and A. G. Paspatis, “Grid-Supporting Three-Phase Inverters with Inherent Root Mean Square Current Limitation Under Balanced Grid Voltage Sags,” *IEEE Transactions on Industrial Electronics*, vol. 68, no. 11, pp. 11379-11389, Nov. 2021, doi: 10.1109/TIE.2020.3034860.
3. A. G. Paspatis, G. C. Konstantopoulos, and S. Dedeoglu, “Control Design and Small-Signal Stability Analysis of Inverter-Based Microgrids with Inherent Current Limitation Under Extreme Load Conditions,” *Electric Power Systems Research*, vol. 193, no. June 2020, p. 106929, 2021, doi: 10.1016/j.epsr.2020.106929.

1.3.2 Conference publications

1. S. Dedeoglu, G. C. Konstantopoulos, “Avoiding Circulating Current via Current-Limiting Control in AC Microgrids with Parallel Three-Phase Inverters,” *IECON 2021 - 47th Annual Conference of the IEEE Industrial Electronics Society*, 2021, to be published.
2. S. Dedeoglu, G. C. Konstantopoulos and H. Komurcugil, “Current-Limiting VSG for Renewable Energy Applications,” *2021 IEEE 30th International Symposium*

- on Industrial Electronics (ISIE), 2021, pp. 01-05, doi: 10.1109/ISIE45552.2021.9576298.
3. S. Dedeoglu and G. C. Konstantopoulos, “PLL-Less Three-Phase Droop-Controlled Inverter with Inherent Current-Limiting Property,” IECON 2019 - 45th Annual Conference of the IEEE Industrial Electronics Society, 2019, pp. 4013-4018, doi: 10.1109/IECON.2019.8927219.
 4. S. Dedeoglu and G. C. Konstantopoulos, “Three-Phase Grid-Connected Inverters Equipped with Nonlinear Current-Limiting Control,” 2018 UKACC 12th International Conference on Control (CONTROL), 2018, pp. 38-43, doi: 10.1109/CONTROL.2018.8516764.

1.4 Thesis organisation

The remaining part of this thesis is organised as follows:

Chapter 2 presents a comprehensive literature review starting from smart grid and microgrid concepts. Then, the inertia issue in the future grid systems is examined considering well-known droop controllers and emerging virtual inertia algorithms. Next, the importance of power converter protection is highlighted, focusing especially on the state-of-the-art current limitation algorithms. In the final part, the stability issues in future power systems are discussed, and gaps in the existing literature are summarised.

Chapter 3 introduces advanced nonlinear controllers for three-phase grid-connected inverters and is divided into three sections. In the first section, a current-limiting controller considering inner voltage and current loops based on the bounded integral controller (BIC) is proposed. In the second section, a PLL-less control method is proposed by simplifying the system model via aligning the inverter current to the local d -axis. Finally, in the third section, a nonlinear current-limiting algorithm based on the state-limiting PI (sl-PI) controller is proposed for grid-supporting three-phase inverters, asymptotic stability analysis is proven, and detailed comparison and experimental results are provided.

Chapter 4 investigates the virtual inertia issue for the three-phase inverters and is divided into two sections. The first section explains the basics of the proposed hybrid method, which uses both droop and virtual synchronous controllers, and provides useful simulation results. In the second section, the proposed virtual inertia algorithm is detailed with asymptotic stability analysis. Comprehensive hardware-in-the-loop results are provided to verify the superior performance of the proposed method compared

to the existing methods.

In Chapter 5, the circulating current problem in AC microgrids is examined. A microgrid, which has three parallel-connected three-phase inverters, is modeled. Then, using the sl-PI controller and universal droop dynamics, a nonlinear algorithm to avoid circulating current and limit the system current is proposed. Simulation results validate the effectiveness of the proposed controller.

In Chapter 6, conclusions and future study directions are provided.

Chapter 2

Literature review

2.1 The future of power grid systems

Environmental concerns, power generation inefficiency, and grid reliability issues due to aging infrastructure are some of the important reasons for the paradigm change in the existing power grid systems [30, 31, 32]. In order to achieve this significant change, the future grid will be different from the existing grid in many ways, such as power generation approach, i.e., from centralized to distributed, equipment type, i.e., from electric machines to power electronics, communication method, i.e., from unidirectional to bidirectional as summarised in Table 2.1 [6, 33, 34, 35]. Besides, the existing power infrastructure is not capable of dealing with the modern grid problems, such as the continuous increase of demand, cyber-attacks, renewable energy-based DERs integration, interconnection requirements, since their initial design was completed considering obsolete specifications [35, 36, 37]. In this section, some critical topics and issues related to the future power systems, such as smart grid and microgrid concepts, the inertia problem, power interface protection, and system stability, are thoroughly reviewed.

2.1.1 Smart grid and microgrid concepts

2.1.1.1 Smart grid

Smart grid concept has initially emerged to increase energy efficiency, provide enhanced demand-side management capabilities via advanced metering infrastructures, and build reliable protection systems against natural disasters and cyber-attacks. However, as the technology improves and power demand increases, the initial concept has become more complicated, and it led to the creation of new standards and law regulations in various countries [34]. The main technological advancements required to achieve a

Table 2.1: Comparison of existing and future power grid systems

Existing grid systems	Future grid systems
Rotating machine based	Power electronics based
Unidirectional communication	Bidirectional communication
Limited active main sources	Large number of active sources
Low percentage of DERs integration	100% DERs based generation
Centralized control and generation	Distributed control and generation
Traditional metering infrastructure	Advanced metering infrastructure
Frequent blackouts and failures	Local blackouts and self-repairs
Aged sensing technology based	Advanced sensing technology based
Limited client choices	Many client choices
Long distance power generation	Short distance power generation

smart grid can be outlined as in the following [32],

1. New materials and alternative clean energy sources: As the efficiency of devices used in the applications increases, power system efficiency improves, and energy losses decrease [38]. Besides, high penetration of RESs, such as solar, wind, wave and tidal, biomass, small-scale hydro-electric plants [39], alleviates the harmful environmental impacts caused by the fossil-fuel-based power generation.
2. Advanced power electronics and devices: The power semiconductor components, such as IGBTs and MOSFETs, can significantly improve the power quality, system efficiency and decrease the circuit size and cost [40].
3. Sensing and measurement: Intelligent monitoring devices form the basis for communication and control systems, and they are the key devices to transform from the traditional grid to the smart grid [7, 41].
4. Communications: Accurate information transfer between DERs and MGs is critical for a reliable, stable and seamless operation. Loss of communication can lead to system instability, and efficiency decrease [4, 42, 43].
5. Advanced computing and control methodologies: The improvements in microchip technologies will encourage manufacturers to build more realistic real-time simulation and hardware experiment devices. Thus, novel controllers and methods can be easily implemented.
6. Mature power market regulation and policies: Encouraging market policies will

increase the competition and participation in the power industry. Thus, the power cost will be minimized for the users [44, 45].

7. Intelligent technologies: Smart grid components can gain self-learning and healing abilities with these technologies, and thus the possibility of power failure in case of system abnormalities can be decreased [35, 46].

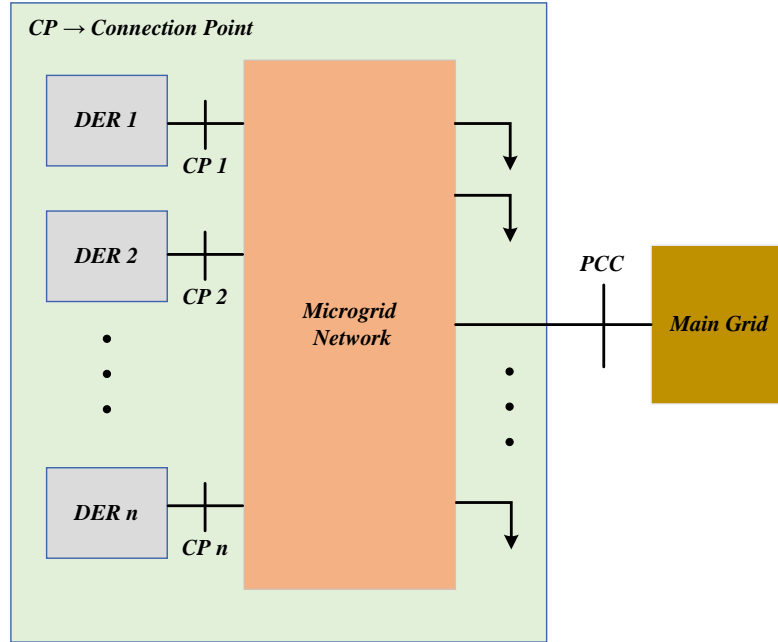


Figure 2.1: A microgrid with several DERs.

2.1.1.2 Microgrid

MGs are accepted as one of the key elements of smart grid, and many research efforts have been devoted to increase AC, DC, and hybrid MGs in grid-connected applications, since they improve grid flexibility and performance [29, 47]. There are two widely accepted MG definitions in the research community. The first one is ‘a cluster of loads, distributed generation (DG) units and ESSs operated in coordination to reliably supply electricity, connected to the host power system at the distribution level at a single point of connection, the point of common coupling (PCC)’ [10], and the second one is ‘an interconnection of DERs, such as microturbines, wind turbines, fuel cells and PVs integrated with storage devices, such as batteries, flywheels and power capacitors on low voltage distribution systems’ [48]. While MGs can be designed to feed the utility grid, they can also be used to provide power to specific fields, such as universities, military

bases, residential, remote and rural areas in islanded cases [49, 50]. An example MG, which includes several DERs is illustrated in Figure 2.1 [10].

In the design process of an MG, many research directions should be considered to feed the critical loads, achieve smooth grid connections, realise reliable and stable applications. Those directions can be summarised as; transmission, PCC, distribution, protections, monitoring, power converters, control, regulatory issues, and economic analysis [51]. In this thesis, the main focuses will be power converters, their control systems and protection algorithms.

2.1.2 Power interface devices

Power electronic converters are critical devices for high penetration of RES-based DERs into the power grids since they are used as interface components between DERs, ESSs, and loads [8] as shown in Figure 1.2. Power converters can be classified as DC/DC converters, AC/DC rectifiers, DC/AC inverters, and AC/AC converters, and they are used to realise different functionalities in different MG applications [52]. For instance, voltage step-up, step-down operations, and a constant DC voltage generation, even in the case of intermittent sources, can be achieved using DC/DC converters [53, 54], while active and reactive power production, synchronization, voltage and frequency control can be accomplished using DC/AC inverters [55, 56, 57]. In the following part, DC/DC converters and DC/AC inverters are explained in detail.

2.1.2.1 DC/DC converters

In some DER applications, the DC voltage that goes to the DC side of the inverters may need to be increased or decreased to the desired values. This process can be achieved using DC/DC converters by controlling the duty ratio signals that drive their power switches. If the ratio between the output and input voltages (V_{out}/V_{in}) is between 0 and 1, this converter is called as buck converter, and it is used to decrease the input voltage. In the case that V_{out}/V_{in} is greater than 1, the converter is called as boost converter, and it is used to increase the input voltage [52, 58]. Besides, they can be designed to deliver both unidirectional and bidirectional DC powers in RES-based DER applications [53].

Due to extensive employment of DC power sources, such as ESSs, PVs, fuel cells, DC/DC converters have become critical components to achieve a reliable, stable, and efficient MG operation, which can include electric vehicles, data centers, and household electronics [59, 60]. These converters can be designed using simple power electronics

components, such as inductors, capacitors, diodes, and power switches. In Figure 2.2 and Figure 2.3, unidirectional and bidirectional DC/DC converter schematics are provided, respectively [53].

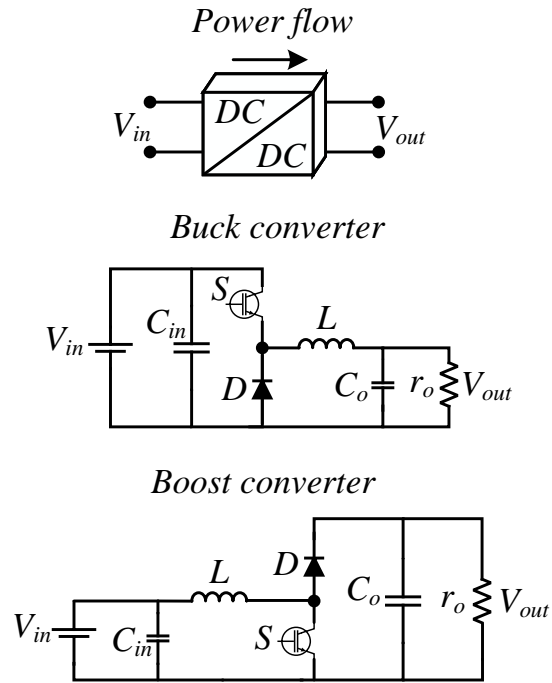


Figure 2.2: Unidirectional DC/DC converters.

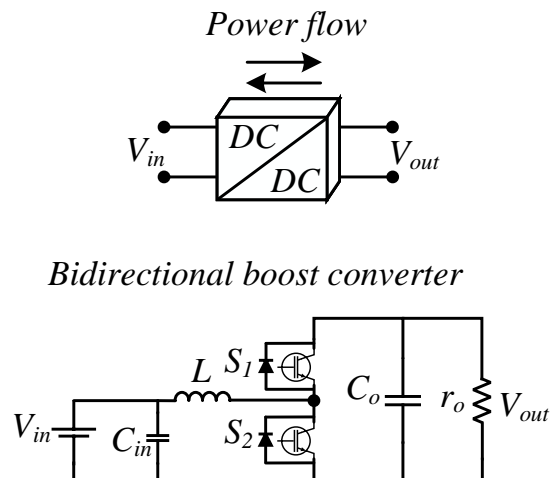


Figure 2.3: Bidirectional DC/DC converters.

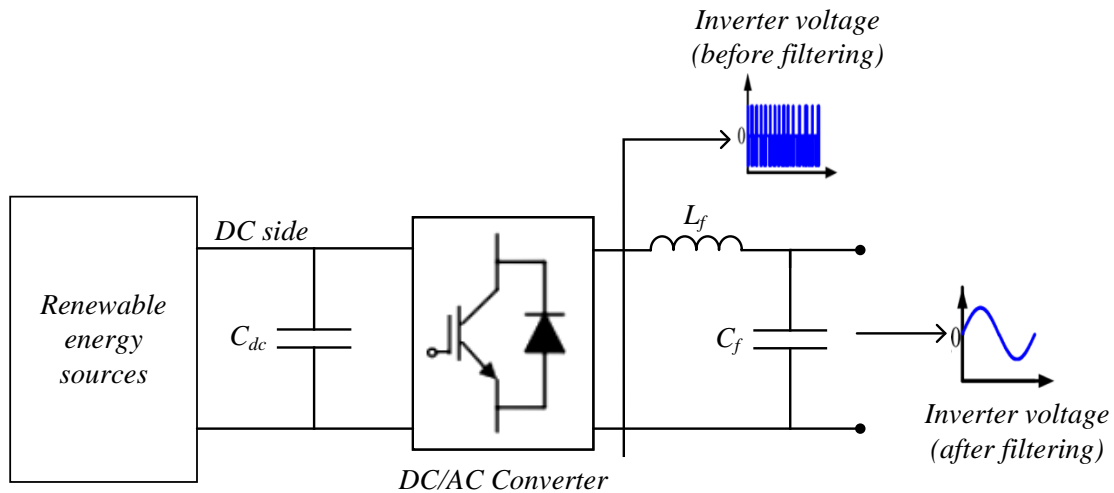


Figure 2.4: DC/AC inverters.

2.1.2.2 DC/AC converters

The main function of these converters is to generate AC voltage from a DC source, and they are generally called as inverters in the literature. Since RESs mostly produce DC power and the grid accepts only AC power form, inverters play a significant role in the integration of RESs-based MGs into the grid. The key functions that are achieved using inverters can be summarised as [61, 62, 63],

- Active and reactive power control.
- DC-link voltage control.
- Synchronization with the grid.
- High-quality current and voltage generation.
- Virtual inertia control.
- System stability support in case of faults.
- Contribution to the MG protection schemes.

Inverters can be designed considering both single-phase [64] and three-phase [55] configurations. A standard inverter schematic is given in Figure 2.4 [65]. The DC side of the inverters can include unidirectional or bidirectional DC/DC converters and input filters in different RES applications, and L , LC , or LCL filters are used at their outputs to generate purely sinusoidal output voltage [65, 66].

In order to accomplish the key functions mentioned above, inverter operations have been organised under three main modes, grid-following (or feeding), grid-supporting, and grid-forming [8, 46]. In grid-following mode, the reference power or current is injected into the PCC irrespective of the grid voltage and frequency deviations. This mode requires a phase-locked-loop (PLL) to obtain the grid frequency [67, 68]. In grid-supporting mode, the main objective is to regulate the grid voltage and its frequency via controlling the active and reactive power delivered to the PCC. In this mode, the inverter can be designed as either voltage or current sources [8, 67]. Finally, in grid-forming mode, the inverter works as a controllable voltage source similar to the SGs and dictates the microgrid voltage without the need of a PLL [67, 68]. In this thesis, the main focus is the control of three-phase inverters in both grid-connected and islanded cases.

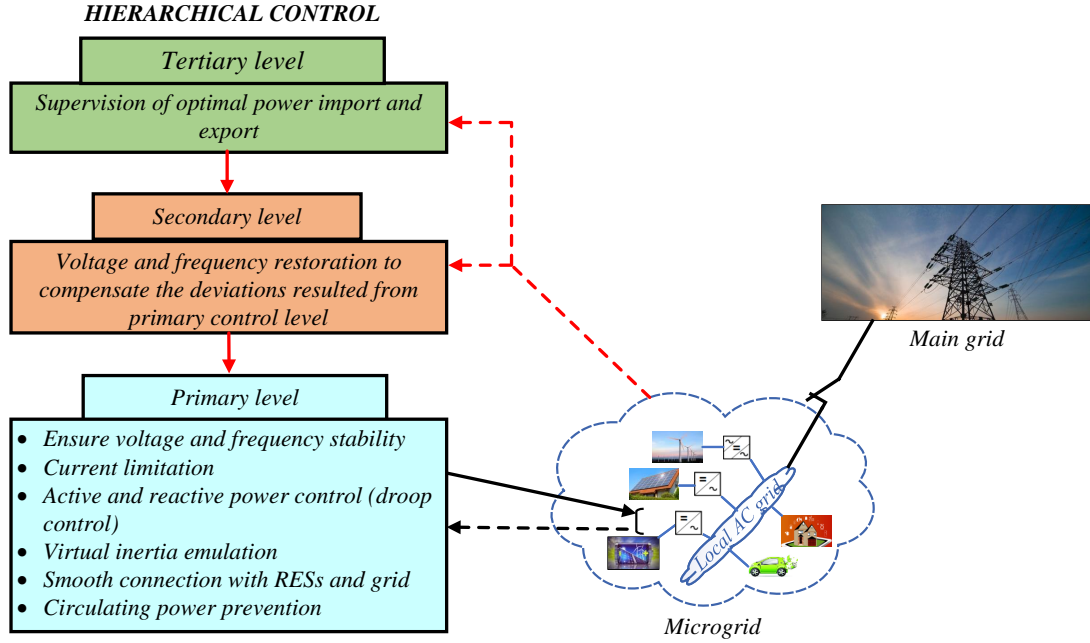
2.1.3 Control strategies and grid code requirements in smart power systems

2.1.3.1 Control strategies

Future power systems will be composed of a large number of grid-connected and islanded MGs, and this will highly increase the control complexity of the entire power network. Therefore, MG systems require the design of advanced control algorithms to achieve multiple functions for reliable and fail-safe DER operations [67, 69]. The main tasks that should be managed by the control systems can be summarised as below [17, 70, 71, 72]:

- Voltage and frequency regulation in both islanded and grid-connected modes;
- Seamless transition capability between islanded and grid-connected modes;
- Power exchange between MGs and utility grid;
- Accurate load sharing ability between DERs;
- MG synchronization with the utility grid;
- Optimization of the MG operation costs considering power demand/supply and energy forecast.

In future power systems, these tasks can be dealt with by using a hierarchical control structure in different time scales. Hierarchical control is divided into three



levels, which are primary, secondary, and tertiary controls and in each level, various control tasks are achieved [43]. Below, these levels are explained in detail.

1. **Primary control:** Converter level controllers, i.e., grid-feeding, grid-supporting, and grid-forming, are employed in this level to ensure voltage, current, and frequency stability under both normal and faulty conditions. In addition, the voltage and current references required for the DER operations are provided, active and reactive powers are regulated via well-known droop controllers, over-current and circulating current issues are investigated, frequency support is realised using virtual inertia algorithms, and DC-link voltage control is achieved at this level. Besides, since the primary level has the fastest time-scale in the hierarchical structure, the controllers used in this level should ensure a stable operation in case of faults until the higher control levels, i.e., secondary and tertiary, sense the abnormalities in the system. [17, 73, 74, 75].
2. **Secondary control:** The control actions employed in the primary control level can lead to the deviation of nominal voltage and frequency values of the MGs. In secondary control, the main goals are to remove these deviations and send proper commands to the DER units in MGs using monitoring and communication systems [8, 17].

3. **Tertiary control:** This level is both the highest and slowest control level in the hierarchical structure and focuses on the economic benefits in MG operations. Using advanced optimization, estimation algorithms and monitoring systems, the power generation, energy storage, power supply and demand capabilities of MGs are managed in a way to be profitable for the supplier companies [8].

In Figure 2.5, the hierarchical control structure is illustrated. As it is clear in Figure 2.5, while the primary level has a direct connection with the power converters without using communication systems, secondary and tertiary levels monitor abnormalities using communication infrastructures. In this thesis, the main focus is given to the primary control to investigate the dynamics of power converters (mainly three-phase inverters) and design advanced nonlinear controllers for them.

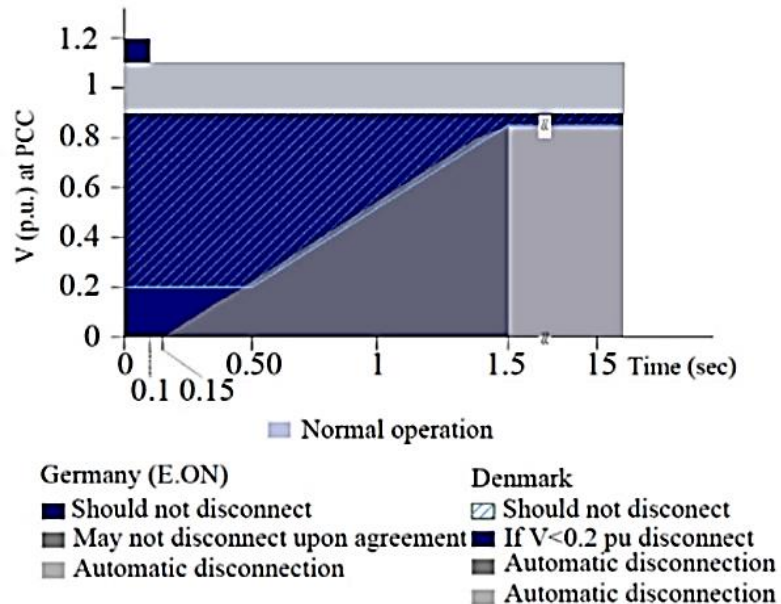


Figure 2.6: FRT curves required by German and Danish grid codes [77].

2.1.3.2 Grid code requirements

As the integration of RES based DERs to the grid increased in recent years, utility companies around the world have started to introduce grid codes to protect the power networks and ensure stable and reliable DER operations. The grid codes generally focus on the changes in frequency and voltage and can vary in different countries due to the specific power network characteristics and conditions. The grid code voltage requirements are called as either fault-ride-through (FRT) or low-voltage-right-through in the literature [76, 77]. In Figure 2.6, German and Danish FRT curves [77] are

illustrated as an example.

Grid codes dictate that power converter-based DERs should stay connected to the grid for a specified time even under severe voltage sags, as shown in Figure 2.6. Likewise, the power converters include semiconductor switches, which can fail instantly in case of fault transients; thus, proper protection schemes should be designed to avoid an undesired system failure [25]. After the fault is cleared, the power converter should be able to re-synchronize with the grid and recover to its normal operation as soon as possible [78, 79]. To this end, advanced controllers that can ensure current limitation, grid voltage and frequency support, re-synchronization with the grid, instant recovery to the normal operation points, and system stability even under severe grid voltage sags, should be designed for power converter-based DERs.

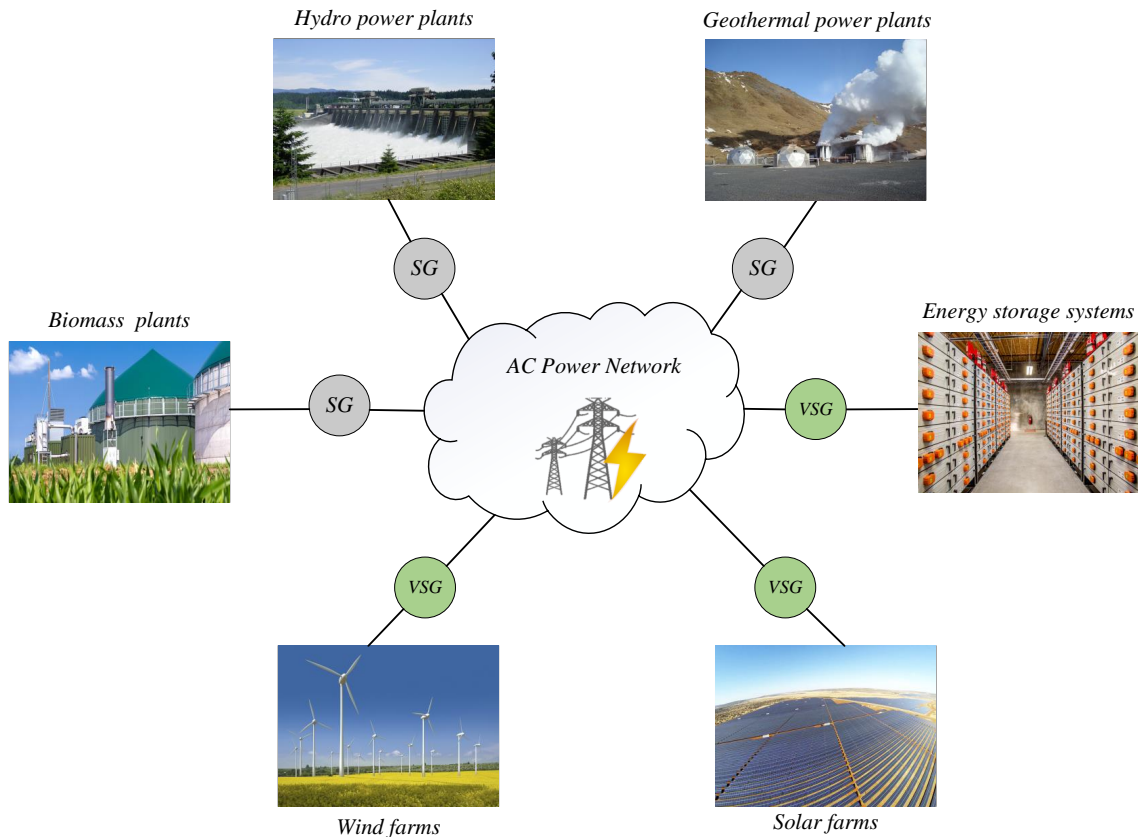


Figure 2.7: RE sourced SG and VSG based power plants.

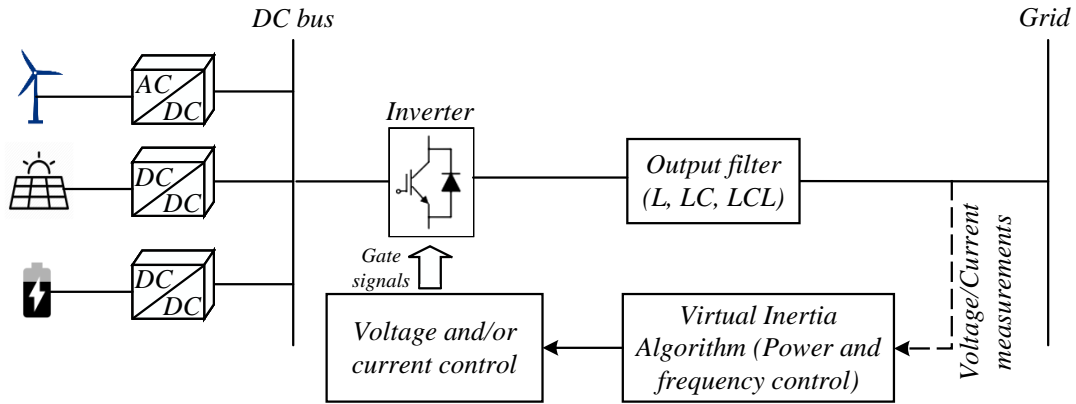


Figure 2.8: Basic virtual inertia concept.

2.2 The forthcoming inertia problem

In traditional power grid systems, the generation is based on large-scale SGs, which can provide rotational inertia to balance the power supply and demand and avoid frequency instability. However, power converters are static devices and cannot dispense physical inertia. Therefore, the large-scale integration of power converter-based DERs can lead to stability problems and system failures unless the converters are equipped with proper control algorithms [80, 81, 82]. It should be noted that even if some of the RESs, such as PVs and WTs, use power converters in their operations, there exist other RESs, such as hydropower, biomass, and geothermal, which rely on SGs [83] in the present AC power networks as shown in Figure 2.7 [84, 85]. In order to achieve 100% power electronic converter based generation without causing stability and inertia issues, advanced methods should be designed and employed in the DER applications [83]. It is agreed in the literature that the promising solution for solving these issues without increasing the system costs is to use virtual inertia concepts in the control design of power converter-fed DERs [20, 81, 86]. Virtual inertia can be implemented both using energy storage components, such as batteries and capacitors, and imitating SG dynamics via control algorithms [87]. The basic concept of virtual inertia algorithms is to produce the driver signals for the power inverter switches by using voltage and current measurements as feedback signals as visually presented in Figure 2.8 [82]. In this section, some of the well-known and emerging virtual inertia concepts, such as droop control, virtual synchronous machines, synchronverter, virtual oscillator control, and virtual synchronous control, are examined in detail.

2.2.1 Droop control

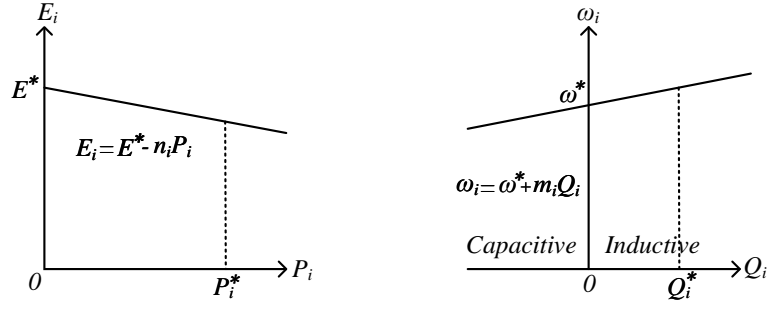
Droop control is the most commonly used power control method in converter-based DER applications since it does not require a dedicated communication infrastructure [55, 88]. Recently, it has been proven that droop control and virtual inertia control can be equivalent under certain conditions [19, 89]. Therefore, in this thesis, droop control is assumed to be a virtual inertia method. In DC/DC converters, active power/voltage (P/V) regulation [90], in DC/AC inverters active power/frequency (P/f) and reactive power/voltage (Q/V) regulations are generally achieved using traditional droop controllers. However, as the power converter-based generation and power network complexity increase, several other droop controllers are proposed, such as robust, adaptive, and universal droop controllers, to ensure seamless grid-connected and islanded mode transitions, accurate load sharing, and synchronization [88, 90].

Although the traditional droop control imitates the SG behaviour by coupling P/f and Q/V assuming inductive converter output impedance, the future power networks will include many different load characteristics that can affect the output impedance in both grid-connected and islanded modes. In Figure 2.9, droop control dynamics for inverters that have resistive, inductive, and capacitive output impedances are illustrated [94]. In order to solve the output impedance dependency issue, robust [92] and universal [93] droop controllers have been proposed.

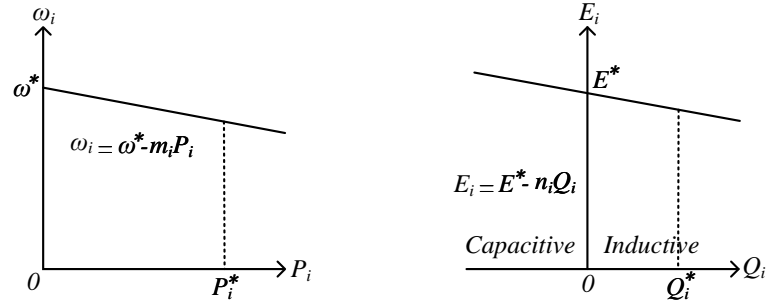
In grid-connected DER applications, a smooth connection can be achieved if the grid voltage and frequency are accurately measured or estimated. For this purpose, phase-locked loop (PLL) structures are mostly employed [61]. However, when there is a grid fault in the system, PLLs may not respond well due to their slow dynamics and lead to system instability [95]. Therefore, droop control can replace PLLs to ensure a stable and reliable DER operation [96]. Although droop control does not seem to include the swing equation of SGs, which includes damping and inertia dynamics, inertia property can be intrinsically added to droop control by using low-pass filters (LPFs) in active and reactive power measurements [89]. The active and reactive power droop coefficients can be arranged as inertia and damping coefficients; thus, droop control can support frequency dynamics and provide inertia [19, 97]. Below, this process is mathematically explained considering traditional droop dynamics and assuming inductive output impedance as given in [82].

$$\omega_g = \omega^* - m_p(P_{out} - P_{in}) \quad (2.1)$$

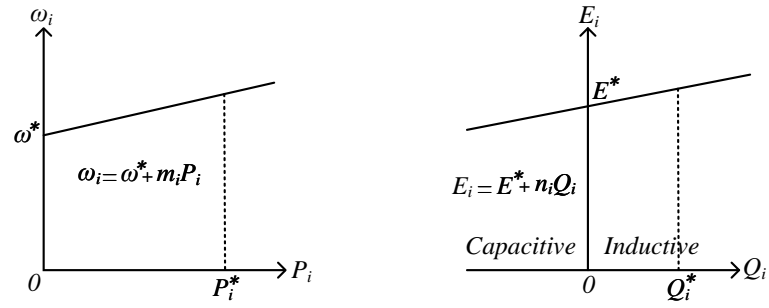
$$E_g = E^* - m_q(Q_{out} - Q_{in}) \quad (2.2)$$



(a) for resistive output inverters



(b) for inductive output inverters



(c) for capacitive output inverters

Figure 2.9: Droop control dynamics considering different types of inverter output impedance.

where, ω^* is the rated frequency, ω_g is the grid frequency, m_p is the active power droop coefficient, P_{in} is the active power reference, P_{out} is the measured output active power, E_g is the grid voltage, E^* is the reference voltage, m_q is the reactive power droop coefficient, Q_{out} is the measured output reactive power, Q_{in} is the reactive power reference. After adding a LPF, which has T_f as time constant, to (2.1), the relationship

between the input and output active powers can be arranged as [82, 89],

$$P_{in} - P_{out} = \frac{1}{m_p}(\omega^* - \omega_g) + \frac{T_f s \omega^*}{m_p}. \quad (2.3)$$

If the swing equation is considered as [89], the relationship between the active power droop coefficient (m_p) and damping (K_D) and inertia (K_J) gains can be found as [82],

$$K_J = T_f \frac{1}{m_p} \quad K_D = \frac{1}{m_p}. \quad (2.4)$$

Thus, the inertia provision capability of droop control is mathematically proven. It should be considered that the droop equations (2.1) and (2.2) may have slow dynamics, and the grid impedance may not have inductive characteristics. Therefore, enhanced droop methods [98, 99] based on the virtual impedance concept have been proposed to improve the system dynamics.

2.2.2 Virtual synchronous machines

Several virtual inertia methods are based on directly emulating the different orders of SG dynamics in the converter control algorithms, and the virtual synchronous machine (VSM or VISMA) concept is one of these methods [100]. In the employment of virtual inertia algorithms, the main objectives are to support the system frequency to avoid instability and eventually power outages and ensure a stable operation in both grid-connected and islanded modes without control method switch, and parameter changes [101]. VSM methods generally employ a PLL for initial grid synchronization, but then PLL is eliminated since the VSMS can ensure synchronization during normal operation via active power/frequency dynamics [102, 103]. VSM algorithm can ensure that the inverter current will follow the reference current generated via emulating the traditional SG dynamics; thus, the converter can supply virtual inertia and damping to the grid [104]. When VSM was introduced first time in [100], the control system of inverters was designed using the seventh order SG model [22]. However, due to its complexity, it was difficult to implement. Therefore, recently, simpler VSM algorithms have been proposed using lower-level SG models. In Figure 2.10, an easily implementable VSM method, which includes both inertia model and voltage controller, is provided. For the modeling and implementation details, the readers can refer to [101].

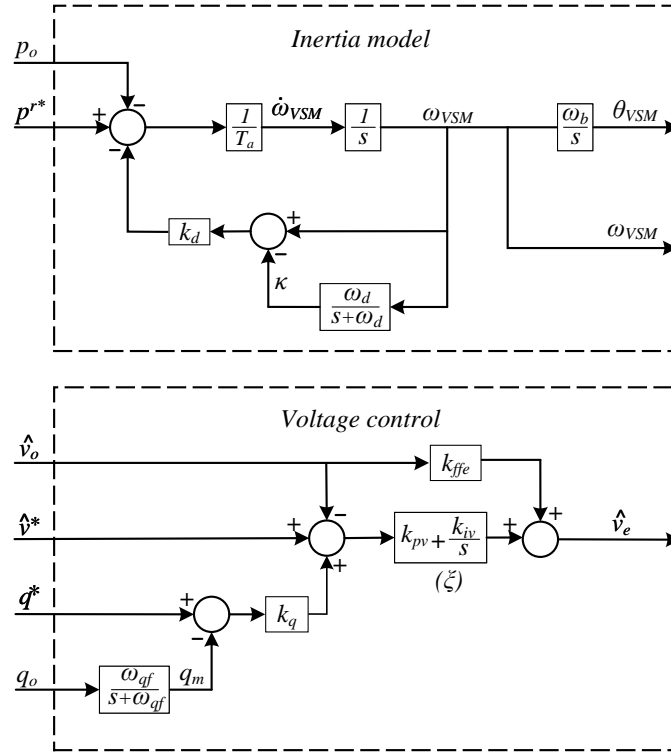


Figure 2.10: VSM inertia model, and voltage controller using reactive power droop.

2.2.3 Synchronverter

Synchronverter is another virtual inertia implementation method that mimics the traditional SG dynamics. The main idea of this method is to embed the dynamic equations of SGs into the inverter control system so that the inverter can produce an output voltage. The critical parameters of synchronverters, such as the virtual inertia, field inductance, and friction coefficient, can be easily configured to achieve a smooth grid connection. Besides, the synchronverter can support the power network stability by acting as a voltage source as opposed to VISMA, which behaves like a current source [62, 104]. Although the synchronverter concept implements the dynamics of SGs in power inverters, it replaces the mechanical power exchanged with the prime mover with the DC bus power [62, 87].

Since synchronverter employs the second-order SG model, the system complexity is much less than the initial VSM design, which uses the seventh-order SG model. Thus, its implementation is easier compared to VSMs [87]. In Figure 2.11, the control part of synchronverter is illustrated. For the modeling and implementation details, the readers can refer to [62].

When the dynamics equations of the synchronverter [62] are examined, it can be

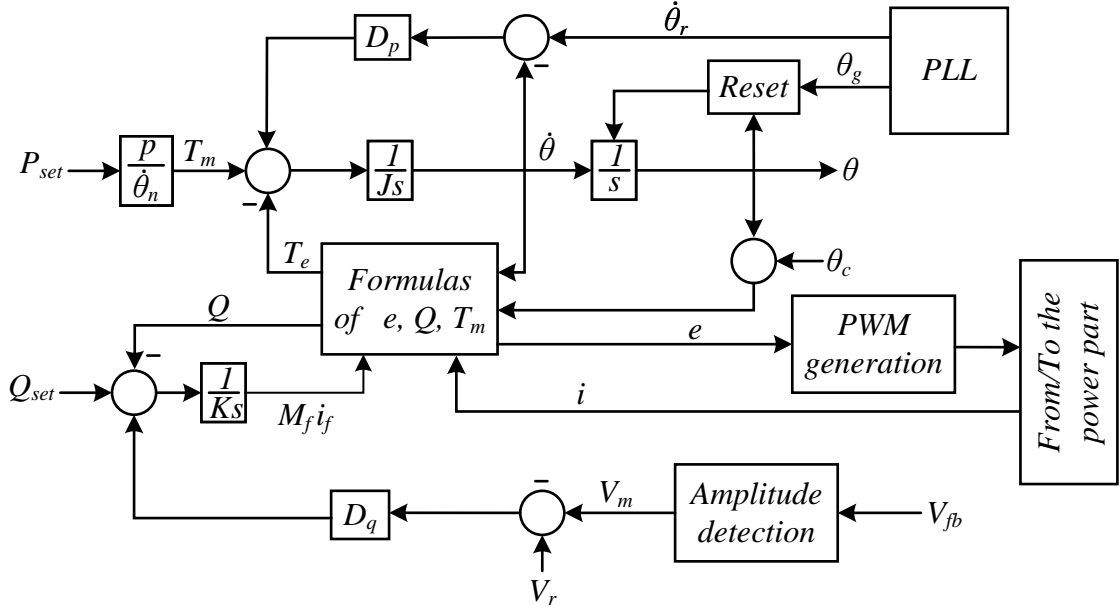


Figure 2.11: Controller stage of synchronverter.

assumed as an improved version of the PLL since it can inherently synchronize with the grid voltage. However, as the first proposed idea [62] needs an additional PLL structure to synchronize with the grid at the beginning of the operation, it may have stability problems when the grid has non-stiff frequency and voltage [105, 106]. Therefore, self-synchronized synchronverter [107] concept has been proposed to solve this issue and has further been studied in [108, 109]. Synchronverter can also be used as grid-forming inverter in islanded distributed generator and microgrid operations to provide inertia. On the other hand, since synchronverter mimics the synchronous generator dynamics, which are differential equations, it can be computationally intensive and may result in analytical deviations. Besides, as it does not include any built-in protection unit against grid fluctuations, safety precautions should also be taken into account [82].

2.2.4 Virtual oscillator control

The virtual oscillator control (VOC) method has a different working principle compared to the previously mentioned virtual inertia methods. It can ensure the grid synchronization and power-sharing using the well-known nonlinear oscillators, such as Van der Pol and Andronov-Hopf oscillators, instead of mimicking the SG dynamics without employing any communication units [25, 82, 110, 111]. In the VOC method, converter dynamics are arranged in a specific way that they can behave like a weakly

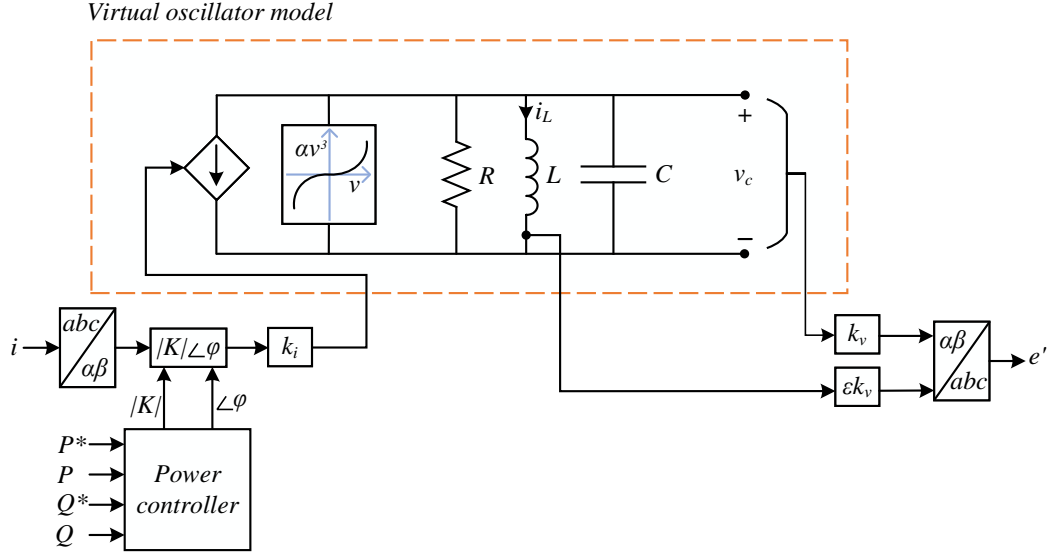


Figure 2.12: Van der Pol oscillator based VOC with active and reactive power regulation capability.

nonlinear limit-cycle oscillator to achieve synchronization with the other converters, and the grid using only the output currents as feedback signals [22, 26].

Due to its promising features, the VOC method has been implemented in both single-phase inverters [110], and three-phase inverters [112], and its performance has been compared with the droop control [113, 114]. According to [114], even if VOC shows a better performance compared to droop control in high-frequency ranges, droop control outperforms VOC in low-frequency ranges. It should be mentioned that the VOC schemes discussed in [113, 114, 115], have not considered the active and reactive power regulation, which makes them unsuitable for grid-connected operations. In order to solve this problem, a modified VOC scheme has been proposed in [112]. This scheme is illustrated in Figure 2.12 [25], and its technical details can be found in [112].

2.2.5 Virtual synchronous control

Virtual synchronous control (ViSynC) concept has been proposed in [116], is also called as matching control in [22, 117]. In this method, both the DC-link voltage control and grid synchronization are achieved via the DC-link voltage controller, and inertia is emulated via DC-link capacitor dynamics. The main control strategy is presented in

[116] as,

$$\omega^* = \omega_g + \frac{s + K_T}{K_{JS} + K_D} [V_{dc}^2 - V_{dcref}^2] \quad (2.5)$$

where ω^* is the converter angular frequency used for dq transformation, ω_g is the frequency setting value, V_{dc} is the DC-link voltage, V_{dcref} is the reference value of DC-link voltage, K_T is the DC-link voltage tracking gain, K_D is the damping gain, and K_J is the inertia emulation gain. The frequency setting value ω_g is designed as [116],

$$\omega_g = m \times \omega_{PLL} + (1 - m) \times \omega_0 \quad (2.6)$$

where m is the weighting gain, ω_0 is the nominal grid frequency, and ω_{PLL} is the grid frequency obtained using a PLL. It is important to note that this method can work without a PLL if K_T and K_D gains are chosen, properly. The value of m can cause the DC-link voltage deviation at the steady-state if the grid frequency changes. The new DC-link voltage value in case of grid frequency deviation can be calculated as [116],

$$V_{dc}^2 - V_{dcref}^2 = \frac{(1 - m)K_D}{K_T} (\omega^* - \omega_0). \quad (2.7)$$

Thus, a relationship between DC-link voltage and system frequency is established to provide inertia without using communication units. For more information, the readers can refer to [116].

To this end, although virtual inertia properties can be added using the previously explained methods, the converters, which are equipped with those algorithms, can be vulnerable against high currents in case of grid faults [25]. Therefore, proper protection methods should be designed to protect the converters from possible damages. In the next part, the commonly used current limitation techniques in the literature are discussed in detail.

2.3 The protection of power interface devices

A reliable MG operation can be ensured if the power converters, which are the main components of MGs, are protected against high voltage and current values during the entire system operation. Over-voltages and over-currents can occur in case of grid voltage sags, short-circuits, islanded to grid-connected or grid-connected to islanded mode transitions, and large load changes, and they can lead to converter hardware

damages and system instability [25, 118, 119, 120]. Besides, the circulating current between parallel inverters is another critical issue that can distort the voltage and current quality, increase the power losses, and decrease the system efficiency [121, 122]. Therefore, advanced control algorithms should be designed for the power converters to avoid the previously mentioned undesired phenomena. In the existing literature, the strategies employed for the current-limiting property can be summarised as reference current saturation, virtual impedance-based algorithm, and d -axis priority-based saturation [123, 124]. Also, the circulating current problem has been investigated via the DC-link voltage controllers [125, 126]. In this thesis, both the current limitation and circulating current issues for grid-connected three-phase inverters and MGs with parallel inverters are examined, and advanced nonlinear controllers, which can guarantee current-limiting property and system stability, and avoid circulating current between parallel-connected inverters even under faulty cases, are proposed. In the following part, the existing current limitation and circulating current prevention strategies are critically assessed.

2.3.1 Existing current limitation strategies

2.3.1.1 Reference current saturation

This method is commonly used in the literature due to its simplicity. As given in Figure 2.13, the inner voltage PI controller provides the reference d - and q -axis currents to the inner current PI controller. These reference values are limited via saturation units when a fault occurs in the system. The upper and lower limits for the saturation units are $-I_{max}$ and I_{max} , where $I_{max} = \sqrt{I_{dmax}^2 + I_{qmax}^2}$ [127]. If the limitation of RMS current is required, the limits should be chosen as $\pm \frac{I_{max}}{\sqrt{2}}$.

Although this method is simple to implement, there are two important problems that should be considered.

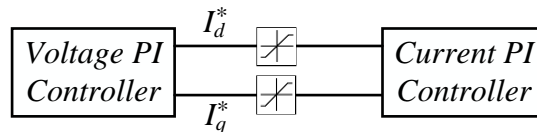


Figure 2.13: Reference current saturation concept.

1. Since the reference values of d - and q -axis currents are limited, this may not ensure that the instantaneous currents will be limited to those values.

2. The employment of saturation units can lead to the well-known integrator windup issue in the inner PI controllers and cause system instability [25, 124].

2.3.1.2 Virtual impedance-based algorithm

In this method, a virtual impedance is designed to decrease the voltage reference in case of faults so that the voltage controller does not send unrealistic values to the current controller [128]. There are three critical steps in the design process; over-current detection, virtual impedance calculation, and AC voltage drop computation, as shown in Figure 2.14 [123]. If the current magnitude violates the predefined threshold value, virtual impedance value is increased, and thus the voltage is decreased as explained in [123, 128]. However, this method may not guarantee the instantaneous current limitation since the maximum current value is chosen greater than the current threshold value [128]. Besides, since the process includes three steps, it may cause computational issues.

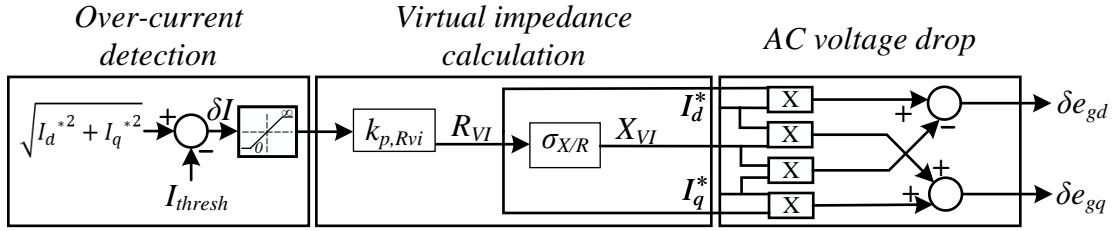


Figure 2.14: Virtual impedance based current limitation concept.

2.3.1.3 d -axis priority-based saturation method

This method is also based on the current reference saturation, but it has slightly different implementation. Instead of sending same reference values for both d - and q -axis currents, the d -axis current is prioritised via the dynamics given below [129, 130],

$$\begin{aligned}
 |I_{dref}| &= \min(I_{max}, |I_{dref}^*|) \\
 |I_{qref}| &= \min(\sqrt{I_{max}^2 - I_{dref}^2}, |I_{qref}^*|)
 \end{aligned} \tag{2.8}$$

If the inverter current magnitude reaches I_{max} under system faults, this mode is defined as current saturation mode; otherwise, the inverter works in current unsaturation mode [130]. Although anti-windup methods in inner PI loops can be employed to avoid the system instability, this method may still lead to current limit violation, and undesired responses in the transients [123, 130].

2.3.2 Circulating current prevention strategies

Power inverter devices are generally connected in parallel to deliver higher-level powers when required in MG applications [72, 121]. Therefore, in order to ensure reliable and stable parallel DER operations, the control algorithms of individual inverters should achieve several challenges, such as high-quality power supply, fast regulation of voltage and current, current limitation, and circulating current prevention among parallel-connected converters [46]. In general, different inverter filter and output impedance values can cause the circulating current issue [121, 122]. In this part, the existing methods to avoid circulating currents in MGs are critically examined.

The main reason behind the circulating current problem is improper active and reactive power control [16]. Therefore, modified droop controllers have been proposed for power-sharing purposes [131, 132]. However, since the droop control performance can be significantly affected by the inverter output impedances, the virtual impedance concept has been embedded to droop control to solve this issue [133]. In order to design accurate virtual impedances, the system parameters are generally required, but in reality, the system parameters may not be available, or they may change due to the environmental factors [121].

In [125], the circulating power problem has been related to the DC-link voltage increase. This paper has emphasized that the circulating power can cause undesired increases in the DC-link voltage, and therefore, the protection relays can be tripped to disable the inverters. To avoid this situation, a proportional derivative (PD) DC-link voltage controller has been designed for parallel-connected three-phase inverters in islanded mode.

To this end, even if the previously mentioned methods have examined the circulating current and power problems using different system configurations, they have not considered the current limitation issue under the system transients, such as islanded to grid-connected and grid-connected to islanded transitions, and short-circuits. Therefore, advanced control algorithms that can ensure circulating power prevention, current limitation, and system stability in parallel-connected inverters should be designed.

2.4 Stability and control issues in power converter-based DER systems

As the integration of power converter based DERs increase, conventional SGs, which possess large inertia and damping capabilities, are gradually being removed from the

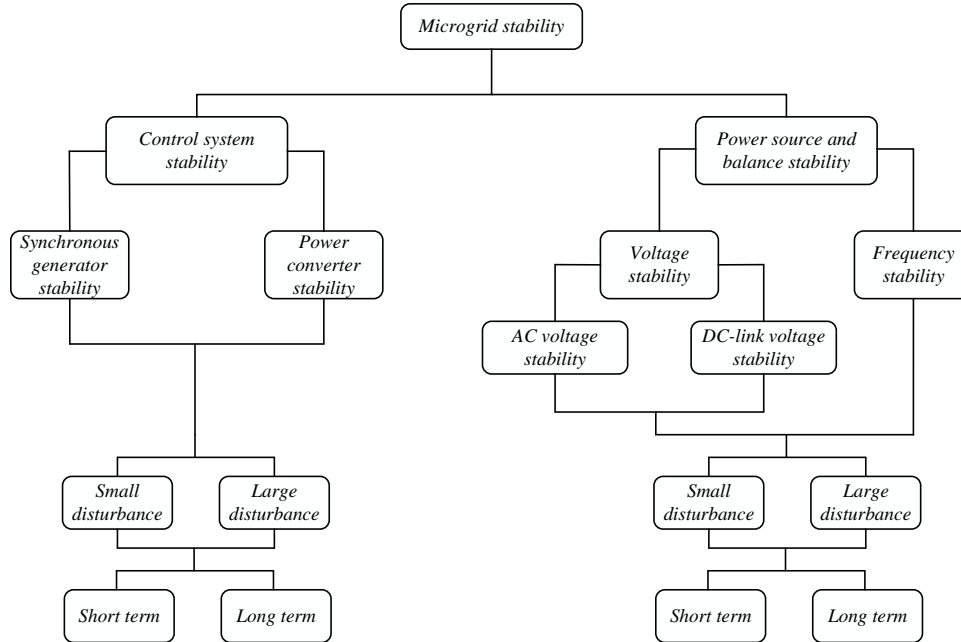


Figure 2.15: Classification of stability concepts in microgrids.

power networks, and power grids are evolving into the power converter dominated systems. This alteration will negatively affect the stability of traditional grid systems since grid systems require SGs as a power reserve in case of disturbances to achieve supply-demand balance and ensure voltage and frequency stability. Therefore, the stability and modeling of the power converter based MGs have become the key topics for reliable and sustainable future power grids [12, 11, 80].

The dynamics of the power converter based MGs exhibit distinctive, complex, and highly nonlinear behaviours compared to the traditional systems, so they can be sensitive against small and large system disturbances [134, 135]. Therefore, advanced control techniques should be designed, and rigorous stability analysis should be conducted to avoid undesired situations, such as hardware damages and power outages [136, 137, 138]. Besides, MGs can exist both in islanded and grid-connected cases, and their control systems should be able to achieve seamless transitions, fast synchronization with the grid, and economical source management without losing the system stability and unnecessarily tripping the protection relays [29, 139]. These control objectives are accomplished through a hierarchical control structure in different timescales, as briefly explained in the previous parts. Since the main focus of this thesis is designing advanced controllers for power inverters, in the next part, the issues that should be achieved in the primary control layer will be explained in detail.

The primary control includes the fastest control actions, and it is responsible

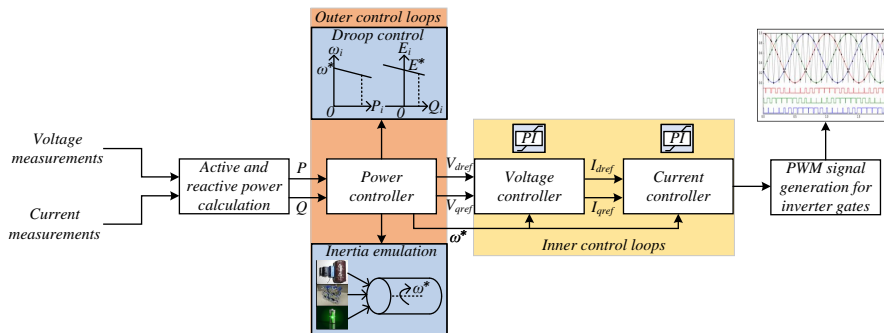


Figure 2.16: Commonly used cascaded inverter control scheme.

for power-sharing, voltage and frequency control, and inverter protection. Besides, primary control techniques should also support the grid voltage and frequency using droop control and virtual inertia methods in grid-connected mode and form the system voltage, and frequency employing grid-forming inverters in islanded mode [11, 140, 141]. In addition, since the RESs are intermittent sources and power flow can be bidirectional in some applications, DC voltage regulation, power balance, and device protection are other important issues that should be considered in the primary control layer. In order to achieve those tasks and ensure a reliable MG operation, the stability of individual power converters existing in MGs should be investigated under small and large faults. In Figure 2.15, MG stability concepts are summarised [11], and in the following part, these concepts will be briefly explained.

Power source and balance stability: MGs consist of converter-based DERs, and the main power supplies for these DERs are RESs. Since the RESs are intermittent sources, system voltage and frequency can be distorted if proper control algorithms and power reserves are not considered. For instance, in a grid-connected inverter operation, if the DC-link voltage is fluctuating more than the suggested levels, this can decrease the generated AC voltage quality by increasing the undesired harmonics and also cause higher frequency oscillations than the allowed limits. Therefore, DC-link voltage stability should be supported using bidirectional power converters, power reserves, such as capacitors and batteries, and virtual inertia and droop control algorithms [142, 143, 144]. Besides, the proposed techniques should ensure the system stability even under large disturbances, such as short-circuits, and support the grid according to the guidelines given by the related grid codes.

Control system stability: In the existing literature, a cascaded control scheme, as shown in Figure 2.16 [20, 145, 146] in synchronous rotating dq frame, is generally employed to control the power inverters. Inverter currents and PCC voltages are measured

and used to calculate the active and reactive powers. Then, either droop controllers or virtual inertia schemes serve as outer control loops to generate the voltage references for the inner voltage controller. Angular frequency (ω^*), which is required for dq transformation, can be obtained using PLL schemes or via droop and virtual inertia algorithms. The inner voltage controller sends the current reference values to the inner current controller. Finally, the PWM signals are generated to drive the inverter switches. PI controllers, whose outputs are limited, are mostly utilised in inner voltage, and current control loops [116, 130].

Poor tuning of controller gains and the slow dynamics of PLL schemes can lead to system instability in case of large system faults, such as short-circuits and mode transitions [95, 147, 148]. Besides, since the outputs of inner PI controllers are limited via saturation blocks, the integrator windup problem, which can be defined as the integrator swelling due to the addition of high error values, can occur and cause overshoots and system instability if the voltage sags are experienced or unrealistic reference values are transferred between the control loops [124, 149]. Thus, advanced controllers, which can inherently solve the integrator windup issue, are needed for the inverters to ensure a stable and reliable DER operation even under large and long term system disturbances.

2.5 Open challenges in the existing literature

As it has been emphasized in the literature review, power interface devices, particularly inverters, are critical for efficient, reliable, and stable power transfer between RESs and utility grids. Power inverters can enable high integration of RESs-based DERs into the grid if their control algorithms are properly designed, and accelerate the transition from traditional SG-based power grids to RESs-based future power grids. The control algorithms of inverters should ensure accurate control of active and reactive powers, support grid voltage and frequency even under severe grid faults, limit the system states (specifically inverter current) for hardware protection, prevent circulating powers between parallel inverters, and avoid unnecessary protection relay trips for a reliable DER operation. These control objectives are considered in the primary control layer using droop control and virtual inertia techniques. However, in the existing literature, the system stability is generally examined via root locus, eigenvalue, and bode analysis, which are valid only for the given (specific) system and controller parameters, may not result in analytic and generic stability conditions for design guidance, do not offer rigorous closed-loop stability analysis, and may not ensure the system stability in case

of large grid faults. Besides, current limitation is achieved via external saturation blocks used together with PI controllers, but this can lead to the swelling (windup) of integrator component and eventually the system instability when the power inverters have to operate in different equilibrium points. Therefore, advanced control techniques, which can inherently accomplish the tasks mentioned above under both normal and faulty conditions, and simplify the system dynamics and analysis, are required for both the grid-connected and islanded inverters. Below, the open challenges in the literature are summarised:

- Advanced control schemes that inherit the droop control concept, take into account the nonlinear dynamics of the inverters, and offer easy implementation are needed.
- Current limitation under large and long term disturbances should be included as an inherent feature to the grid-connected inverters. Advanced current-limiting controllers that can inherently solve the integrator windup problem should be designed.
- Grid voltage and frequency should be supported via controller algorithms according to the guidelines given by the grid codes, and grid synchronization should be ensured when the grid connection and disconnection occur.
- The negative impact of PLLs on the system stability should be avoided using PLL-less schemes.
- Closed-loop system stability should be rigorously investigated, and analytic stability conditions should be provided without assuming specific set of system and controller parameters to guide the potential designers.
- Virtual inertia and droop control methods should be combined to ensure power balance, frequency and voltage stability, and the interaction of this unified scheme with the grid-connected inverters should be investigated.
- The existing circulating current studies in parallel-connected inverters generally ignore the current-limiting property of individual inverters. Therefore, controllers that can prevent circulating current and limit the inverter current are required.
- Control schemes, which can ensure closed-loop system stability and grid synchronization in the islanded to grid-connected and grid-connected to islanded transitions, should be designed.

Chapter 3

Nonlinear control of three-phase grid-connected inverters

As mentioned in Chapter 2, the existing linear controllers may not implement the droop methods, and ensure the integrator-windup free current-limiting property and system stability at the same time for three-phase inverters in case of severe grid faults. Linear controllers assume specific set of system and controller parameters in the process of stability analysis, and they cannot ensure stable inverter operation if the system parameters or equilibrium points change. Besides, power inverter applications are highly dynamic due to the variable input source, load, and grid characteristics, and may require to operate for wide range of equilibrium points. In order to address these issues, the nonlinearities that exist in the dynamic equations of the power inverters should be considered and nonlinear controllers should be designed. Therefore, in this chapter, advanced nonlinear controllers for the three-phase grid-connected inverters are proposed. This chapter is divided into three sections, and each section focuses on solving specific issues related to the grid-connected three-phase inverters. In the first section, a nonlinear current-limiting controller is designed considering both inner and outer control loops as previously explained, and simulation results are provided [150]. In the second section, a PLL-less control scheme is introduced, closed-loop stability analysis is realised, and simulation studies are performed [151]. Finally, in the third section, a novel nonlinear droop controller is proposed for three-phase grid-supporting inverters that rigorously guarantee RMS inverter current limitation and closed-loop system stability under both normal grid conditions and balanced voltage sags. The effectiveness of the proposed method is compared with the existing techniques, extensive simulation and experimental studies are realised [152].

3.1 Nonlinear current-limiting controller for three-phase inverters

3.1.1 Background and motivations

As the integration of RESs-based units into the grid increases, power system stability has weakened due to the fluctuations in the supply and demand, which affect the frequency and voltage of the grid [153]. Thus, in order to increase the system reliability and realise large-scale utilization of DG units and seamless transition between islanded and grid-connected modes without violating the voltage and frequency limits [154], the design of advanced control methods for the inverter devices that integrate DG systems to the utility grid has major importance [52, 62, 155].

Although droop control has been used to manage the active and reactive power flows, in many studies, such as [141, 156, 157, 158], the nonlinear system dynamics are generally neglected, and the system stability analysis is conducted based on linearization techniques. Since linearization methods confine the stability regions of the systems, the nonlinear dynamics of a droop controlled grid-connected inverter should be considered to realise a rigorous stability analysis [23, 159].

The system stability and the protection of inverter switches and filters against high currents should be ensured in grid-connected DER applications. To embed the current limitation functionality to the inverters, additional saturation blocks or limiters [124, 128, 129] are mostly used in combination with the droop controller. However, these techniques can lead to system instability due to the integrator windup issue. This problem can be handled using anti-windup methods [160, 161], but most of the state-of-the-art anti-windup methods require information of the system parameters, which are generally unknown, and traditional anti-windup techniques cannot rigorously guarantee closed-loop system stability. To this end, a nonlinear current-limiting controller that overcomes these issues has been recently proposed for single-phase grid-connected inverters in [162, 163] and ensures current limitation without suffering from integrator windup under both normal and faulty grid conditions. However, this controller cannot be directly applied to three-phase inverters using the dq synchronously rotating reference frame modeling [52] and can only limit the current on the inverter side and not the grid-side, which can be desired in grid-connected applications.

Therefore, there is a need for designing a novel controller that can be applied to three-phase inverters connected to the grid and achieve a rigorous grid current limitation. Based on the synchronously rotating dq reference frame modeling of the inverter,

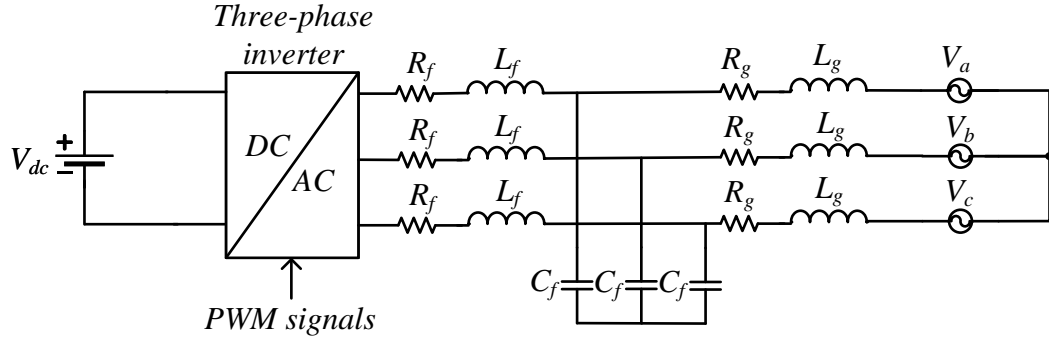


Figure 3.1: Grid-connected three-phase inverter with an LCL filter.

a novel controller is proposed in a cascaded control structure with two inner current and voltage loops and an outer power control loop (droop control). For the inner control loops, traditional PI controllers are used with decoupling terms to guarantee fast regulation of the inverter currents and voltages, as commonly done in three-phase inverter applications [116]. However, for the outer power loop, a new nonlinear droop controller is proposed with bounded voltage dynamics and constant virtual resistance to guarantee closed-loop system stability and the desired current limitation. Using nonlinear Lyapunov methods [164], the boundedness of the controller voltages are analytically proven and then using input-to-state stability, the d - and q -axis grid currents are proven to be limited below a given maximum value independently from each other or the power demand. Hence, the proposed controller introduces a droop control structure to support the voltage and frequency of the grid, and at the same time, maintains a limited injected current to the grid to protect the inverter under unrealistic power demands. This process is investigated in the sequel.

3.1.2 Problem statement and system modeling

The system under investigation is a three-phase grid-connected inverter that has an LCL filter at the output as shown in Figure 3.1. In this system, filter resistance, inductance and capacitance are shown as R_f , L_f , and C_f , grid-side resistance and inductance are shown as R_g and L_g , respectively. Inverter input voltage is given as V_{dc} , three-phase balanced grid-side voltages are given as V_a , V_b , and V_c . Considering the synchronously rotating dq frame [165], the dynamic equations of the system can be obtained as;

$$\frac{d}{dt}I_{fd} = -\frac{R_f}{L_f}I_{fd} + \omega I_{fq} + \frac{m_d}{2L_f}V_{dc} - \frac{V_{Cd}}{L_f} \quad (3.1)$$

$$\frac{d}{dt}I_{fq} = -\frac{R_f}{L_f}I_{fq} - \omega I_{fd} + \frac{m_q}{2L_f}V_{dc} - \frac{V_{Cq}}{L_f} \quad (3.2)$$

$$\frac{d}{dt}V_{Cd} = \frac{I_{fd}}{C_f} - \frac{I_{gd}}{C_f} + \omega V_{Cq} \quad (3.3)$$

$$\frac{d}{dt}V_{Cq} = \frac{I_{fq}}{C_f} - \frac{I_{gq}}{C_f} - \omega V_{Cd} \quad (3.4)$$

$$\frac{d}{dt}I_{gd} = -\frac{R_g}{L_g}I_{gd} + \omega I_{gq} - \frac{V_{gd}}{L_g} + \frac{V_{Cd}}{L_g} \quad (3.5)$$

$$\frac{d}{dt}I_{gq} = -\frac{R_g}{L_g}I_{gq} - \omega I_{gd} - \frac{V_{gq}}{L_g} + \frac{V_{Cq}}{L_g} \quad (3.6)$$

where, I_{fd} , I_{fq} and V_{Cd} , V_{Cq} represent d - and q -axis inverter currents and voltages, I_{gd} , I_{gq} show d - and q -axis grid currents. m_d and m_q are pulse width modulation (PWM) signals which are the control inputs of the system. The real and reactive power of the system can be calculated as below;

$$P = \frac{3}{2}(V_{Cd}I_{gd} + V_{Cq}I_{gq}), \quad Q = \frac{3}{2}(V_{Cd}I_{gq} - V_{Cq}I_{gd}). \quad (3.7)$$

As the system states are multiplied with each other in (3.7), the closed-loop system becomes nonlinear. Therefore, stability analysis should be realised using nonlinear control theory to provide a seamless operation for the inverter. To this end, the main aim of this section is to design a nonlinear droop controller that assures system stability and limits the grid currents below the given values. In the following part, the controller design process has been explained.

3.1.3 Controller design and analysis

In order to design the nonlinear droop controller for the inverter, a cascaded control structure that includes inner current and voltage control loops and an outer power control loop is adopted. For the inverter side currents and voltages, the inner loops introduce PI controllers with decoupling terms, while a novel nonlinear droop controller is proposed as the outer loop to limit the grid currents in dq reference frame, as presented below in detail.

3.1.3.1 Inner PI control loops

Based on the dq dynamic model of the grid-connected inverter, where m_d and m_q are the control inputs, the inner current controller that regulates the inverter currents I_{fd} and I_{fq} to the desired values I_{dref} and I_{qref} , respectively takes the form:

$$\begin{aligned} m_d &= \frac{(I_{dref} - I_{fd})(K_{pi} + \frac{K_{I_i}}{s}) + V_{Cd} - \omega L_f I_{fq}}{0.5V_{dc}} \\ m_q &= \frac{(I_{qref} - I_{fq})(K_{pi} + \frac{K_{I_i}}{s}) + V_{Cq} + \omega L_f I_{fd}}{0.5V_{dc}}. \end{aligned} \quad (3.8)$$

Here, a PI controller with additional decoupling terms is applied at the duty-ratio inputs m_d and m_q , while the reference values I_{dref} and I_{qref} are obtained from a voltage controller that can be expressed as:

$$\begin{aligned} I_{dref} &= (V_{Cdref} - V_{Cd})(K_{pv} + \frac{K_{I_v}}{s}) + I_{gd} - \omega C_f V_{Cq} \\ I_{qref} &= (V_{Cqref} - V_{Cq})(K_{pv} + \frac{K_{I_v}}{s}) + I_{gq} + \omega C_f V_{Cd}. \end{aligned} \quad (3.9)$$

The desired values for the capacitor voltages V_{Cdref} and V_{Cqref} are obtained from the outer power control loop. Assuming the current controller is much faster than the voltage controller (at least ten times as a rule of thumb) and the voltage controller is much faster than the power controller, the PI controller gains can be chosen using the pole placement method as commonly done in cascaded systems [166].

3.1.3.2 Proposed nonlinear controller (Outer loop)

Since the fast inner control loops have been extensively investigated in the literature [129] and [166], this part will focus on designing the outer droop control loop, which represents the novelty offered in this section. Based on the fast current and voltage controllers, it is considered that the capacitor voltages V_{Cd} and V_{Cq} are regulated to their reference values V_{Cdref} and V_{Cqref} in (3.5) and (3.6). Then, the proposed controller takes the form

$$V_{Cdref} = V_{gd} + E_d - r_v I_{gd} - \omega L_g I_{gq} \quad (3.10)$$

$$V_{Cqref} = V_{gq} + E_q - r_v I_{gq} + \omega L_g I_{gd}. \quad (3.11)$$

In (3.10) and (3.11), the parameters E_d and E_q represent two controllable voltage terms (controller states), while r_v acts as a positive constant virtual resistance. Inspired by

the universal droop control expressions [93], and the bounded controller proposed in [167], the controller states E_d and E_q are dynamically formed as

$$\dot{E}_d = c_d (K_e(E^* - V_C) - n(P - P_{set})) E_{dq}^2 \quad (3.12)$$

$$\dot{E}_{dq} = -\frac{c_d E_d E_{dq}}{E_{max}^2} (K_e(E^* - V_C) - n(P - P_{set})) - k_d \left(\frac{E_d^2}{E_{max}^2} + E_{dq}^2 - 1 \right) E_{dq} \quad (3.13)$$

$$\dot{E}_q = -c_q (\omega^* - \omega_g + m(Q - Q_{set})) E_{qq}^2 \quad (3.14)$$

$$\dot{E}_{qq} = \frac{c_q E_q E_{qq}}{E_{max}^2} (\omega^* - \omega_g + m(Q - Q_{set})) - k_q \left(\frac{E_q^2}{E_{max}^2} + E_{qq}^2 - 1 \right) E_{qq} \quad (3.15)$$

where E_{dq} , and E_{qq} are two additional control states and c_d , c_q , E_{max} , K_e , k_d , and k_q are positive constants. The expression $K_e(E^* - V_C) - n(P - P_{set})$ introduces the $P \sim V$ droop expression, which should be zero at the steady-state, and E^* is the rated RMS voltage of the grid, V_C is the RMS voltage of the filter capacitor given as $V_C = \sqrt{\frac{V_{Cd}^2 + V_{Cq}^2}{2}}$, P_{set} is the reference value of the real power and n is the real power droop coefficient. Similarly, $\omega^* - \omega_g + m(Q - Q_{set})$ represents the $Q \sim -\omega$ droop expression, where ω^* is the rated angular frequency, ω_g is the grid frequency, Q_{set} is the desired injected reactive power and m is the reactive power droop coefficient. The $P \sim V$ and $Q \sim -\omega$ droop expressions are adopted in this section due to the introduction of the virtual resistance r_v in the output via the proposed control design [93]. The initial conditions of the controller states E_d , E_{dq} , E_q , and E_{qq} are selected as 0, 1, 0, and 1, respectively, and the nonlinear dynamics (3.12)-(3.15) have been proposed in a way to guarantee the boundedness of the controller states E_d and E_q in the range $E_d, E_q \in [-E_{max}, E_{max}]$ as explained below.

For the controller dynamics (3.12) and (3.13), one can consider a Lyapunov function candidate as

$$W_d = \frac{E_d^2}{E_{max}^2} + E_{dq}^2 \quad (3.16)$$

(3.16) should be chosen considering a) $W_d > 0$ for all $E_d, E_{dq} \neq 0$, b) $W_d = 0$ only if $E_d, E_{dq} = 0$, and c) $\dot{W}_d \leq 0$ for all $E_d, E_{dq} \neq 0$ [164] to be used as a proper Lyapunov function candidate in the analysis.

The time derivative of (3.16) is

$$\dot{W}_d = \frac{2E_d \dot{E}_d}{E_{max}^2} + 2E_{dq} \dot{E}_{dq}. \quad (3.17)$$

By replacing (3.12) and (3.13) in (3.17), then

$$\dot{W}_d = -2k_d \left(\frac{E_d^2}{E_{max}^2} + E_{dq}^2 - 1 \right) E_{dq}^2. \quad (3.18)$$

As can be seen from (3.18), $\dot{W}_d = 0$ when $E_{dq} = 0$ or for every values of E_d and E_{dq} on the ellipse:

$$W_{d0} = \left\{ E_d, E_{dq} \in R : \frac{E_d^2}{E_{max}^2} + E_{dq}^2 = 1 \right\}. \quad (3.19)$$

Based on the initial conditions of the controller states, E_d and E_{dq} will always stay on the ellipse W_{d0} as mathematically expressed below:

$$\dot{W}_d = 0 \Rightarrow W_d(t) = W_d(0) = 1, \quad \forall t \geq 0. \quad (3.20)$$

Hence, $E_d \in [-E_{max}, E_{max}]$, $\forall t \geq 0$. By considering the transformation

$$E_d = E_{dmax} \sin \phi \quad \text{and} \quad E_{dq} = \cos \phi \quad (3.21)$$

then taking into account (3.12)-(3.13), E_d and E_{dq} will remain on the ellipse W_{d0} with an angular velocity

$$\dot{\phi} = \frac{c_d (K_e (E^* - V_C) - n(P - P_{set})) E_{dq}}{E_{max}}. \quad (3.22)$$

From (3.22), when $K_e (E^* - V_C) - n(P - P_{set})$ is zero, the angular velocity becomes zero and the controller states can converge to the desired equilibrium point defined by the $P \sim V$ droop control. Considering a similar analysis for the controller dynamics (3.14)-(3.15), then E_q and E_{qq} are proven to remain on a similar ellipse

$$B_{q0} = \left\{ E_q, E_{qq} \in R : \frac{E_q^2}{E_{max}^2} + E_{qq}^2 = 1 \right\} \quad (3.23)$$

and travel with an angular velocity

$$\dot{\psi} = \frac{-c_q (\omega^* - \omega_g + m(Q - Q_{set})) E_{qq}}{E_{max}}. \quad (3.24)$$

Therefore, the $Q \sim -\omega$ droop can be implemented in a similar way, while E_q satisfies $E_q \in [-E_{max}, E_{max}] \forall t \geq 0$. It should be noted that, the proposed controller can easily change from the droop control to accurate regulation of P and Q at their reference values by removing the term $K_e (E^* - V_C)$ from (3.12)-(3.13) and the term $(\omega^* - \omega_g)$

from (3.14)-(3.15). Thus, real and reactive power can be set to their desired values at any time, and transition between the two modes can be seamlessly realised.

3.1.4 Stability analysis and current-limiting proof

By implementing the proposed controller (3.10)-(3.11) into the grid-side current equations (3.5)-(3.6) and taking into account the fast regulation of the inner current and voltage loops, the closed-loop grid-side current equations are expressed as

$$L_g \frac{dI_{gd}}{dt} = -(R_g + r_v)I_{gd} + E_d \quad (3.25)$$

$$L_g \frac{dI_{gq}}{dt} = -(R_g + r_v)I_{gq} + E_q. \quad (3.26)$$

It is clear that the dynamics of I_{gd} and I_{gq} can be handled independently taking into account that $E_d, E_q \in [-E_{max}, E_{max}]$ for all $t \geq 0$, as proven in the previous subsection. Hence for d -axis grid current dynamics (3.25), one can consider the Lyapunov function candidate as

$$V = \frac{1}{2}L_g I_{gd}^2. \quad (3.27)$$

The time derivative of (3.27) is calculated using (3.25) as

$$\dot{V} = -(R_g + r_v)I_{gd}^2 + E_d I_{gd} \leq -(R_g + r_v)I_{gd}^2 + |E_d||I_{gd}|. \quad (3.28)$$

Thus,

$$\dot{V} < 0, \forall |I_{gd}| > \frac{|E_d|}{R_g + r_v} \quad (3.29)$$

which proves that system (3.25) is input-to-state stable by considering E_d as the input. Since it is proven that $|E_d| \leq E_{max}, \forall t \geq 0$, then I_{gd} will be bounded for all $t \geq 0$. In particular, if initially $|I_{gd}(0)| \leq \frac{E_{max}}{R_g + r_v}$, then from the input-to-state stability analysis, there is

$$|I_{gd}(t)| \leq \frac{E_{max}}{R_g + r_v}, \forall t \geq 0. \quad (3.30)$$

In order to limit the current I_{gd} below a maximum value I_{max} , the controller parameters E_{max} and r_v can be selected to satisfy

$$E_{max} = (R_g + r_v)I_{max}. \quad (3.31)$$

By substituting (3.31) into (3.30), it is proven that

$$|I_{gd}(t)| \leq I_{max}, \quad \forall t \geq 0, \quad (3.32)$$

which proves the desired current-limiting property. A similar approach for the q -axis grid current dynamics (3.26) can be applied to show that if initially it holds true that $|I_{gq}(0)| \leq \frac{E_{max}}{R_g+r_v}$, then

$$|I_{gq}(t)| \leq I_{max}, \quad \forall t \geq 0. \quad (3.33)$$

As a result, the grid d - and q -axis currents are proven to remain below a defined maximum value I_{max} independently from each other or the nonlinear droop control expressions by selecting the controller parameters E_{max} and r_v according to (3.31). This is achieved without using any saturation units, which is a common approach in conventional controllers and can lead to instability [124, 129]. Since the current-limiting property is achieved using nonlinear Lyapunov theory and input-to-state stability analysis, then the grid current limitation is guaranteed at all times, even during transients. In low voltage applications, since the value of filter capacitors are small, grid-side and inverter-side currents are almost equal. Limiting any of them can ensure the safe converter operation. Therefore, in this section, grid-side current limitation is preferred. It is worth mentioning that if $|I_{gd}| \rightarrow I_{max}$ or $|I_{gq}| \rightarrow I_{max}$, then $|E_d| \rightarrow E_{max}$ or $|E_q| \rightarrow E_{max}$, respectively, which leads $E_{dq} \rightarrow 0$ or $E_{qq} \rightarrow 0$ since the controller states are restricted on the ellipses W_{d0} and B_{q0} . Then, from (3.12) and (3.14), it becomes clear that $\dot{E}_d \rightarrow 0$ and $\dot{E}_q \rightarrow 0$, which proves that the integration slows down near the limits resulting in an inherent anti-windup property of the proposed controller. This highlights the superiority of the proposed controller with respect to the existing approaches that introduce saturation limits and require additional anti-windup mechanisms that further complicate the controller implementation and closed-loop system stability analysis.

Table 3.1: System and controller parameters for the examined inverter system

Parameters	Values	Parameters	Values
L_f, L_g	$0.0139H$	C_f	$1.8186\mu F$
R_f, R_g	0.8752Ω	r_v	2Ω
n	0.0661	m	0.0019
ω_g	$2\pi 49.97$	k_d, k_q	1
V_{dc}	$700V$	I_{max}	$2.5A$
K_{Pi}, K_{Ii}	$0.3, 10$	K_{Pv}, K_{Iv}	$2, 10$
K_e	10	ω^*	$2\pi 50$
c_d	0.65	c_q	22.5
E^*	$218V$	E_{max}	7.188
V_{gd}	$220\sqrt{2}V$	V_{gq}	$0V$

3.1.5 Simulation results

In order to validate the effectiveness of the proposed control strategy, a three-phase grid-connected inverter is simulated using the Matlab/Simulink software. The system and controller parameters are given in Table 3.1. In this section, the main aim is to illustrate that the proposed controller can change between set mode, i.e. accurate real and reactive power regulation and droop control mode and at the same time limits the grid currents when an unrealistic power reference value is provided to the controller.

Initially, the set control mode is enabled by removing the terms $K_e(E_d^* - V_{Cd})$ and $(\omega^* - \omega_g)$ from (3.12)-(3.13) and (3.14)-(3.15), respectively, where P_{set} and Q_{set} are set to zero. At the time instant $t = 1s$, the active power reference value P_{set} changes to $400W$ and at $t = 2s$, it is further increased to $1650W$. As it can be seen from Figure 3.2, initially P is regulated to the desired $400W$, but when P_{set} becomes very high, the proposed controller regulates the real power to a lower value. This is because the current I_{gd} tries to violate its maximum value $I_{max} = 2.5A$ as shown in Figure 3.3, and the proposed controller maintains the desired current limitation to protect the inverter under unrealistic power demands. However, the reactive power is always regulated to the desired zero value and the current I_{gq} also remains limited below its maximum value. At $t = 3s$, P_{set} is decreased to $800W$ and the real power is regulated to the desired value after a short transient. At the time instant $t = 4s$, the reactive power reference Q_{set} increases to $200Var$ and at $t = 5s$ it changes to $400Var$ to verify the ability of the controller to regulate the reactive power. As it can be seen from Figure 3.2, the reactive power injected by the inverter is accurately regulated to both reference values. The $P \sim V$ droop control is enabled at $t = 7s$, and the real power

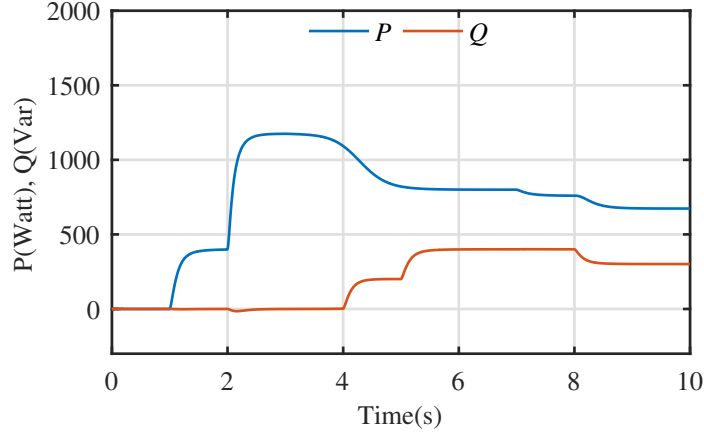


Figure 3.2: System active and reactive powers.

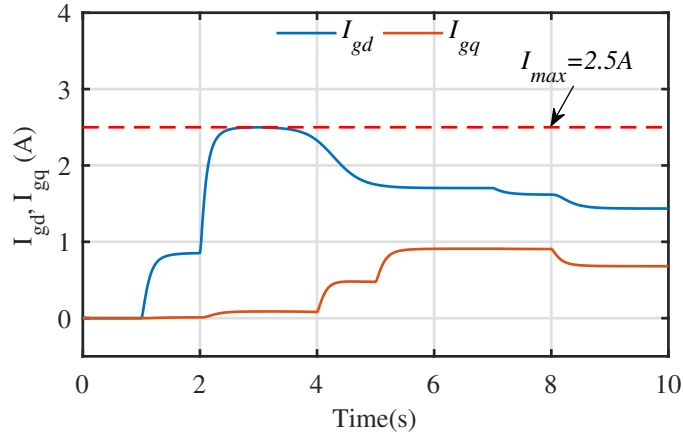


Figure 3.3: d - and q -axis grid currents.

decreases to 760 W in order to regulate the RMS voltage V_C closer to the rated E^* . The response of the system states V_{Cd} and V_{Cq} , which define the RMS voltage value V_C as $V_C = \sqrt{\frac{V_{Cd}^2 + V_{Cq}^2}{2}}$, are shown in Figures 3.4 and 3.5. At $t = 8\text{ s}$, the $Q \sim -\omega$ droop control is enabled and the reactive power is decreased to 301 Var since the frequency of the grid ω_g is slightly lower than the rated ω^* , as given in the parameters of Table 3.1. Hence, both accurate regulation of the real and reactive power and droop control modes can be implemented by the proposed nonlinear controller with an inherent grid current limitation that protects the inverter from unrealistic values of the power demand.

In order to verify the theoretic analysis, the trajectory of the controller states E_d , E_{dq} and E_q , E_{qq} is plotted on the E_d - E_{dq} and E_q - E_{qq} planes, respectively, in Figure 3.6 for the entire simulation. One can easily observe that the controller states remain on the corresponding ellipses W_{d0} and B_{q0} , which are the same in this case. From the controller analysis, as the state E_{dq} tends to zero, the state E_d reaches its maximum

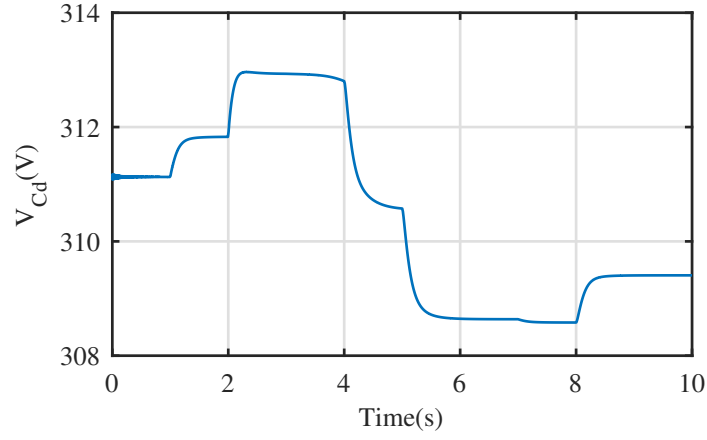


Figure 3.4: d -axis capacitor voltage.

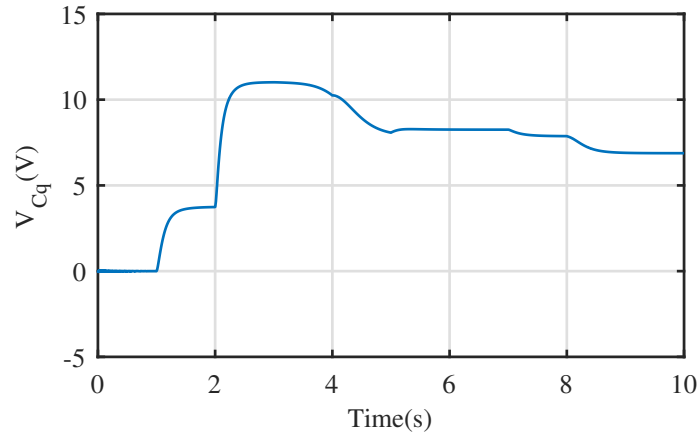


Figure 3.5: q -axis capacitor voltage.

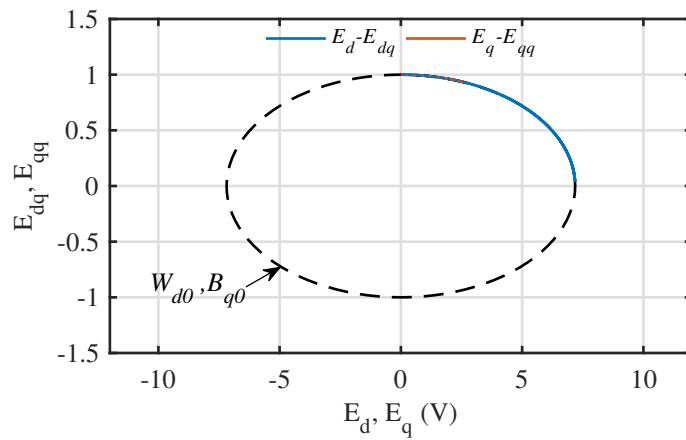


Figure 3.6: The trajectories of the controller states E_d , E_{dq} , E_q , and E_{qq} .

value E_{max} , as shown in Figure 3.6, leading to the current-limiting property for I_{gd} . Since I_{gq} does not reach its upper limit as shown in Figure 3.3, then the trajectory of

the controller states E_q and E_{qq} remains on the top of the ellipse B_{q0} and is regulated at the corresponding steady-state values depending on the reference value Q_{set} and the $Q \sim -\omega$ droop. It should be noted that the regulation speed of the controller can be affected by the choice of integral gains c_d and c_q . If faster regulation is required, the gains can be increased without the concern of current limit violation since current limitation is proven independently of the controller gains.

3.2 PLL-less three-phase inverters with current-limiting property

In the previous section, a nonlinear controller is proposed for three-phase grid-connected inverters, and comprehensive analysis of the controller dynamics and current-limiting property is provided. However, the closed-loop stability of the entire system has not been examined. In this section, a novel droop control method for three-phase grid-connected inverters is proposed to guarantee closed-loop system stability and an inherent current-limiting property without the need for a PLL. This current limitation is guaranteed independently of the grid, line and filter parameters, thus increasing the controller robustness. In addition, asymptotic stability of the desired equilibrium point of the closed-loop system is guaranteed under different values of the proposed controller gain.

3.2.1 Background and motivations

The control of real and reactive power injected into the grid can be achieved separately by introducing additional terms in the droop control structure to remove their coupling [88], while virtual impedance methods can also be added to affect the inverter output or line impedance in order to enhance the stability of the grid [93]. As mentioned in Chapter 2, depending on the type of the output impedance, the droop expressions can take the form of $P \sim \omega/Q \sim V$ (inductive impedance) and $P \sim V/Q \sim \omega$ (resistive impedance), and they are used to support the local voltage and frequency of the system at the point of common coupling (PCC) [130], while a line is generally considered between the PCC and the utility grid.

Grid synchronization is one of the most critical issues that requires special attention in grid-connected applications to maintain a stable and reliable inverter-based DER operation [167, 168]. In the synchronization process, several techniques such as Kalman Filter, nonlinear least square, and phase-locked loops (PLL) can be employed.

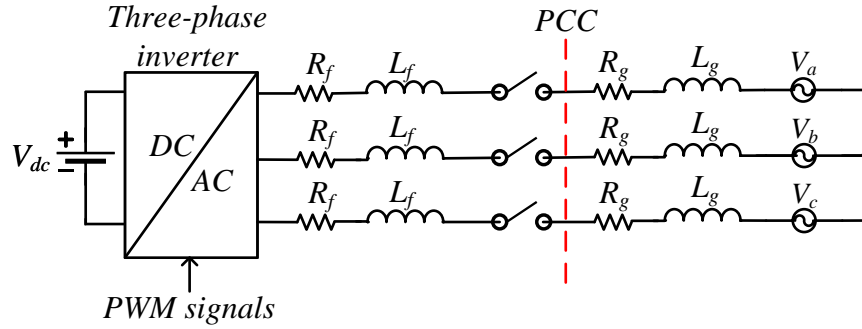


Figure 3.7: Three-phase grid-connected inverter with an L filter.

Due to its easy implementation and simplicity, the most commonly used method is the PLL. Although PLLs can ensure stable operation under normal grid conditions, it has been shown in the literature that they can lead to undesirable phenomena and instability of the system under grid disturbances [169]. In order to avoid the negative effects of PLLs, self-synchronization algorithms have been recently proposed and can be integrated into the droop control [107, 163].

To increase the reliability of the grid-connected inverter operation and satisfy the requirements imposed by the grid codes [29, 77], the interaction between the inverter and grid should be managed by considering the protection and stability issues [28, 170]. For instance, when injecting power to the grid, the system states such as voltage, current and frequency should be limited for stability and inverter protection reasons. Specifically, the current limitation is of significant importance under grid faults or sudden changes in supply, demand or the desired reference signal received from a supervisory control. In order to address the current limitation problem, the bounded integral controller [167] using nonlinear input-to-state stability theory has been proposed and it has been successfully implemented to limit the system current in both three-phase [171] and single-phase applications [162]. Nevertheless, asymptotic stability of the closed-loop system to a desired equilibrium point has not been proven yet for a three-phase inverter connected to the PCC, while a PLL is often required for the implementation that reduces the system reliability.

In this section, a novel nonlinear current-limiting droop controller for a three-phase inverter connected to the grid through a filter and a distribution line is proposed without the need for a PLL. The proposed controller supports the voltage and frequency of the PCC and inherently limits the current of the inverter using only the local measurements of the PCC independently from unrealistic values of the reference power. The desired current limitation is mathematically proven using nonlinear uli-

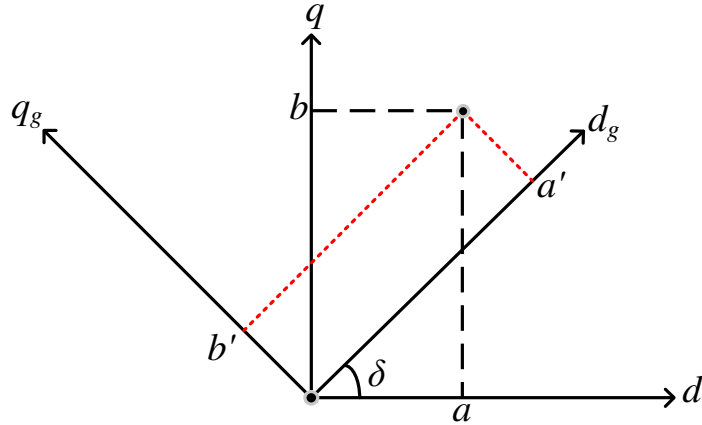


Figure 3.8: Axis transformation.

mate boundedness theory, and the closed-loop asymptotic stability is examined using small-signal model analysis. The system is modeled using the synchronous rotating (dq) frame, and for the stability analysis, a global-to-local axis transformation is used to investigate the asymptotic convergence to a desired equilibrium point [27]. The controller design process is thoroughly explained in the following subsections.

3.2.2 Problem definition and system dynamics

The system under consideration is a three-phase inverter connected to a point of common coupling (PCC) through a filter, as demonstrated in Figure 3.7. The filter resistance and inductance are described as R_f and L_f , respectively, whereas the line between the PCC and the main grid has a resistance R_g and inductance L_g . The inverter DC input voltage is expressed as V_{dc} , and the three-phase grid voltages are given as

$$\begin{bmatrix} V_a \\ V_b \\ V_c \end{bmatrix} = \begin{bmatrix} V_m \cos(\omega_g t) \\ V_m \cos(\omega_g t - 120^\circ) \\ V_m \cos(\omega_g t + 120^\circ) \end{bmatrix}, \quad (3.34)$$

with V_m and ω_g being the grid voltage amplitude and frequency, respectively.

In order to realise the system analysis, an algebraic axis transformation [27] is used to align the grid and inverter voltages as shown in Figure 3.8. The algebraic

transformation is given below [27]:

$$\begin{bmatrix} a \\ b \end{bmatrix} = \begin{bmatrix} \cos(\delta) & -\sin(\delta) \\ \sin(\delta) & \cos(\delta) \end{bmatrix} \begin{bmatrix} a' \\ b' \end{bmatrix}. \quad (3.35)$$

In this context, (3.35) is referred as global-to-local transformation, where δ represents the rotation angle. If the rotation is counterclockwise then $\delta > 0$, and if it is clockwise, as in the proposed system, then $\delta < 0$. For the clockwise case, the rotation matrix (3.35) (after δ is replaced with $-\delta$) becomes

$$\begin{bmatrix} \cos(\delta) & \sin(\delta) \\ -\sin(\delta) & \cos(\delta) \end{bmatrix}, \quad (3.36)$$

where $\delta = \theta - \theta_g$, which represents the difference between the inverter and grid angles. Assuming that the PCC voltage is aligned on the d_g -axis of the global dq reference frame and neglecting the small voltage drop and phase shifting caused by the line, i.e. $V'_{gd} = V_m$ and $V'_{gq} = 0$, then by using the inverse of the rotation matrix (3.36), the inverter side equivalence of the PCC voltages can be found as

$$\begin{bmatrix} V_{gd} \\ V_{gq} \end{bmatrix} = \begin{bmatrix} V_m \cos(\delta) \\ -V_m \sin(\delta) \end{bmatrix}. \quad (3.37)$$

As a result, the three-phase dynamics in the local dq reference frame are expressed as

$$L_f \frac{dI_d}{dt} = -R_f I_d + \omega L_f I_q - V_{gd} + V_d \quad (3.38)$$

$$L_f \frac{dI_q}{dt} = -R_f I_q - \omega L_f I_d - V_{gq} + V_q \quad (3.39)$$

where I_d, I_q and V_d, V_q represent the dq frame inverter currents and voltages. Active power (P) and reactive power (Q) can be calculated as in [27]

$$P = \frac{3}{2} (V_{gd} I_d + V_{gq} I_q) \quad Q = \frac{3}{2} (V_{gq} I_d - V_{gd} I_q). \quad (3.40)$$

It is clear from (3.37) and (3.40) that the P and Q expressions include nonlinear terms, and any control method that controls the real and reactive power injected by the inverter, such as the droop control method, will result in a nonlinear closed-loop system. Therefore, nonlinear control theory should be considered to prove key system features, such as current limitation, and guarantee a reliable inverter operation. To this end, the main aim of this section is to design a nonlinear controller which limits the

system current even when there is excessive power demand and ensure system stability at all times.

Remark: Since the value of the grid-side line inductance is relatively small, this results in a small voltage drop and phase shift between the grid and PCC voltages; hence these can be assumed as almost equal and constant under the assumption of stiff grid. However, further analysis can be required if the grid is non-stiff.

3.2.3 Proposed nonlinear controller

The main focus of this section is to design a nonlinear controller which limits the injected inverter current and realises the desired power droop functions without the need for a PLL. For this purpose, the local inverter voltages (V_d and V_q), which represent the control inputs of the system, are proposed to take the form

$$V_d = V_{gd} + E_d - r_v I_d - \omega L_f I_q \quad (3.41)$$

$$V_q = V_{gq} - r_v I_q + \omega L_f I_d \quad (3.42)$$

where E_d and r_v act as a controllable virtual voltage, and a constant virtual resistance, respectively. Motivated by the recently proposed bounded integral controller [167], the E_d dynamics of the proposed nonlinear controller are defined as

$$\dot{E}_d = c_d [(E^* - V_{rms}) - n(Q - Q_{set})] E_{dq}^2 \quad (3.43)$$

$$\dot{E}_{dq} = -c_d \frac{E_d E_{dq}}{E_{max}^2} [(E^* - V_{rms}) - n(Q - Q_{set})] - \left(\frac{E_d^2}{E_{max}^2} + E_{dq}^2 - 1 \right) E_{dq} \quad (3.44)$$

where E_{dq} is the additional controller state to create a two-dimensional plane with E_d as in [167], while c_d and E_{max} are positive constants related to the dynamics of the bounded integral controller. The initial conditions of the controller states are selected as $E_{d0} = 0$ and $E_{dq0} = 1$. The proposed control dynamics has been suitably designed to guarantee that the controller states remain bounded in the ranges $E_d \in [-E_{max}, E_{max}]$ and $E_{dq} \in [0, 1]$. For the proof of the boundedness, the analysis provided in [163, 167, 171] can be referred. Note that if the expression $(E^* - V_{rms}) - n(Q - Q_{set})$ becomes zero at the steady-state in the proposed controller then the $Q \sim V$ droop control is realised. E^* is the nominal RMS grid voltage, V_{rms} is the inverter RMS voltage calculated as $V_{rms} = \sqrt{\frac{V_{gd}^2 + V_{gq}^2}{2}} = \frac{V_m}{\sqrt{2}}$, Q_{set} is the reactive power reference value and n is the reactive power droop coefficient. Finally, the $P \sim \omega$ droop is accomplished independently from the controller dynamics (3.43) and (3.44) and employed through

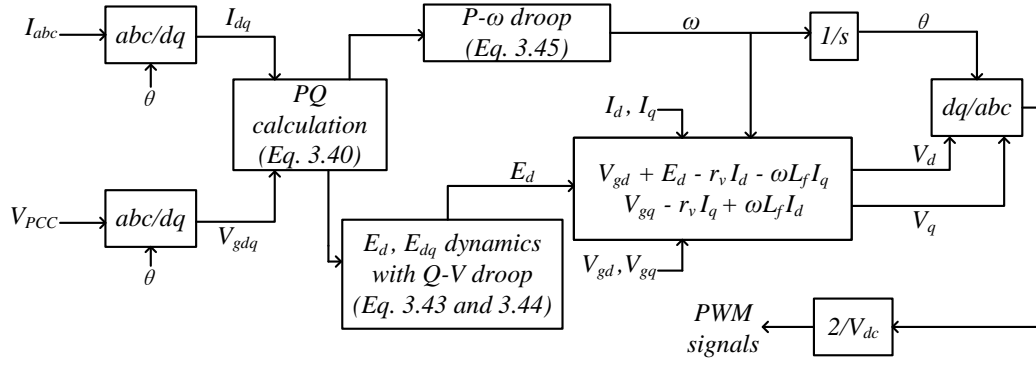


Figure 3.9: Implementation diagram of the proposed controller.

the expression

$$\omega = \omega^* - m(P - P_{set}) \quad (3.45)$$

where ω is the inverter angular frequency which is used in the dq transformation, ω^* is the nominal angular frequency, m is the active power droop coefficient, and P_{set} is the active power reference value. Note that since only the local variables are used in the power calculation and the controller dynamics, then the proposed design does not require any information after the PCC. Additionally, before connecting to the grid, there is $E_d = E_{d0} = 0$, $I_d = I_q = 0$ and hence from (3.41) and (3.42) there is $V_d = V_{gd}$ and $V_q = V_{gq}$ which can be equivalently implemented using the abc quantities without a PLL. Hence, a PLL is not needed either before or after the grid connection as illustrated in the implementation diagram in Figure 3.9.

3.2.4 Current-limiting property and closed-loop stability analysis

3.2.4.1 Current-limiting property

The closed-loop system can be obtained by replacing the proposed controller dynamics (3.41) and (3.42) in the inverter dynamics (3.38) and (3.39) as

$$L_f \frac{dI_d}{dt} = -(R_f + r_v)I_d + E_d \quad (3.46)$$

$$L_f \frac{dI_q}{dt} = -(R_f + r_v)I_q \quad (3.47)$$

From (3.47), it becomes clear that if initially $I_q(0) = 0$ then $I_q(t) = 0, \forall t \geq 0$. Hence, in order to guarantee the desired current limitation, it is sufficient to prove using nonlinear control theory that only the d -axis current (I_d) will be limited at all times below a given value I_{max} . For this purpose, if the energy stored in the filter inductor is used as a candidate Lyapunov function

$$V = \frac{1}{2}L_f I_d^2, \quad (3.48)$$

the time derivative of (3.48) can be calculated using (3.46) as

$$\begin{aligned} \dot{V} &= -(R_f + r_v)I_d^2 + E_d I_d \\ &\leq -(R_f + r_v)I_d^2 + |E_d| |I_d|. \end{aligned} \quad (3.49)$$

Since $E_d \in [-E_{max}, E_{max}]$ from the boundedness of the controller states, then (3.49) can be written as,

$$\dot{V} \leq -(R_f + r_v)I_d^2 + E_{max} |I_d| \quad (3.50)$$

Thus,

$$\dot{V} \leq -R_f I_d^2, \forall |I_d| \geq \frac{E_{max}}{r_v} \quad (3.51)$$

According to theorem 4.18 [164], it is proven that the solution $I_d(t)$ of (3.46) is ultimately bounded. In this theorem, although initially the system states do not need be inside the given bound, after a t time, they will enter the bounded area and stay there. However, if initially the system current is chosen such that $|I_d(0)| \leq \frac{E_{max}}{r_v}$, then it can be resulted that

$$|I_d| \leq \frac{E_{max}}{r_v}, \forall t \geq 0. \quad (3.52)$$

In order to limit the current I_d below a maximum value I_{max} , then the controller parameters E_{max} and r_v can be chosen to meet the expression

$$E_{max} = r_v I_{max}. \quad (3.53)$$

If (3.53) is replaced in (3.52), it is verified that

$$|I_d| \leq I_{max}, \forall t \geq 0, \quad (3.54)$$

which confirms the desired current-limiting property. The main idea is that the trajectories starting in a specified bounded neighbourhood will remain there bounded in time.

From the above ultimate boundedness proof, it is clear that the limitation of the inverter current is guaranteed independently of the system variables, such as the grid frequency and voltage or the parameters of the filter and the line. In addition, the current-limiting property is guaranteed during the entire grid-connected inverter operation, even during transients. In contrast to the existing approaches in the literature that use additional saturation units and might suffer from integrator windup and instability [116, 124], here the proposed controller introduces an inherent anti-windup property due to the bounded integral control structure, thus facilitating the stability analysis of the closed-loop system, which is provided in the sequel.

3.2.4.2 Small-signal stability analysis

Although the current-limiting property is proven analytically in the previous section using nonlinear systems theory, the asymptotic stability of the closed-loop to a desired equilibrium point has not been examined, yet. Therefore, this part emphasizes on evaluating the asymptotic performance of the proposed controller using small-signal stability analysis for a three-phase grid-connected inverter. After adding the controller states (3.43) and (3.44) into the system and considering $\dot{\delta} = \omega - \omega_g = \Delta\omega$, the state vector of the closed-loop system becomes $x = [I_d \ E_d \ \delta \ I_q \ E_{dq}]^T$. Consider an equilibrium point $x_e = [I_{de} \ E_{de} \ \delta_e \ I_{qe} \ E_{dqe}]^T$, where $E_{de} \in (-E_{max}, E_{max})$ and $E_{dqe} \in (0, 1]$. Then, the Jacobian matrix of the closed-loop system can be constructed as in (3.55) using the equations (3.43)-(3.47) via *Lyapunov's indirect method* by following the steps given in [164]. As can be understood from (3.47) and the system Jacobian matrix (3.55) that the q -axis current I_q is controlled to be 0 and results in a negative eigenvalue $-\frac{(R_f + r_v)}{L_f}$. Similarly, the term $-2E_{dqe}^2$ is always negative, since E_{dqe} is considered to be in the range $E_{dqe} \in (0, 1]$. To this end, the equilibrium point x_e of the closed-loop system will be asymptotically stable, if the eigenvalues of the matrix J_T (3.57) have negative real

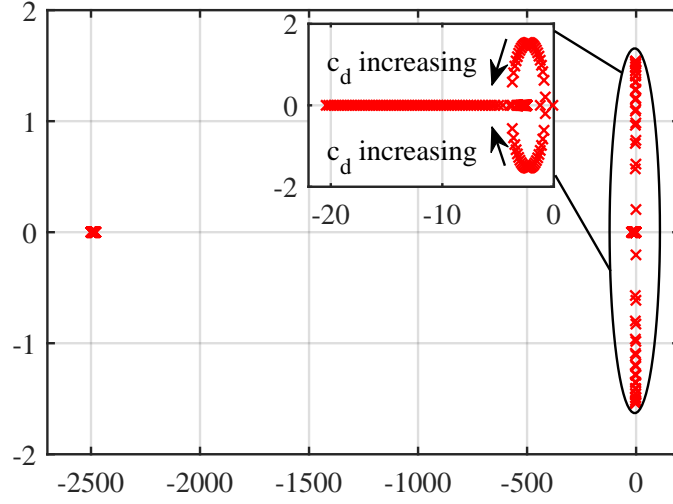


Figure 3.10: Closed-loop system eigenvalues as a function of controller gain c_d with $0.1 \leq c_d \leq 50$

parts.

$$J = \begin{bmatrix} J_T & 0_{3 \times 1} & 0_{3 \times 1} \\ 0_{1 \times 3} & -\frac{(R_f + r_v)}{L_f} & 0 \\ C_{1 \times 3} & 0 & -2E_{dqe}^2 \end{bmatrix} \quad (3.55)$$

$$C^T = \begin{bmatrix} -\frac{3c_d E_{de} E_{dqe} V_m \sin \delta_e}{2E_{max}^2} \\ \frac{-2E_{de} E_{dqe}}{E_{max}^2} \\ -\frac{3c_d E_{de} E_{dqe} V_m \cos \delta_e}{2E_{max}^2} \end{bmatrix} \quad (3.56)$$

$$J_T = \begin{bmatrix} -\frac{(R_f + r_v)}{L_f} & \frac{1}{L_f} & 0 \\ A \sin \delta_e & 0 & A i_{de} \cos \delta_e \\ -B \cos \delta_e & 0 & B i_{de} \sin \delta_e \end{bmatrix} \quad (3.57)$$

In the matrix J_T , the terms A and B are given as $\frac{3}{2}V_m c_d n E_{dqe}^2$ and $\frac{3}{2}mV_m$, respectively. In order to calculate the equilibrium point values of I_{de} , E_{de} , δ_e and E_{dqe} , the equations (3.43), (3.44), (3.45), and (3.46) can be used. In Figure 3.10, a root locus analysis is realised by changing the controller gain c_d between 0.1 and 50 using the system parameters provided in Table 3.2. Contrary to [26] which assumes the equilibrium points are constant while changing the droop coefficients, the controller

Table 3.2: System and controller parameters for the simulation studies

Parameters	Values	Parameters	Values
L_f, L_g	$2.2mH$	S_{max}	$3300VA$
R_f, R_g	0.5Ω	r_v	5Ω
n	0.0167	m	9.52×10^{-4}
ω^*	$2\pi 50$	V_{dc}	$700V$
E_{max}	27.5	I_{max}	$5A$
c_d	15	E^*	$220V$

gain c_d changes only the convergence rate of the system states to the equilibrium points. As it can be easily observed, the closed-loop system stability is guaranteed for any value of the controller gain in the given range verifying the effectiveness of the proposed controller to both limit the inverter current and regulate the system at the desired equilibrium point. It should be noted that the filter capacitor and grid-side line dynamics have not been included into the system analysis. Although current-limiting property is independent of these dynamics as proven in the previous part, their effects on system stability need further investigation.

3.2.5 Simulation results

To validate the performance of the proposed controller, a three-phase inverter connected to the grid through a filter and a line (Figure 3.7) is simulated using the Matlab/Simulink software. The implementation diagram of the proposed controller is provided in Figure 3.9 and the simulation parameters are given in Table 3.2. The main aims in this part are:

- To verify the desired droop control operation and convergence to the desired equilibrium points under changes of the real and reactive power references.
- To illustrate that the inverter currents can never exceed the defined upper limit even under extreme power demands.

During the operation, droop control is implemented for both active and reactive power. Initially, the accurate active power regulation is achieved since $\omega_g = \omega^*$, while the $Q \sim V$ droop is enabled for the reactive power as explained in the controller design. At the time instant $t = 0$, P is set to $1000W$ and Q is set to $1000Var$. However, even if P is regulated exactly at P_{set} as expected when $\omega_g = \omega^*$, Q is regulated to a lower value that can be calculated using $\frac{E^* - V_{rms}}{n} + Q_{set}$. The change in the RMS voltage of the

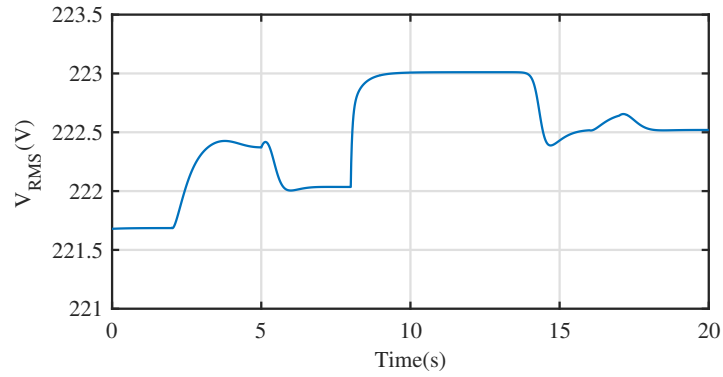


Figure 3.11: RMS voltage.

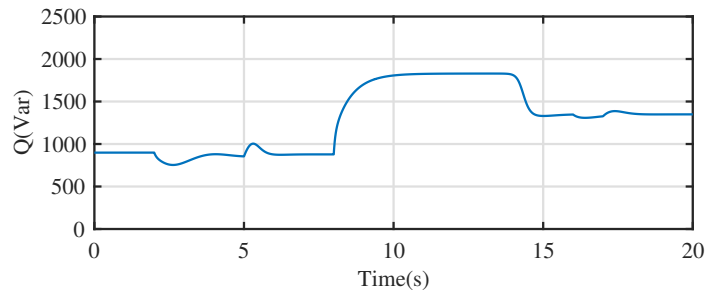
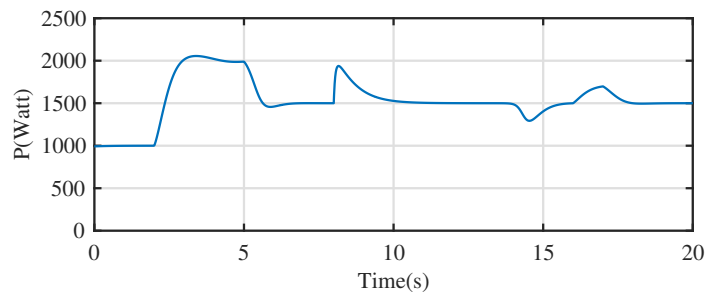


Figure 3.12: Active and reactive power.

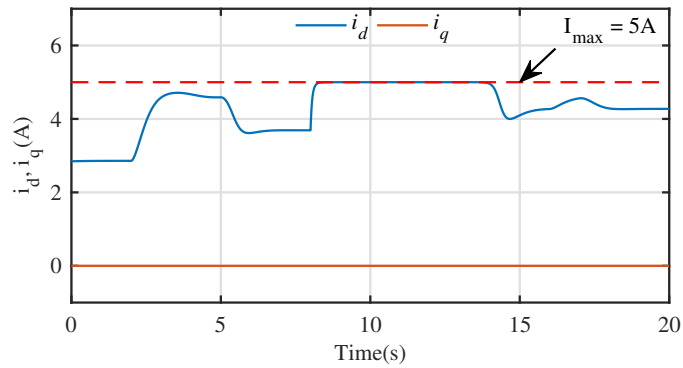


Figure 3.13: d - and q -axis currents.

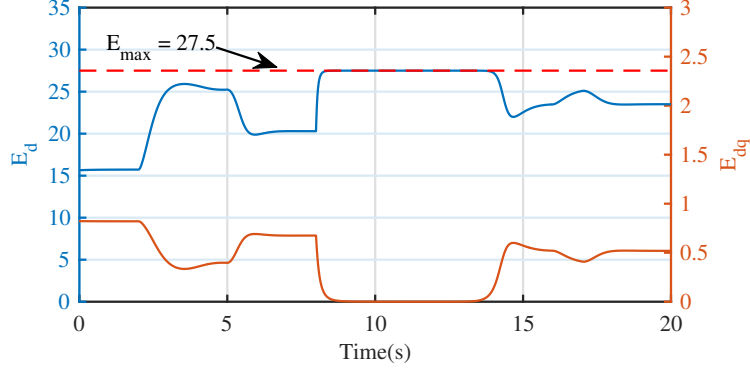


Figure 3.14: Response of the controller states.

system is given in Figure 3.11 where the difference between the rated voltage E^* and V_{rms} can be clearly observed. At $t = 2s$, P_{set} is increased to $2000W$ and at $t = 5s$, it drops to $1500W$. It is clear from the Figure 3.12 that P follows the exact P_{set} values as expected. At the time instant $t = 8s$, the reactive power reference is set to an extreme value which is $2200Var$ to check the effectiveness of the proposed controller. Since the droop mode is enabled, the expected steady-state value for Q can be calculated as $2020Var$. However, it cannot go beyond $1828Var$ as can be seen from Figure 3.12, due to the inherent current-limiting property of the proposed controller. At this point, the current I_d attempts to exceed its maximum value $I_{max} = 5A$, but the controller limits the current to protect the inverter as rigorously proven using ultimate boundedness theory and as seen in Figure 3.13. At $t = 12s$, Q_{set} is decreased to $1500Var$, and after some transient, the reactive power is regulated to $1350Var$ as shown in Figure 3.12. To test the $P \sim -\omega$ droop operation, the grid frequency is decreased by $0.03Hz$ at $t = 16s$ and restored at $t = 17s$. The active power then changes to $1700W$ and is restored back to $1500W$ after $1s$ as shown in Figure 3.12 to compensate the change in the grid frequency.

Since P and Q are coupled due to their expressions (3.40), there are some fluctuations when either of them changes. However, this does not affect the current-limiting property, as shown in Figure 3.13, according to the rigorous mathematical proof. Thus, the capability of the proposed droop controller has been tested for different power reference values, and it has been validated that even under unrealistic power demand, both the closed-loop stability and the current-limiting property are maintained at all times.

In order to confirm the theoretical analysis, the time domain response of the controller states E_d and E_{dq} is given in Figure 3.14. It can be clearly seen that the controller states stay in the defined limits during the entire operation. When the

reactive power demand increases to high values, then E_d and E_{dq} tend to E_{max} and 0, respectively, to ensure that the inverter current I_d remains lower than I_{max} .

3.3 Three-phase inverters with inherent RMS current limitation

In the previous sections, novel nonlinear algorithms using bounded integral controller structure for three-phase grid-connected inverters have been proposed, and simulation studies have been realised. However, analytic conditions to ensure the closed-loop system stability have not been obtained, and experimental studies have not been conducted. Besides, the proposed methods have not been compared with the conventional techniques. In this section, a novel nonlinear droop control method is proposed for three-phase grid-supporting inverters, and analytic conditions for the controller parameter selection are provided to ensure asymptotic stability for the entire closed-loop system for the first time without depending on the particular values of the filter and line parameters. To verify the effectiveness of the proposed controller compared to existing current-limiting control methods, extensive simulation and experimental results of a three-phase inverter are provided under a normal grid and different balanced voltage sag scenarios.

3.3.1 Background and motivations

Grid-supporting inverters are generally controlled via the droop method, whose target is to contribute to the system stability by regulating the grid voltage, and frequency [172, 173]. However, the power measurements required for the droop control operation introduce nonlinearities, which complicate the closed-loop stability analysis of the system [174]. Thus, when analytically examining the closed-loop stability of a droop-controlled inverter, a root locus analysis of the small-signal inverter model is broadly provided [26]. Nevertheless, root locus analysis is valid only for a specific inverter application since it requires particular information on the inverter, filter, and controller parameters.

The stable and reliable operation of a grid-supporting inverter has to be ensured under both normal and faulty grid conditions, especially during transients. If a sudden voltage sag occurs in the grid-side, the current injected by the inverter unit rapidly increases and can reach high values that can cause hardware damages in the inverter device. To accomplish a current-limiting property, either an adjustment of the reference

inverter current is usually applied as mentioned in Chapter 2, or an adjustment of the reference powers (real and reactive) of inverters that follow low-voltage ride-through (LVRT) requirements is often employed. However, even if these techniques ensure the desired current limitation at the steady-state, their transient current-limiting performances are poor [175, 176]. In grid-supporting inverters, the most common approach is the use of saturation units in the output of the inner-loop voltage controller [177, 178]. Nevertheless, this approach is based on the deactivation of the voltage controller during abnormal grid conditions, which can cause integrator windup and system instability [124, 128]. Although a nonlinear current-limiting droop control technique, which does not utilize saturation units, thus avoiding the integrator windup, has been proposed in [162, 163] for single-phase grid-connected inverters and in [171] for three-phase rectifiers, it introduces additional controller states, which makes the hardware implementation a difficult task. Besides, a nonlinear current-limiting controller is proposed in [179] using optimization techniques, but this scheme requires knowledge of the system parameters for the controller implementation and intensive computational effort. As explained in Chapter 2.3, the majority of the current-limiting control techniques for three-phase inverters are designed on the synchronously rotating dq frame and aim to limit the d - and q -axis of the inverter current separately [116, 26, 156]. Then, in order to ensure RMS current limitation, adaptive saturation units are employed, which further complicate the implementation of the controller [180]. Therefore, there is a need for a novel nonlinear control approach for three-phase grid-supporting inverters that inherently limits the RMS inverter current without the need for saturation units, offers a simple controller implementation, and facilitate the closed-loop stability analysis.

Inspired by the recently developed state-limiting PI controller in [181], a nonlinear controller is proposed and formulated to incorporate the widely used droop control concept and provide the necessary ancillary services to the grid. Then, using invariant set theory, it is rigorously proven for the first time that the proposed scheme ensures the desired limitation of the RMS inverter current below a given maximum value during the entire operation, i.e. during transients and at the steady-state, irrespective of the grid conditions that might include grid faults (voltage sags). Opposed to the common droop control techniques, which align the inverter output voltage with the d -axis [26], the novel idea of the proposed approach is based on the alignment of the local inverter current with the d -axis using a suitable formulation of the inverter control input. The special structure of the proposed controller ensures that the desired RMS current limitation is maintained at all times, even during the transient response of a balanced grid voltage sag.

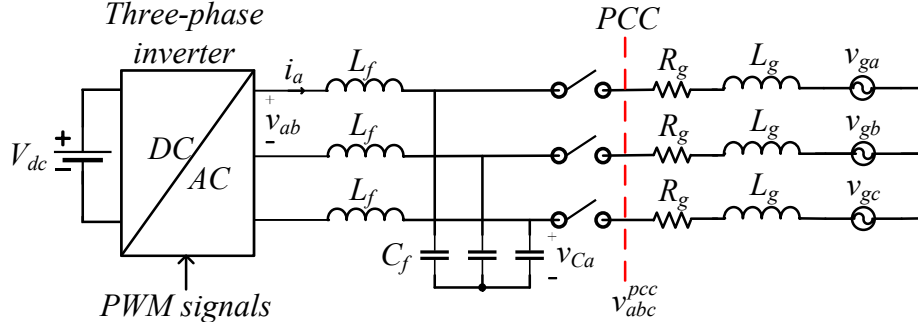


Figure 3.15: Grid-connected three-phase inverter.

Although the proposed method in this section can be regarded as a continuation of the technique proposed in section 3.2 [151], many technical improvements and new contributions are offered, such as i) a new structure of the proposed controller which introduces less dynamic states, thus leading to a simplified implementation, ii) rigorous closed-loop system stability for the entire grid-supporting inverter without depending on the exact values of the inverter and filter parameters, iii) detailed comparison with the conventional current-limiting control methods, and iv) extensive experimental results under a normal grid and under balanced voltage sags, to validate the proposed approach on a real setup. To this end, compared to the existing droop control and current-limiting techniques, the proposed droop control approach for three-phase grid-supporting inverters inherits a desired RMS current limitation at all times, even during transients, without additional saturation units, while guaranteeing a stable closed-loop system. This is accomplished in a unified structure, without the need of modifying the controller during a grid voltage sag, as often required by LVRT methods, causing the RMS current to violate its desired maximum threshold during the transient [175, 176]. Furthermore, since no saturation units are required, contrary to the conventional approaches [124, 128], the proposed method does not suffer from integrator windup, thus simplifying its implementation and facilitating the stability analysis. A detailed comparison with the conventional LVRT and current-limiting methods is presented in this section to highlight the novelty of the proposed control approach, followed by experimental validation.

3.3.2 Dynamic system modeling and problem statement

The system under consideration is a three-phase inverter which is connected to a point of common coupling (PCC) via an LC filter, as shown in Figure 3.15. The filter inductance and capacitance are denoted as L_f , C_f , respectively, while the line resistance

and inductance are expressed as R_g and L_g . Let v_{abc}^{pcc} be the balanced three phase voltages at the PCC, where V_{rms} and θ_g are the PCC RMS voltage and phase angle, respectively. Assuming the global dq frame PCC voltages are given as V_d^{pcc} and V_q^{pcc} , following the axis transformation as given in the previous section [151], the local dq frame PCC voltages are calculated as

$$\begin{bmatrix} V_{dl}^{pcc} \\ V_{ql}^{pcc} \end{bmatrix} = \begin{bmatrix} V_d^{pcc} \cos \delta + V_q^{pcc} \sin \delta \\ -V_d^{pcc} \sin \delta + V_q^{pcc} \cos \delta \end{bmatrix}. \quad (3.58)$$

where $\delta = \theta - \theta_g$ describes the phase angle difference between the inverter and the PCC. Thus, the dynamic equations of the three-phase inverter are given as

$$L_f \frac{di_d}{dt} = V_d + \omega L_f i_q - V_{dl}^{pcc} \quad (3.59)$$

$$L_f \frac{di_q}{dt} = V_q - \omega L_f i_d - V_{ql}^{pcc} \quad (3.60)$$

where i_d, i_q and V_d, V_q denote the dq frame local inverter currents and voltages, while $\omega = \dot{\theta}$ is the inverter angular frequency.

Considering the global PCC voltages V_d^{pcc}, V_q^{pcc} and the local currents, then the inverter active and reactive power can be computed as

$$\begin{aligned} P &= \frac{3}{2} \left[\cos \delta \left(V_d^{pcc} i_d + V_q^{pcc} i_q \right) + \sin \delta \left(V_q^{pcc} i_d - V_d^{pcc} i_q \right) \right] \\ Q &= \frac{3}{2} \left[\cos \delta \left(V_q^{pcc} i_d - V_d^{pcc} i_q \right) - \sin \delta \left(V_d^{pcc} i_d + V_q^{pcc} i_q \right) \right] \end{aligned} \quad (3.61)$$

To achieve the voltage and frequency regulation for grid support when required, the universal droop controller, with droop expressions $P \sim V$ and $Q \sim -\omega$, which can be applied independently of the inverter output impedance [93], will be used in this section. Since the power expressions (3.61) are nonlinear, the closed-loop system introduces nonlinear dynamics, which increase the difficulty in proving stability and ensuring a reliable and safe operation under both normal and faulty grid conditions. To this end, the main objective of this section is to propose a novel control approach for implementing the droop functionality in three-phase grid-supporting inverters that guarantees an RMS current limitation under both a normal grid and under balanced grid voltage sags while rigorously ensuring closed-loop system stability.

3.3.3 Proposed nonlinear controller and RMS current-limiting property

3.3.3.1 Proposed nonlinear controller

In order to ensure that the RMS value of the inverter current remains limited at all times, the proposed novel controller is based on the idea of orienting the inverter current to the local d -axis, i.e. $i_q = 0$, and then implement a bounded dynamic controller that limits the d -axis inverter current to a range of positive values and inherits the desired droop expression. In order to accomplish this task, the inverter voltage, which is the control input, is separated into two parts: *a*) a feed-forward term v_{abc}^{pcc} that contains the PCC voltage in the abc frame and *b*) a feedback control term \bar{v}_{abc} , obtained from a dq/abc transformation that implements the bounded nonlinear controller dynamics.

It should be underlined that the dynamic feedback term \bar{v}_{abc} is disabled when the relay is open, i.e. when the PCC is disconnected and enabled only when the relay is closed; hence the controller includes only the feed-forward term v_{abc}^{pcc} before connection, thus leading to a smooth grid connection and simultaneously avoiding the presence of circulating currents.

Hence, the proposed controller is introduced in the following scheme

$$v_{abc} = v_{abc}^{pcc} + \bar{v}_{abc} \quad (3.62)$$

where the feedback term \bar{v}_{abc} is calculated from a dq/abc transformation using the angular frequency θ obtained considering the $Q \sim -\omega$ droop

$$\dot{\theta} = \omega = \omega^* + m(Q - Q_{set}) \quad (3.63)$$

where ω^* represents the rated grid angular frequency. Q_{set} is the reactive power reference and m indicates the reactive power droop coefficient. Consequently, the dq frame feedback term takes the form

$$\bar{v}_d = -r_v i_d + \frac{r_v I_{rms}^{max}}{\sqrt{2}} (1 + \sin \sigma) - \omega L_f i_q \quad (3.64)$$

$$\bar{v}_q = -r_v i_q + \omega L_f i_d \quad (3.65)$$

where r_v is the constant virtual resistance, σ is the dynamic controller state, $\omega L_f i_d$ and $\omega L_f i_q$ are decoupling terms. In addition, I_{rms}^{max} is the maximum rated inverter RMS current which is defined by the user or the technical limitations of the inverter.

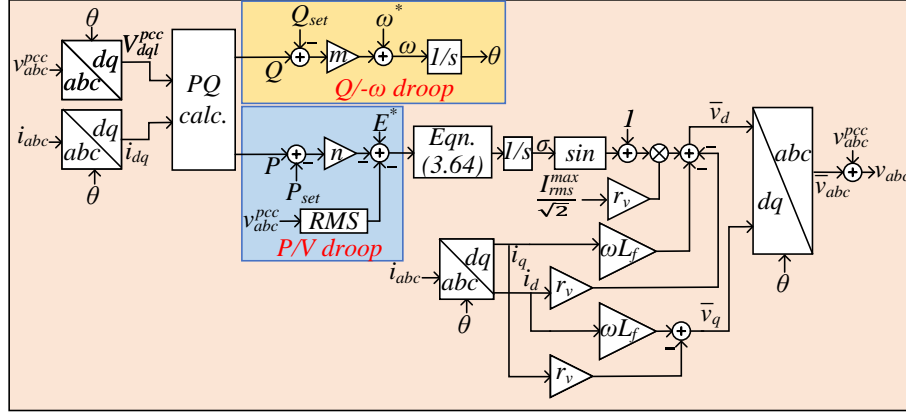


Figure 3.16: Implementation diagram of the proposed controller.

Motivated by the recently proposed nonlinear state-limiting PI controller structure presented in [181], the dynamics for the controller state σ are given as

$$\dot{\sigma} = \frac{\sqrt{2}c}{r_v I_{rms}^{max}} [(E^* - V_{rms}) - n(P - P_{set})] \cos \sigma \quad (3.66)$$

where c is the positive integral gain. By selecting the initial condition of σ to satisfy $\sigma_0 \in [-\frac{\pi}{2}, \frac{\pi}{2}]$, then it is guaranteed that $\sigma(t) \in [-\frac{\pi}{2}, \frac{\pi}{2}], \forall t \geq 0$. As it is explained in [181], the nonlinear dynamics have been carefully designed to avoid a continuously oscillating behavior of the controller state σ and additionally ensure that the controller dynamics slow down, i.e. $\dot{\sigma} \rightarrow 0$, as $\sigma \rightarrow \pm\frac{\pi}{2}$ (near the limits of the state σ), which illustrates an inherent integrator anti-windup property. Hence, the proposed controller does not result in any nonlinear phenomena that can lead to instability for the inverter system. Note that if initially σ_0 is selected as $\sigma_0 = -\frac{\pi}{2} + \epsilon$, for an arbitrarily small $\epsilon > 0$, then at the moment of the connection with the grid, since the inverter currents are very small before the connection, then both \bar{v}_d and \bar{v}_q will be very close to zero from (3.64)-(3.65), and a smooth transient can be achieved.

Since the controller state σ represents an integral action, it leads to the regulation of the function $(E^* - V_{rms}) - n(P - P_{set})$, which describes the $P \sim V$ droop control that should be regulated to zero at the steady-state. In this droop function, E^* indicates the nominal RMS grid voltage, V_{rms} represents the RMS PCC voltage, which can be computed as $V_{rms} = \sqrt{\frac{(V_d^{pcc})^2 + (V_q^{pcc})^2}{2}}$, while P_{set} and n stand for the active power reference value and the active power droop coefficient, respectively. Note that by removing the term $(E^* - V_{rms})$ in (3.66), the controller can easily switch its operation from droop control to real power regulation. In order to illustrate the implementation of the proposed controller, a detailed diagram of its structure is provided in Figure

3.16.

3.3.3.2 RMS current-limiting property

By implementing the controller dynamics (3.64) and (3.65) into the original inverter dynamics (3.59) and (3.60), the closed-loop inverter current equations can be written as

$$L_f \frac{di_d}{dt} = -r_v i_d + \frac{r_v I_{rms}^{max}}{\sqrt{2}} (1 + \sin \sigma) \quad (3.67)$$

$$L_f \frac{di_q}{dt} = -r_v i_q \quad (3.68)$$

By defining $i_s = i_d - \frac{I_{rms}^{max}}{\sqrt{2}}$, then the equation (3.67) becomes

$$L_f \frac{di_s}{dt} = -r_v i_s + \frac{r_v I_{rms}^{max}}{\sqrt{2}} \sin \sigma \quad (3.69)$$

where i_s is the shifted d -axis current, which is defined to ensure the positiveness of the d -axis current. This is necessary to ensure the closed-loop asymptotic stability, as it will be explained in the next part. As it is clear from (3.68), the q -axis current dynamics are independent providing the solution $(i_q(t) = i_q(0)e^{-\frac{r_v}{L_f}t})$, and therefore if initially $i_q(0) = 0$, then $i_q(t) = 0, \forall t \geq 0$. Thus, it is sufficient to prove that only the d -axis current will be limited below a given maximum value for guaranteeing the RMS current-limiting property at all times. Then, for system (3.69), the following continuously differentiable function can be considered:

$$V = \frac{1}{2} L_f i_s^2, \quad (3.70)$$

while its time derivative can be computed by utilizing (3.69) as

$$\begin{aligned} \dot{V} &= -r_v i_s^2 + \frac{r_v I_{rms}^{max}}{\sqrt{2}} i_s \sin \sigma \\ &\leq -r_v i_s^2 + \frac{r_v I_{rms}^{max}}{\sqrt{2}} |i_s| \\ &\leq -r_v |i_s| \left(|i_s| - \frac{I_{rms}^{max}}{\sqrt{2}} \right). \end{aligned} \quad (3.71)$$

Hence, it becomes obvious from (3.71) that

$$\dot{V} < 0, \forall |i_s| > \frac{I_{rms}^{max}}{\sqrt{2}} \quad (3.72)$$

This means that the set $S = \{i_s \in R : |i_s| \leq \frac{I_{rms}^{max}}{\sqrt{2}}\}$ is invariant (since $\dot{V} < 0$ outside of S) [164, 182]. Hence, if initially $|i_s(0)| \leq \frac{I_{rms}^{max}}{\sqrt{2}}$, then

$$|i_s(t)| \leq \frac{I_{rms}^{max}}{\sqrt{2}}, \forall t \geq 0. \quad (3.73)$$

Since $i_s = i_d - \frac{I_{rms}^{max}}{\sqrt{2}}$, then (3.73) can be rewritten as

$$-\frac{I_{rms}^{max}}{\sqrt{2}} \leq i_d - \frac{I_{rms}^{max}}{\sqrt{2}} \leq \frac{I_{rms}^{max}}{\sqrt{2}}, \forall t \geq 0, \quad (3.74)$$

or equivalently

$$0 \leq i_d \leq \sqrt{2}I_{rms}^{max}, \forall t \geq 0. \quad (3.75)$$

Note, however, that by projecting the inverter current vector with amplitude $\sqrt{2}I_{rms}$, on the d and q axes, there is

$$\sqrt{i_d^2 + i_q^2} = \sqrt{2}I_{rms}. \quad (3.76)$$

Since $i_q = 0$, then $i_d = \sqrt{2}I_{rms}$ and consequently from (3.75), it is proven that

$$I_{rms} \leq I_{rms}^{max} \quad \forall t \geq 0, \quad (3.77)$$

which results in the desired RMS current-limiting property.

As can be understood from the analysis provided above, the current-limiting property is proven independently of the grid variables such as voltage, frequency, and angle, the droop functions, and the nonlinearities in the power expressions (3.61). Hence, this mathematical proof ensures a safe inverter operation under grid variations/faults or under unrealistic P_{set} values. In addition, contrary to [179], the proposed controller ensures that the system current will be limited at both transients and steady-state, and in contrast to [124], the integrator windup problem is inherently addressed using the state-limiting PI controller dynamics ($\dot{\sigma} \rightarrow 0$ when $\sigma \rightarrow \pm \frac{\pi}{2}$, or equivalently when $I_{rms} \rightarrow I_{rms}^{max}$) without the need for saturation blocks which might lead to system instability.

3.3.4 Closed-loop stability analysis

In the previous part, it was proven that the RMS inverter current remains bounded below a given value regardless of the grid parameters or the active and reactive power set values. However, closed-loop system stability, in the sense of convergence to a desired equilibrium point, has not been guaranteed yet. Therefore, this section focuses on proving the asymptotic stability of the complete system. Taking into account that the power angle is given as $\delta = \theta - \theta_g$, then from (3.63) it yields

$$\dot{\delta} = \omega^* - \omega_g + m(Q - Q_{set}), \quad (3.78)$$

where ω_g is the PCC angular frequency. The closed-loop system dynamics are given now from (3.66)-(3.68) and (3.78). Without loss of generality, as done in [116], one can consider that $V_d^{pcc} = \sqrt{2}V_{rms}$ and $V_q^{pcc} = 0$ are constant (or equivalently close to the grid voltages at the global reference frame), and since it was proven in the previous section that the local q -axis current of the inverter i_q remains at zero at all times, then the power expressions (3.61) can be simplified as

$$\begin{aligned} P &= \frac{3}{\sqrt{2}}V_{rms}i_d \cos \delta \\ Q &= -\frac{3}{\sqrt{2}}V_{rms}i_d \sin \delta. \end{aligned} \quad (3.79)$$

Considering (3.66)-(3.68), and (3.78), the closed-loop state vector becomes $x = [i_d \ \sigma \ \delta \ i_q]^T$. Let V_{rms} and ω_g take some constant (or piece-wise constant) values, not necessarily equal to their rated ones. Then, the equilibrium point vector $x_e = [i_{de} \ \sigma_e \ \delta_e \ i_{qe}]^T$ can be calculated as

$$a) \ i_{de} = \frac{I_{rms}^{max}}{\sqrt{2}}(1 + \sin \sigma_e) \quad (3.80)$$

$$b) \ \sigma_e = \sin^{-1} \left(\frac{2}{3V_{rms} \cos \delta_e I_{rms}^{max}} \left(\frac{E^* - V_{rms}}{n} + P_{set} \right) - 1 \right) \quad (3.81)$$

$$c) \ \delta_e = \tan^{-1} \left(\frac{-\left(\frac{\omega_g - \omega^*}{m} + Q_{set}\right)}{\left(\frac{E^* - V_{rms}}{n} + P_{set}\right)} \right) \quad (3.82)$$

$$d) \ i_{qe} = 0 \quad (3.83)$$

where P_{set} and Q_{set} are active and reactive power set values, which can be changed by the control operator.

Now, the closed-loop system stability can be summarised in the following propo-

sition.

Proposition 1. Every equilibrium point $x_e = [i_{de} \ \sigma_e \ \delta_e \ i_{qe}]^T$ of the closed-loop system (3.66)-(3.68), and (3.78), given by (3.80)-(3.83), with $\sigma_e, \delta_e \in (-\frac{\pi}{2}, \frac{\pi}{2})$, is asymptotically stable when r_v is chosen as

$$r_v > 3mL_f V_{rms} I_{rms}^{max}, \quad (3.84)$$

and P_{set} and Q_{set} are selected to satisfy the inequality

$$\left| \frac{\omega^* - \omega_g}{m} - Q_{set} \right| \leq \left| \frac{E^* - V_{rms}}{n} + P_{set} \right|. \quad (3.85)$$

Proof: Given the equilibrium point $x_e = [i_{de} \ \sigma_e \ \delta_e \ i_{qe}]^T$, the Jacobian matrix of the closed-loop system takes the form,

$$J = \begin{bmatrix} J_T & 0_{3 \times 1} \\ 0_{1 \times 3} & -\frac{r_v}{L_f} \end{bmatrix}, \quad (3.86)$$

where

$$J_T = \begin{bmatrix} -\frac{r_v}{L_f} & \frac{r_v I_{rms}^{max} \cos \sigma_e}{\sqrt{2} L_f} & 0 \\ -3 \frac{V_{rms} cn \cos \sigma_e \cos \delta_e}{r_v I_{rms}^{max}} & 0 & 3 \frac{V_{rms} cn i_{de} \cos \sigma_e \sin \delta_e}{r_v I_{rms}^{max}} \\ -\frac{3}{\sqrt{2}} m V_{rms} \sin \delta_e & 0 & -\frac{3}{\sqrt{2}} m V_{rms} i_{de} \cos \delta_e \end{bmatrix}. \quad (3.87)$$

Due to the block diagonal structure of matrix J in (3.86) and since $-\frac{r_v}{L_f}$ is negative, for the stability of the closed-loop system, it is only required to investigate the eigenvalues of J_T in (3.87). The characteristic equation of (3.87) can be formed as

$$\begin{aligned} & \lambda^3 + \left(\frac{3}{\sqrt{2}} m V_{rms} i_{de} \cos \delta_e + \frac{r_v}{L_f} \right) \lambda^2 \\ & + \left(\frac{3}{\sqrt{2} L_f} V_{rms} \cos \delta_e (r_v m i_{de} + cn \cos^2 \sigma_e) \right) \lambda \\ & + \frac{9}{2 L_f} cn m i_{de} \cos^2 \sigma_e V_{rms}^2 = 0 \end{aligned} \quad (3.88)$$

By applying the Routh-Hurwitz criterion, in order for all eigenvalues to have negative real parts, the following three stability conditions are obtained:

$$\left(\frac{3}{\sqrt{2}} m V_{rms} i_{de} \cos \delta_e + \frac{r_v}{L_f} \right) > 0 \quad (3.89)$$

$$\frac{9}{2L_f} c n m i_{de} \cos^2 \sigma_e V_{rms}^2 > 0 \quad (3.90)$$

$$\frac{3}{\sqrt{2} L_f} V_{rms} \cos \delta_e (r_v m i_{de} + c n \cos^2 \sigma_e) > \frac{\frac{9}{2L_f} c n m i_{de} \cos^2 \sigma_e V_{rms}^2}{\left(\frac{3}{\sqrt{2}} m V_{rms} i_{de} \cos \delta_e + \frac{r_v}{L_f} \right)}. \quad (3.91)$$

Since $\sigma_e \in (-\frac{\pi}{2}, \frac{\pi}{2})$, then from (3.80) there is $i_{de} > 0$, while from the current-limiting proof in the previous subsection, $i_{de} \leq \sqrt{2} I_{rms}^{max}$, i.e. $i_{de} \in (0, \sqrt{2} I_{rms}^{max}]$. As a result, condition (3.90) always holds. Note also that from (3.79) there is:

$$|P_e| = \left| \frac{3}{\sqrt{2}} V_{rms} i_{de} \cos \delta_e \right| \leq 3 V_{rms} I_{rms}^{max}. \quad (3.92)$$

Given the selection of r_v according to (3.84) and taking into account (3.92), one can easily see that condition (3.89) is also satisfied.

Finally, condition (3.91) can be rewritten as

$$\begin{aligned} & \frac{3}{\sqrt{2} L_f} V_{rms} \cos \delta_e (r_v m i_{de} + c n \cos^2 \sigma_e) \left(\frac{3}{\sqrt{2}} m i_{de} V_{rms} \cos \delta_e + \frac{r_v}{L_f} \right) \\ & - \frac{9}{2L_f} c n m i_{de} \cos^2 \sigma_e V_{rms}^2 > 0. \end{aligned} \quad (3.93)$$

By using the trigonometric property $\cos^2 \delta_e = 1 - \sin^2 \delta_e$, after some calculations, (3.93) results in

$$\begin{aligned} & \frac{9}{2L_f} V_{rms}^2 m^2 i_{de}^2 r_v + \frac{3}{\sqrt{2} L_f} V_{rms} (r_v m i_{de} + c n \cos^2 \sigma_e) \cdot \\ & \frac{r_v \cos \delta_e}{L_f} - \frac{3m}{\sqrt{2}} V_{rms} i_{de} \sin^2 \delta_e > 0. \end{aligned} \quad (3.94)$$

In order for the above inequality to hold, it is sufficient to show that

$$\left(\frac{r_v \cos \delta_e}{L_f} - \frac{3m}{\sqrt{2}} V_{rms} i_{de} \sin^2 \delta_e \right) \geq 0, \quad (3.95)$$

Table 3.3: System hardware and control parameters for experimental studies

Parameters	Values	Parameters	Values
L_f	$5.7mH$	L_g	$4.4mH$
R_g	0.5Ω	C_f	$1\mu F$
ω^*	$2\pi 50 rad/s$	I_{rms}^{max}	$2A$
n	0.0117	m	0.0033
S	$660VA$	V_{dc}	$350V$
E^*	$110V$	f_{sw}	$16kHz$
r_v	20Ω	c	50

Now, by combining (3.84) and (3.92), it is guaranteed that

$$\frac{r_v}{L_f} > \frac{3}{\sqrt{2}} m V_{rms} i_{de} \cos \delta_e. \quad (3.96)$$

Taking into account that $\delta_e \in (-\frac{\pi}{2}, \frac{\pi}{2})$, i.e., $0 < \cos \delta_e \leq 1$, the following relation can be obtained

$$\frac{r_v}{L_f} \cos \delta_e > \frac{3}{\sqrt{2}} m V_{rms} i_{de} \cos^2 \delta_e. \quad (3.97)$$

By combining (3.95) and (3.97), then to complete the stability analysis, it is sufficient to show that

$$\frac{3}{\sqrt{2}} m V_{rms} i_{de} (\cos^2 \delta_e - \sin^2 \delta_e) \geq 0. \quad (3.98)$$

Given that P_{set} and Q_{set} are selected according to (3.85), then from (3.82) it holds true that $-1 \leq \tan \delta_e \leq 1$ which yields that $\delta_e \in [-\frac{\pi}{4}, \frac{\pi}{4}]$ or $\delta_e \in [\frac{3\pi}{4}, \frac{5\pi}{4}]$. Hence, it holds true that

$$\cos^2 \delta_e - \sin^2 \delta_e \geq 0, \quad (3.99)$$

which ensures that (3.98) is always satisfied. This completes the proof. \blacksquare

Remark: Proposition 1 provides a useful guidance for the selection of the controller parameter r_v . Note that if V_{rms} and L_f are not accurately known but vary within some given ranges, i.e. $V_{rms} \in [V_{rms}^{min}, V_{rms}^{max}]$ and $L_f \in [L_f^{min}, L_f^{max}]$, then r_v can be selected as

$$r_v > 3mL_f^{max}V_{rms}^{max}I_{rms}^{max}, \quad (3.100)$$

which still satisfies (3.84). Similarly, the range for the values of P_{set} and Q_{set} can be calculated from (3.85), given that V_{rms} and ω_g can vary within some given ranges $V_{rms} \in [V_{rms}^{min}, V_{rms}^{max}]$ and $\omega_g \in [\omega_g^{min}, \omega_g^{max}]$.

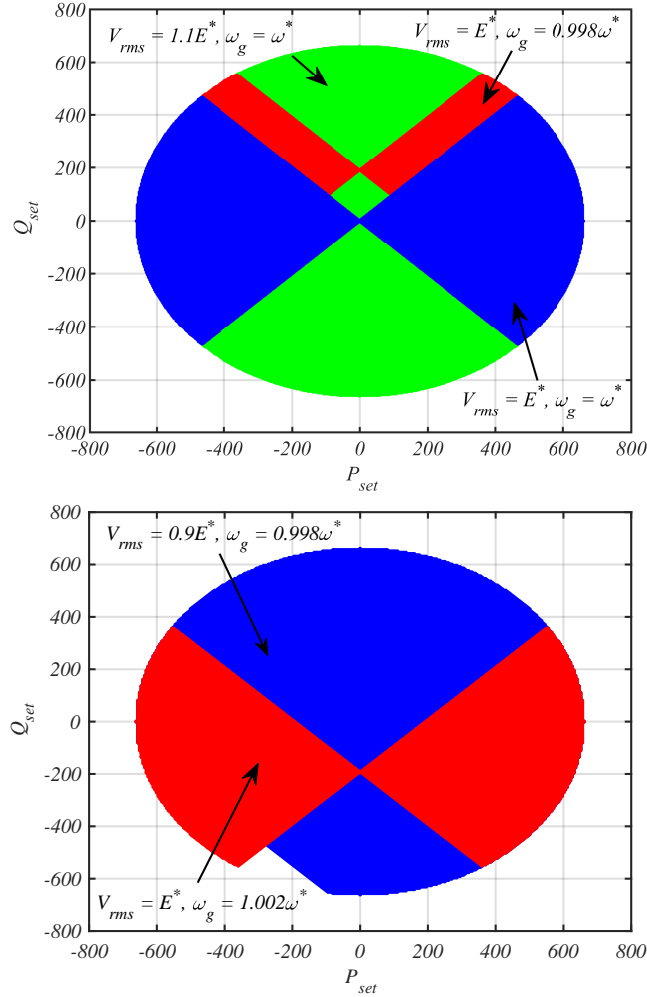


Figure 3.17: Regions for selecting P_{set}^* and Q_{set} to ensure closed-loop stability.

Figure 3.17 provides a guidance on how to select the values of P_{set} and Q_{set} for different values of V_{rms} and ω_g to ensure the closed-loop system stability, using the parameters given in Table 3.3 as an example. In particular, in the upper part of Figure 3.17, it can be observed that with $V_{rms} = 1.1E^*$ and $\omega_g = \omega^*$, the P_{set} and Q_{set} values can be selected anywhere within the green area, while for other voltage and frequency values, the P_{set} and Q_{set} values are restricted to the red or blue area. Similarly, in the lower part of Figure 3.17, the P_{set} and Q_{set} values can be selected within the blue and red areas, according to the different values of V_{rms} and ω_g . Note that these areas represent the sufficient conditions to ensure the closed-loop system stability, i.e. the system may still be stable even if P_{set} and Q_{set} are selected outside of the provided ranges. However, these sets provide a useful guidance to the control operator to ensure that the system stability is guaranteed at all times, based on the proof of Proposition 1.

It should be underlined that Proposition 1 guarantees the closed-loop system stability for the inverter currents and the controller dynamics. In order to prove the closed-loop stability for the entire grid-connected inverter system, the dynamics of the remaining system, which include the capacitor voltages and grid side currents, should be investigated as well. These are given in the global dq frame as

$$C_f \frac{dV_{Cd}}{dt} = i_d \cos \delta - i_q \sin \delta + \omega_g C_f V_{Cq} - i_{gd} \quad (3.101)$$

$$C_f \frac{dV_{Cq}}{dt} = i_d \sin \delta + i_q \cos \delta - \omega_g C_f V_{Cd} - i_{gq} \quad (3.102)$$

$$L_g \frac{di_{gd}}{dt} = -R_g i_{gd} + \omega_g L_g i_{gq} + V_{Cd} - V_{gd} \quad (3.103)$$

$$L_g \frac{di_{gq}}{dt} = -R_g i_{gq} - \omega_g L_g i_{gd} + V_{Cq} - V_{gq} \quad (3.104)$$

where ω_g is the grid frequency and V_{dg} , V_{gq} are the dq -axis components of the grid voltage, which can be considered constant as in [116], to define the equilibrium point in (3.80)-(3.83). This system can be viewed as a linear-time invariant system and can be written in the standard form $\dot{x} = Ax + Bu$ with state vector $x = [V_{Cd} \ V_{Cq} \ i_{gd} \ i_{gq}]^T$ and input vector $u = [i_d \cos \delta \ i_d \sin \delta \ i_q \cos \delta \ i_q \sin \delta \ V_{gd} \ V_{gq}]^T$. Then, the A and B matrices can be constructed as

$$A = \begin{bmatrix} 0 & \omega_g & -\frac{1}{C_f} & 0 \\ -\omega_g & 0 & 0 & -\frac{1}{C_f} \\ \frac{1}{L_g} & 0 & -\frac{R_g}{L_g} & \omega_g \\ 0 & \frac{1}{L_g} & -\omega_g & -\frac{R_g}{L_g} \end{bmatrix}$$

$$B = \begin{bmatrix} \frac{1}{C_f} & 0 & 0 & -\frac{1}{C_f} & 0 & 0 \\ 0 & \frac{1}{C_f} & \frac{1}{C_f} & 0 & 0 & 0 \\ 0 & 0 & 0 & 0 & -\frac{1}{L_g} & 0 \\ 0 & 0 & 0 & 0 & 0 & -\frac{1}{L_g} \end{bmatrix}.$$

One can easily see that matrix A is Hurwitz independently of the filter, line and grid frequency parameters. Hence, system (3.101)-(3.104) is bounded-input bounded-state (BIBS) stable. Since the inverter currents (i_d, i_q) are proven to be bounded in the previous subsection and the grid side voltages (V_{gd}, V_{gq}) are also bounded (constant or piecewise constant), then both the capacitor voltages V_{Cd}, V_{Cq} and the grid currents i_{gd}, i_{gq} are guaranteed to remain bounded at all times.

To complete the stability analysis of the entire closed-loop system, it should be

proven that x converges to $x_e = [V_{Cde} V_{Cqe} i_{gde} i_{gqe}]^T$, which corresponds to $i_d = i_{de}$, $i_q = i_{qe}$ from (3.80)-(3.83) and constant V_{gd} and V_{gq} (not necessarily equal to their rated values). By setting $\tilde{x}_1 = x_1 - x_{1e} = [i_d \ \sigma \ \delta \ i_q]^T - [i_{de} \ \sigma_e \ \delta_e \ i_{qe}]^T$ and $\tilde{x}_2 = x_2 - x_{2e} = [V_{Cd} V_{Cq} i_{gd} i_{gq}]^T - [V_{Cde} V_{Cqe} i_{gde} i_{gqe}]^T$, then the entire closed-loop system given from (3.66)-(3.68), (3.78), (3.101)-(3.104) can be written in the form of two interconnected systems as

$$\dot{\tilde{x}}_1 = f(\tilde{x}_1) \quad (3.105)$$

$$\dot{\tilde{x}}_2 = g(\tilde{x}_1, \tilde{x}_2). \quad (3.106)$$

Based on Proposition 1, system (3.66)-(3.68), (3.78) is asymptotically stable at $[i_{de} \ \sigma_e \ \delta_e \ i_{qe}]^T$, then equivalently (3.105) is asymptotically stable at the origin. In the same framework, since the linear system (3.101)-(3.104) is BIBS with respect to the input u , and V_{gd} , V_{gq} are constant, then consequently (3.106) is BIBS with respect to \tilde{x}_1 . Then, according to Lemma 5.6 in [164], it is proven that the interconnected system (3.105)-(3.106) is also asymptotically stable at the origin, yielding that the remaining system states $[V_{Cd} V_{Cq} i_{gd} i_{gq}]^T$ asymptotically converge to $[V_{Cde} V_{Cqe} i_{gde} i_{gqe}]^T$. This completes the stability analysis of the entire closed-loop system.

Table 3.4: Three-phase inverter system and controller parameters for comparison studies

Parameters	Values	Parameters	Values
Power System Parameters			
L_f	2.2mH	L_g	0.028mH
R_f	0.5Ω	R_g	0.04Ω
ω^*	2π50 rad/s	I_{rms}^{max}	20A
S	13200VA	V_{dc}	800V
E^*	220V	C_f	1μF
Proposed Controller Parameters			
n	0.0017	m	0.0012
r_v	20Ω	c	3000
Saturation and LVRT Controller Parameters			
k_{pi}, k_{ii}	4, 200	k_{pv}, k_{iv}	0.03, 1.2
n	0.0047	m	0.0012
r_v	0.7Ω	k_{pfrt}, k_{ifrt}	0.04, 2.5

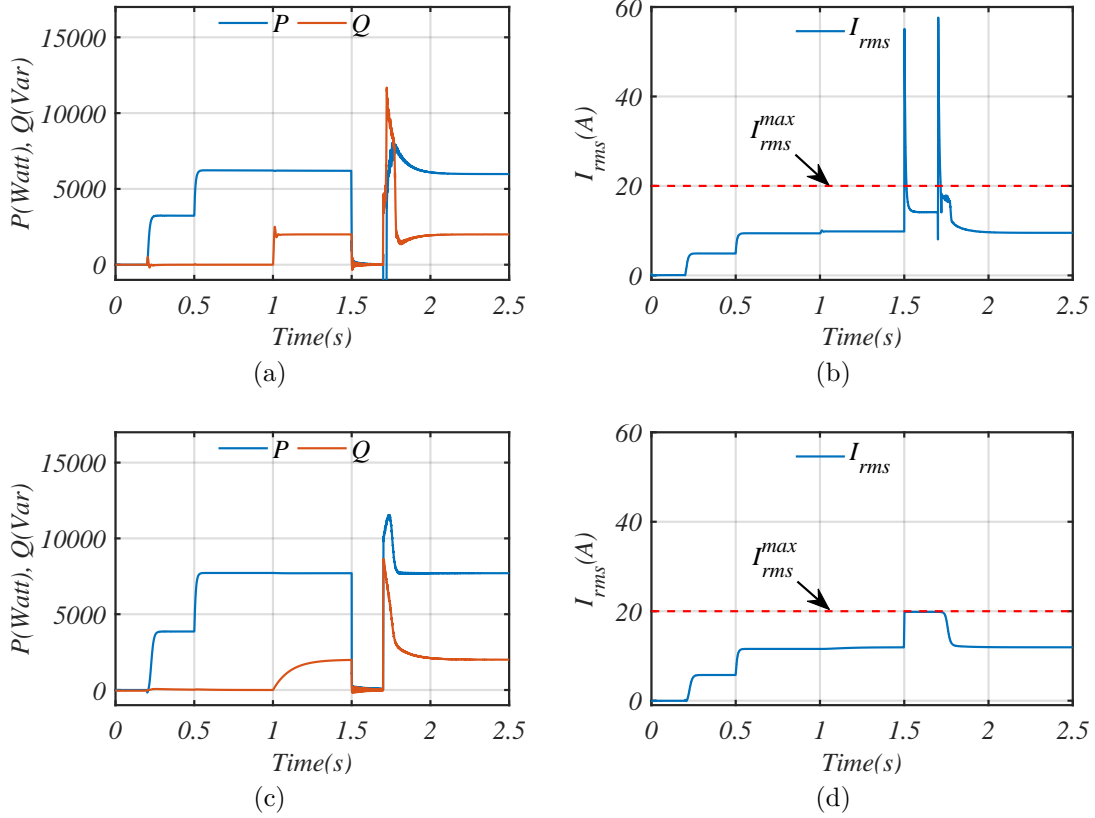


Figure 3.18: Performance comparison between the Benchmark Ctrl 1 (a)-(b) and the Proposed controller (c)-(d) under a three-phase short-circuit fault.

3.3.5 Performance comparison with the existing methods

In order to evaluate the proposed controller performance and highlight the novel contributions compared to the other recently proposed methods, in this section, comparative simulation results are presented using the Matlab/Simulink environment. In particular, the proposed control scheme is compared with the two widely used current-limiting methods for inverter-interfaced DERs. Both benchmark schemes are based on the cascaded droop control scheme presented in [26], while adopting the $P \sim V$ and $Q \sim -\omega$ droop relations proposed in [176] to have a direct comparison. The simulation parameters are shown in Table 3.4. Regarding the conventional current-limiting methods, the first benchmark scheme (Benchmark Ctrl 1) uses saturation units at the output of the voltage PI controllers, as explained in [124], while the second method (Benchmark Ctrl 2) follows an LVRT technique to limit the injected power (thus limiting the inverter current as well) by modifying the active and reactive power references using a specific formula in case of grid fault, as explained in [175, 176] in detail. Since Benchmark Ctrl 1 and Benchmark Ctrl 2 are the most commonly used current-limiting techniques in

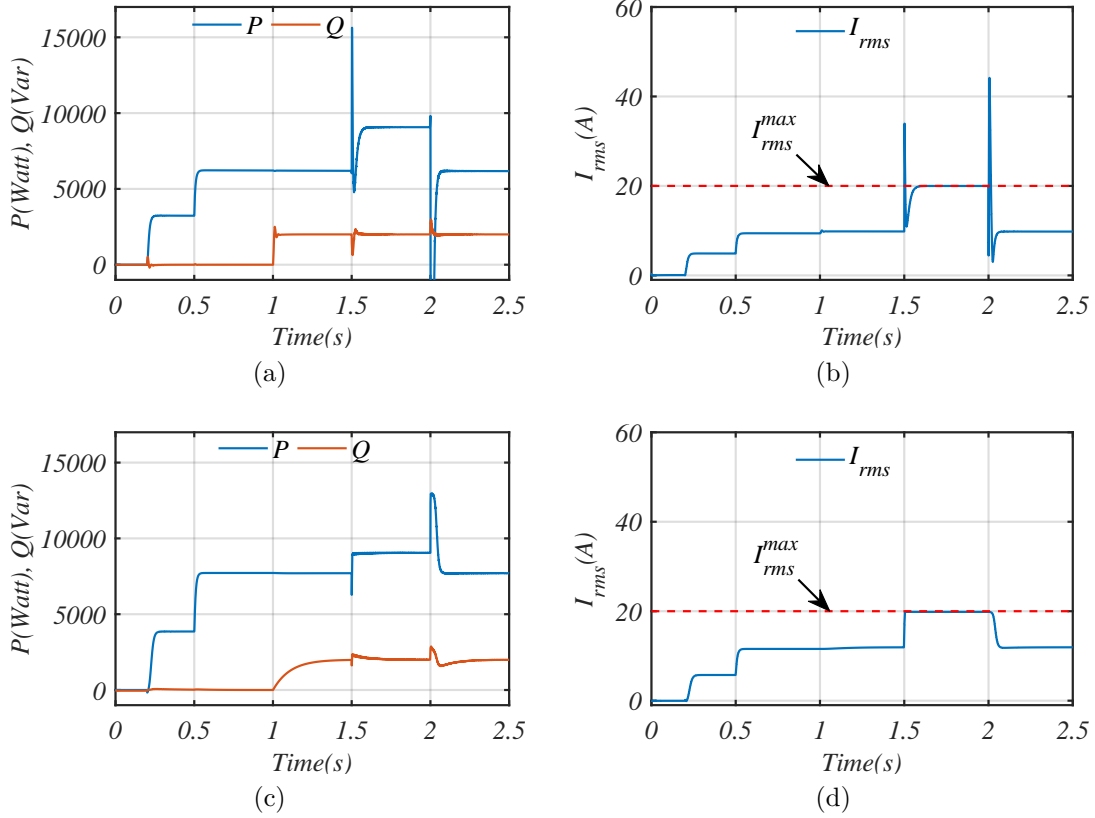


Figure 3.19: Performance comparison between the Benchmark Ctrl 2 (a)-(b) and the Proposed controller (c)-(d) under a 30% balanced grid voltage sag.

grid-connected inverter applications, comparison studies have been realised based on them. Initially, the proposed controller is compared with the Benchmark Ctrl 1, with the performed scenario being as follows: At the beginning, the inverter is not connected to the grid, since the relay is open. At $t = 0.2$ s, the relay closes and the inverter is connected to the grid, with P_{set} and Q_{set} having initially the values of 4000 W and 0 Var, while they are changed to 8000 W and 2000 Var at $t = 0.5$ s and $t = 1$ s, respectively. As it is depicted in Figure 3.18a and Figure 3.18c, both the Benchmark Ctrl 1 and the proposed controller regulate their output powers to the desired values according to droop control. From the same figure, it can be understood that the operation of the inverter under the two control schemes is similar under normal grid conditions. However, at $t = 1.5$ s, a bolted short-circuit occurs at the grid voltage and last for 0.2 s. When this fault happens, as can be seen in Figure 3.18b, the Benchmark Ctrl 1 fails to limit the inverter current during the fault appearance and clearance transients, while during the steady state, the maximum available power is not utilised, since the d - and q -axis inverter currents are limited independently to ensure the worst case, i.e., $I_{rms} \leq I_{rms}^{max}$. In contrast, the proposed controller effectively limits the inverter current

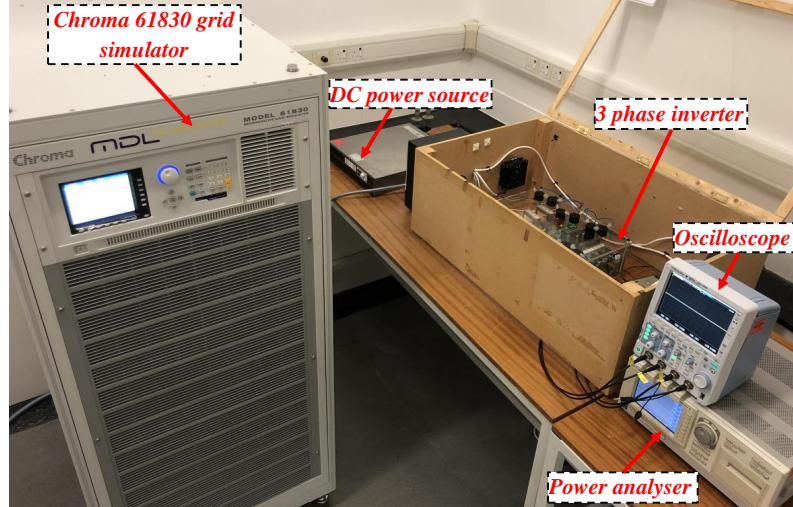


Figure 3.20: Experimental setup.

during both the transient and the steady-state as shown in Figure 3.18d, while the inverter current is maximized during the fault to provide maximum voltage support.

Next, the proposed controller is compared with the Benchmark Ctrl 2. While the normal grid operation is the same with the previous comparison as shown in Figure 3.19a and Figure 3.19c, here a balanced 30% voltage drop is applied at the grid voltage at $t = 1.5s$ and lasts for 0.5s. It is highlighted in Figure 3.19b that even if the LVRT limitation technique of the Benchmark Ctrl 2 manages to provide maximum voltage support during the fault, the maximum inverter current threshold is again violated during the fault appearance and clearance transients. On the other hand, using the proposed controller in the same faulty conditions, the current is safely regulated to its maximum value as shown in Figure 3.19d. Hence, as it is verified in the presented simulation study, the proposed controller outperforms the benchmark control schemes, in terms of its transient current-limiting property as shown in both Figure 3.18 and Figure 3.19, and the maximization of the injected power opposed to Benchmark Ctrl1 (Figure 3.18b) as illustrated in Figure 3.18 during the balanced grid faults. It is important to note that the reference regulation speed of the proposed controller can be enhanced by increasing the integral gain c . The higher values of c will not affect the current-limiting property as it is proven via nonlinear analysis in the previous part.

3.3.6 Experiment results

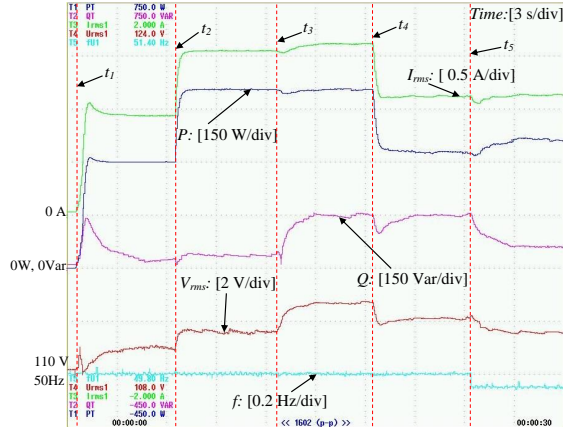
In order to further validate the effectiveness of the proposed controller, a 660 VA three-phase grid-connected inverter was experimentally tested. The inverter was connected

to a Chroma 61830 grid simulator via an LC filter and a line, as shown in Figure 3.20. The controller was implemented as in Figure 3.16 using a dSPACE 1104 control card with a sampling frequency of 15 kHz, while the system and controller parameters are given in Table 3.3. The droop coefficients were chosen as in [93, 162].

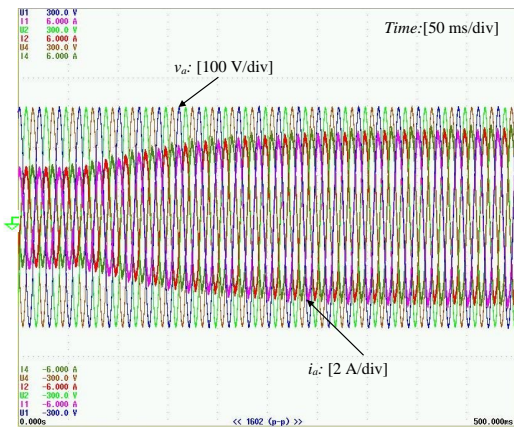
3.3.6.1 Normal grid operation

Initially, normal grid conditions are considered and in Figure 3.21a, the following scenario is performed. At $t_1 = 0.6s$, the inverter is connected to the grid, with the real power regulation mode is initially enabled and the real and reactive power reference values being 300 W and 0 Var, respectively. At $t_2 = 6.6s$, the real power reference value is increased to 500 W and at $t_3 = 12.6s$, the reactive power reference is changed to 150 Var. As it can be seen in Figure 3.21a, the proposed controller quickly regulates P and Q to their desired reference values. Note that small inaccuracies are present at the reactive power measurement near the zero value due to limitations of the power analyser in low values (near zero). To verify the droop control operation, the active power droop is enabled at $t_4 = 18.4s$ and P is quickly regulated at its new steady-state value, which can be calculated as $\frac{E^* - V_{rms}}{n} + P_{set}$ from (3.66), to regulate the inverter output voltage closer to its rated value. Likewise, to verify the reactive power droop control operation, a drop from 50 Hz to 49.95 Hz is applied to the grid frequency using the grid simulator, at $t_5 = 24.3s$. Thus, the reactive power drops in accordance to the frequency difference with respect to its nominal value.

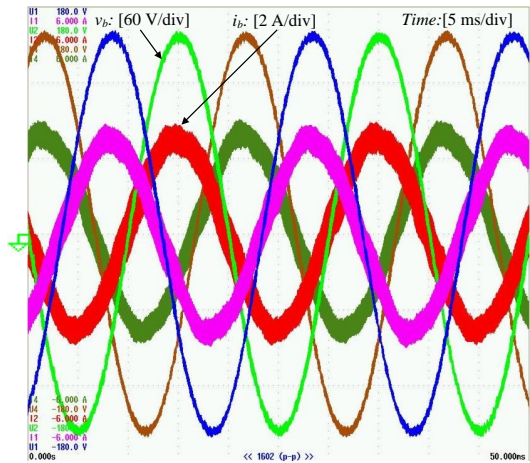
In order to validate the current-limiting property of the proposed controller, at $t = 75ms$ in Figure 3.21b, the active power reference is increased from 300 W to 750 W with reactive power reference value being 0 Var, which represents a demand higher than the maximum apparent power of the inverter. However, as shown in Figure 3.21b and proven in the theoretic part, I_{rms} is limited to 1.84 A, thus limiting the real power to 607.2 W, which is slightly below the maximum inverter apparent power. It is underlined that the RMS inverter current is limited to a slightly lower value than I_{rms}^{max} because in the theoretic design of the controller, the parasitic resistance of the filter inductor was neglected. In fact, if the filter inductor L_f introduces a small series resistance r_f , then from the resulting closed-loop inverter current dynamics at the steady-state, given similarly to (3.67), one can calculate the maximum steady-state RMS value of the current as $I_{rmse}^{max} = \frac{r_v}{r_f + r_v} I_{rms}^{max}$. In order to fully utilise the inverter current-limiting capability, the virtual resistor r_v can be selected to dominate the parasitic resistance



(a) Time response of P , Q , I_{rms} , V_{rms} and f



(b) Current transient when P_{set} is increased from 300 W to 750 W



(c) Steady-state inverter voltages and currents

Figure 3.21: Grid-supporting inverter operation under the proposed controller during normal grid conditions.

r_f (i.e. $r_v \gg r_f$) or the d -axis dynamic feedback term (3.64) can be modified as

$$\bar{v}_d = -r_v i_d + \frac{(r_f + r_v) I_{rms}^{max}}{\sqrt{2}} (1 + \sin \sigma) - \omega L_f i_q \quad (3.107)$$

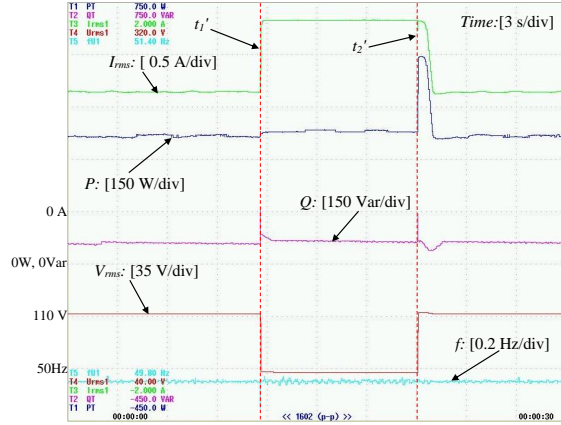
Note that this modification does not affect the theoretical proof provided above and $I_{rms} < I_{rms}^{max}$ will still hold, which is required for the safe inverter operation. However, even with the proposed control design, which does not require knowledge of this parasitic resistance, the RMS current is limited below the maximum value as desired, offering a more robust controller implementation.

Furthermore, Figure 3.21c shows the steady-state inverter current and voltage measurements when I_{rms} has reached to I_{rms}^{max} . The visible ripples in the current waveforms are expected as these represent the inverter-side currents. In fact, a 10% THD has been calculated for these waveforms using the Yokogawa WT1800 power analyser. Nevertheless, since the THD of the grid-side currents is more important for a grid-connected inverter case, this has been calculated as 4.5%, which falls within the acceptable range according to the IEEE 519-2014 standard for low voltage grid applications [183, 184]. A further reduction of the THD can be achieved if inner current control loops are adopted or a different filter is selected. It is underlined that even if a different filter is selected, the RMS current-limiting property and the stability analysis presented in this part are still valid, as they do not depend on the particular values of the filter parameters L_f , C_f or L_g . However, in the case where inner current control loops are added to the controller implementation, further investigation is required for the stability analysis of the entire system. Nevertheless, the purpose of this work is to propose for the first time this novel control structure and simultaneously guarantee the stability in a rigorous manner. Thus, it has been verified that the proposed controller supports the grid via the desired droop control operation and additionally offers an inherent protection of the inverter against excessive power demands.

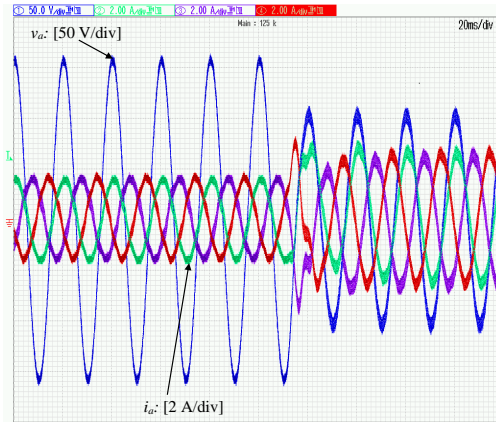
3.3.6.2 Operation under balanced grid voltage sags

To further validate the performance of the proposed control scheme, grid fault cases in terms of balanced voltage sags are examined in this section, while the inverter is operating in the desired droop control mode.

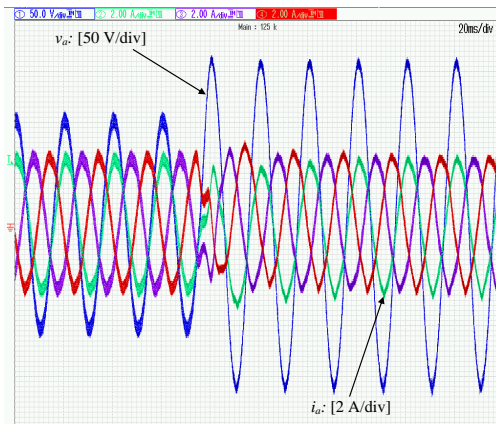
Initially, the grid voltage drops from 110 V to 70 V at $t'_1 = 11.6s$ in Figure 3.22a. During the fault, the RMS value of the current increases to its maximum value without violating the desired upper threshold. Hence, the proposed controller maximizes the power injection, while inherently protecting the inverter device. This



(a) Time response of P , Q , I_{rms} , V_{rms} and f

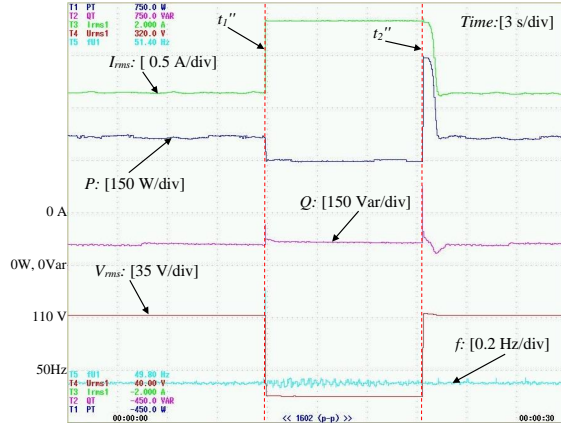


(b) Inverter currents and PCC phase-a voltage when the fault occurs

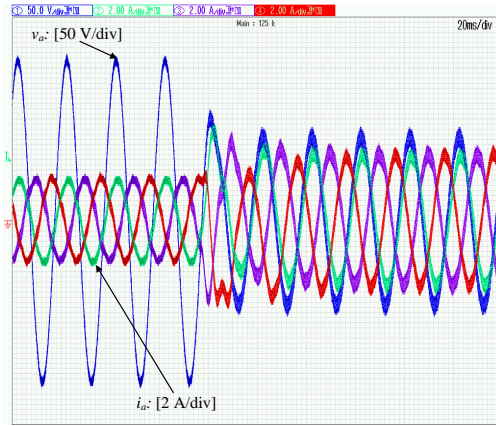


(c) Inverter currents and PCC phase-a voltage when the fault is cleared

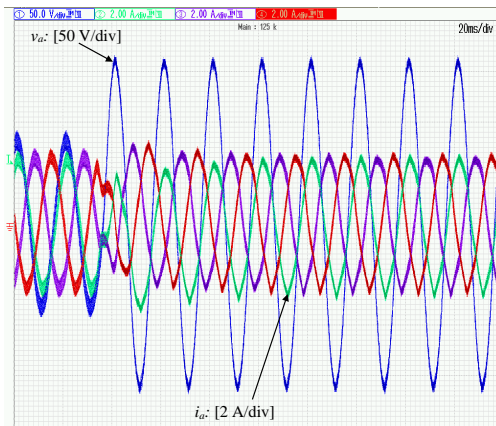
Figure 3.22: Grid-supporting inverter response under the proposed controller when a balanced voltage sag $110\text{ V} \rightarrow 70\text{ V}$ occurs.



(a) Time response of P , Q , I_{rms} , V_{rms} and f



(b) Inverter currents and PCC phase-a voltage when the fault occurs



(c) Inverter currents and PCC phase-a voltage when the fault is cleared

Figure 3.23: Grid-supporting inverter response under the proposed controller when a balanced voltage sag $110\text{ V} \rightarrow 55\text{ V}$ occurs.

operation can be theoretically explained as follows: when the fault appears, the controller state σ converges to its maximum value, which is $\frac{\pi}{2}$. In that case, the integration (3.66) tends to zero due to the cosine term in the dynamics, and therefore, acts like an inherent integrator anti-windup technique. As it is clear in Figure 3.22a, when the current is limited at 1.85 A, P increases to 384.6 W, which can be calculated as $(\sqrt{S^2 - Q^2} = \sqrt{(3 \times 1.85 \times 70)^2 - 55^2})$. When the fault is cleared at $t'_2 = 21s$, the real and reactive powers return to their original values, according to the droop control. In Figure 3.22b and Figure 3.22c, the transient response of the inverter current and the PCC voltage are depicted during the fault appearance and the fault clearance. It is underlined that due to the limited number of the channels available in the oscilloscope (4 in total), only one voltage (phase a) and three current measurements are shown in the Figures 3.22b, 3.22c, 3.23b, and 3.23c. Since the balanced voltage sags are examined, the other phases (b and c) of the grid voltage follow the same drop ratio as phase a. As it is clear, the RMS value of the inverter current never violates its maximum value, as desired.

In order to test the controller performance under larger grid voltage sags, experimental results where the grid voltage drops from 110 V to 55 V are provided in Fig 3.23a. When the fault appears at $t''_1 = 11.9s$, I_{rms} increases again to 1.85 A (i.e. very close to I_{rms}^{max}), while the reactive power remains at its steady-state value. Hence, the real power during this voltage drop can be calculated as 300 W ($\sqrt{S^2 - Q^2} = \sqrt{(3 \times 1.85 \times 55)^2 - 55^2}$), as depicted in Figure 3.23a. When the fault is cleared at $t''_2 = 21.3s$, the real and reactive powers return to their former values, after a short transient. Fault appearance and clearance under the 50% grid voltage drop can be observed in detail in Figure 3.23b and Figure 3.23c. As a result, the desired grid support capability of the inverter and its inherent RMS current-limiting property have been confirmed under both normal and faulty grid conditions that include balanced voltage sags verifying the theoretic contribution and the stability analysis presented in this work.

3.4 Conclusions

In this Chapter, advanced nonlinear controllers for three-phase grid-connected inverters with different output filters, such as L and LC, were proposed to ensure reliable, stable, and safe DER operations. The reason of using various output filters was to demonstrate that the proposed controllers can be modified and work equally effective under any output filter.

In the first section, a nonlinear current-limiting droop controller for a three-phase inverter connected to the grid through an LCL filter was proposed. The proposed controller includes traditional PI controllers with decoupling terms for the inner control loops and a nonlinear dynamic controller for the outer power control loop. Using the nonlinear dynamics of the system and input-to-state stability theory, the current-limiting property of the grid-side inverter currents was analytically proven based on the bounded controller dynamics and the virtual resistance that was introduced in the proposed control design. Both active and reactive power regulation and droop control with a guaranteed upper limit for the grid currents can be accomplished by the proposed nonlinear controller, which was validated via extensive simulation results of a grid-connected three-phase inverter to support the theoretic analysis of the proposed control approach.

In the second section, the main focus was to design a novel nonlinear PLL-less current-limiting controller for a three-phase grid-connected inverter. The controller is proposed using the synchronously rotating (dq) frame of the inverter. Voltage and frequency supports are realised at the PCC point by including the droop dynamics into the nonlinear controller dynamics. Considering the nonlinear dynamics of the system, the current-limiting property is proven for the injected inverter current using nonlinear ultimate boundedness theory. In addition, the closed-loop system stability is guaranteed for different values of the controller gains. The proposed controller performance and its stability properties are confirmed via detailed simulation results.

In the third section, a novel nonlinear current-limiting droop controller for three-phase grid-connected inverters has been introduced as an improvement to the method proposed in section two. The limitation of the RMS value of the inverter current was guaranteed for the first time without requiring adaptive saturation units through a rigorous analysis based on invariant set theory, under both a normal grid and balanced voltage sags. A detailed proof of the closed-loop asymptotic system stability was presented without requiring full knowledge of the inverter filter parameters, which also provides a useful guidance on the selection of the controller parameters for the control implementation. To emphasize the superiority of the proposed controller over existing current-limiting methods, extensive comparison studies have been realised. The theoretic contributions and the effectiveness of the proposed control scheme were confirmed using an experimental setup consisting of a three-phase grid-connected inverter operating under a normal grid and different levels of balanced voltage sags.

Chapter 4

Virtual synchronous control of three-phase inverters considering DC-link voltage dynamics

In the existing literature, several virtual inertia and damping methods, such as VISMA, synchronverter, VOC, and ViSynC, have been proposed to support the grid in inverter-based DER applications, as explained in Chapter 2.2. However, in these methods, inverter protection, particularly the current limitation, is mostly realised using saturation unit-based methods, and the closed-loop stability analysis is generally examined via root locus technique. Since saturation units may lead to system instability and the root locus method is valid only for the given system and controller parameters, a method that includes virtual inertia and damping properties and can ensure the current limitation and closed-loop system stability by providing analytic conditions is required for reliable DER operations. To achieve these tasks, a composite controller that combines the useful features of droop control and ViSynC is proposed in this chapter. The chapter is divided into two sections. The first section focuses on the controller design and gives preliminary simulation results for the DER system equipped with the proposed method [185]. In the second section, comprehensive closed-loop stability analysis with analytic stability conditions is provided and detailed comparison studies with the existing techniques are realised. The performance of the proposed method is tested via extensive HIL studies [186].

4.1 Three-phase inverters with virtual inertia and current limitation capabilities

In Chapter 3, the system modeling has been realised by assuming a constant DC voltage in the input side of the three-phase inverters. Although this can be a reasonable assumption in some DER applications, the intermittent behavior of RESs should be taken into consideration, and DC-link dynamics should be included in the system models. Therefore, in this section, an improved nonlinear controller structure, which inherits both virtual inertia (VI) and current-limiting properties in grid-connected voltage-source converters (VSCs), is proposed. The proposed method inherits the $V_{dc} \sim \omega$ droop control for inertia emulation and frequency control, and $Q \sim V$ droop control for AC voltage support. The current-limiting property, which is a critical issue for the protection of grid interface inverters throughout the operation, including the grid faults, is also ensured for VI-based VSCs. Furthermore, the small-signal stability of the system is examined considering the effects of different controller gains. To validate both the small-signal stability and the current-limiting property, extensive Matlab/Simulink simulations are performed.

4.1.1 Background and motivations

The priority in converter-based RES applications is to send the maximum power to the grid without considering the inertia requirements, which are critical for energy balance and system stability, dictated by the grid authorities [116]. However, even if providing inertia in DER applications is not a strictly applied requirement in some countries since a high percentage of energy production depends on SG-based sources in present operations, inertia will be one of the critical elements to increase the proportion of DER-based energy production in the future [21, 83]. As the majority of RESs are not capable of providing physical inertia, the VI concept has been first proposed in [100] for power electronic converters, and its various modifications such as synchronverters, VOC and VISMA have been published to deal with this problem [82] as explained in Chapter 2.2. In general, the current VI algorithms assume either constant or quasi-constant DC-link voltage, which may be acceptable in some specific applications, but this may not always be guaranteed due to the intermittent nature of the RESs. This problem is investigated by controlling the DC-link capacitor voltage for both inertia emulation and synchronization purposes in [116, 187].

Besides, as the power converters are operated via semiconductor switches, which

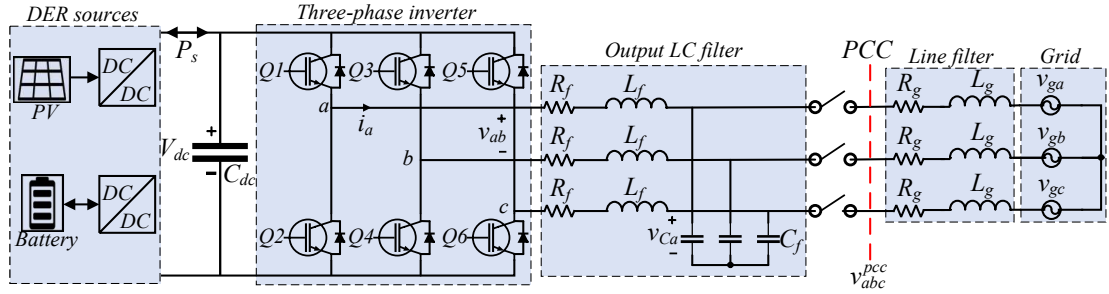


Figure 4.1: DER-sourced grid-connected VSC system

can be damaged in sudden abnormal situations, such as grid faults, the control algorithms should ensure that the critical system states, such as system currents, will remain within the desired limits to guarantee a reliable operation. To address this issue, a nonlinear droop control method, which can analytically prove the current-limiting property independently from the system parameters, unlike [179], has been proposed in [162] for single-phase inverters and in [171] for three-phase rectifiers. However, the applicability of this method for VI applications has not been proven yet. Therefore, there is a need for a controller that ensures the VSC current limitation at all times, even under grid faults, and utilizes the virtual synchronous control dynamics to provide virtual inertia to the system when required. Unlike [116], which uses saturated PI controllers in the control loops and cannot guarantee the current-limiting property and system stability at all times, an improved method that ensures the current-limiting property for the first time for VI-based inverters using the recently introduced state-limiting PI controller [181] is proposed in this section. Furthermore, the closed-loop stability is examined via small-signal system analysis and useful root locus plots by changing the controller gains are provided to guide the prospective users. This process is thoroughly explained in the following subsections.

4.1.2 Dynamic system modeling and necessary definitions

The system under inspection is a DER-sourced grid-connected three-phase inverter as shown in Figure 4.1. The filter parasitic resistance, inductance, and capacitor are described as R_f , L_f , C_f , respectively, while the line between the PCC and the main grid has a resistance R_g and an inductance L_g . The DER side is designed as a bidirectional power source (using a bidirectional DC/DC converter as given in Chapter 2.1), which can provide/absorb power to/from the AC side and its power is shown as P_s . V_{dc} and C_{dc} denote the DC-link voltage and capacitor. The balanced abc frame three-phase

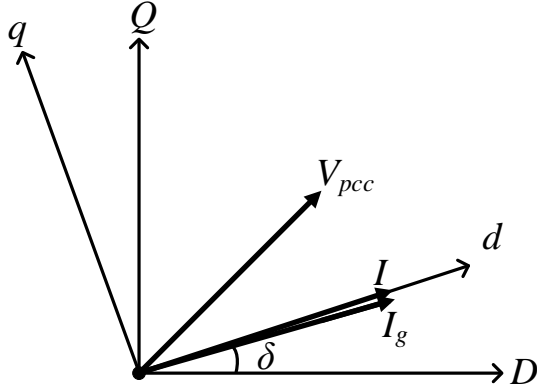


Figure 4.2: Vector diagram of local (dq) and global (DQ) PCC frames.

PCC voltages and their phase angle are denoted as v_{abc}^{pcc} and θ_g , respectively. Assuming the global dq frame PCC voltages are in the form of $V_d^{pcc} = \sqrt{2}V_{rms}$ and $V_q^{pcc} = 0$, using the reference frame transformation [26] as illustrated in Figure 4.2, the local (inverter) dq frame PCC voltages can be expressed as

$$\begin{bmatrix} V_{dl}^{pcc} \\ V_{ql}^{pcc} \end{bmatrix} = \begin{bmatrix} V_d^{pcc} \cos \delta \\ -V_d^{pcc} \sin \delta \end{bmatrix}, \quad (4.1)$$

where $\delta = \theta - \theta_g$ is the phase angle difference between the DER-sourced inverter and the PCC. Hence, the voltage dynamics of the system in the local inverter dq frame becomes

$$L_f \frac{di_d}{dt} = -R_f i_d + \omega L_f i_q - V_{dl}^{pcc} + V_d \quad (4.2)$$

$$L_f \frac{di_q}{dt} = -R_f i_q - \omega L_f i_d - V_{ql}^{pcc} + V_q \quad (4.3)$$

where i_d, i_q and V_d, V_q are the local dq frame inverter currents and voltages, while $\omega = \dot{\theta}$ is the angular frequency of the inverter. Thus, considering (4.1) and local frame inverter currents, the inverter active and reactive power can be obtained as

$$\begin{aligned} P &= \frac{3}{\sqrt{2}} V_{rms} (i_d \cos \delta - i_q \sin \delta) \\ Q &= -\frac{3}{\sqrt{2}} V_{rms} (i_d \sin \delta + i_q \cos \delta). \end{aligned} \quad (4.4)$$

It is clear from (4.4) that the power equations include nonlinear terms. Hence, nonlinear control design and analysis are essential to guarantee a stable behavior of the inverter when power control is required as pointed out in [57, 188]. It is important to mention that since the filter capacitor has very small values in real applications, in this section, the real and reactive power arriving at the filter capacitor are almost equal to the ones injected to the grid, as mentioned in [162]. Power control is generally implemented via droop control by either coupling $P \sim \omega$ and $Q \sim V$ in high power or inductive output applications or coupling $P \sim V$ and $Q \sim \omega$ in low power or resistive output applications [88, 152]. However, DC-link dynamics are generally ignored by assuming a constant DC voltage in the DER side, which is not realistic in practical applications. To this end, this section proposes a method, which combines the grid supporting features of the ViSynC approach combined with $Q \sim V$ droop control to introduce virtual inertia and damping, achieve RMS current limitation and accurate reactive power control, while guaranteeing the closed-loop system stability under balanced grid voltage sags.

4.1.3 Proposed nonlinear controller, RMS current limitation, and ViSynC integration

4.1.3.1 Proposed nonlinear controller and current limitation

In this part, the recently proposed sl-PI controller [181] is formulated in a way to achieve both the $Q \sim V$ droop control and the RMS inverter current limitation without using any saturation limits and additional anti-windup techniques. Contrary to the existing approaches [26], which align the local inverter voltage to the d -axis, the proposed control structure is based on the idea of aligning the local inverter current to the d -axis as shown in Figure 4.2, i.e. $i_q = 0$, in order to simplify the control implementation and facilitate the closed-loop system stability. To this end, the local dq frame inverter voltages are used as control inputs and formed as

$$V_d = V_{dl}^{pcc} + E_{max} \sin \sigma - r_v i_d - \omega L_f i_q \quad (4.5)$$

$$V_q = V_{ql}^{pcc} - r_v i_q + \omega L_f i_d \quad (4.6)$$

where r_v and E_{max} are the main parameters for the sl-PI controller and introduced as virtual resistor and voltage, respectively, to the DER-sourced inverter system. While $\omega L_f i_d$ and $\omega L_f i_q$ represent the dq transformation decoupling terms, σ is the sl-PI

controller state and designed as

$$\dot{\sigma} = \frac{c}{E_{max}} [(E^* - V_{rms}) - n(Q - Q_{set})] \cos \sigma \quad (4.7)$$

where c is the positive integral gain. As it is proven in [181], if the initial controller state σ_0 is chosen as $\sigma_0 \in [-\frac{\pi}{2}, \frac{\pi}{2}]$, it is ensured that $\sigma(t) \in [-\frac{\pi}{2}, \frac{\pi}{2}], \forall t \geq 0$. Furthermore, since $\dot{\sigma} \rightarrow 0$ when $\sigma \rightarrow \pm\frac{\pi}{2}$, then the controller inherently provides an integrator anti-windup property by slowing down the integration near the limits, opposed to conventional saturated integrators.

Note that the $Q \sim V$ droop operation is achieved by regulating the expression $(E^* - V_{rms}) - n(Q - Q_{set})$ to zero using the integrator feature of the sl-PI controller. In this expression, E^* , V_{rms} , n , and Q_{set} denote the rated RMS grid voltage, PCC RMS voltage, reactive power droop coefficient, and reactive power set value, respectively.

Replacing the proposed controller dynamics (4.5)-(4.6) in the system dynamics (4.2)-(4.3), the closed-loop system current dynamics can be obtained as

$$L_f \frac{di_d}{dt} = -(r_v + R_f)i_d + E_{max} \sin \sigma \quad (4.8)$$

$$L_f \frac{di_q}{dt} = -(r_v + R_f)i_q \quad (4.9)$$

The solution of q -axis current dynamics (4.9) can be obtained independently from the closed-loop system dynamics as $i_q(t) = i_q(0)e^{-\frac{(r_v+R_f)}{L_f}t}$, thus if initially $i_q(0) = 0$, then $i_q(t) = 0, \forall t \geq 0$. In order to ensure RMS current limitation and closed-loop stability, the controller parameter can be selected as $E_{max} = (r_v + R_f)I_d^{max}$, where $I_d^{max} = \sqrt{2}I_{rms}^{max}$ and I_{rms}^{max} is the maximum RMS current that the inverter can handle. More precisely, for $\forall t \geq 0$, it holds true that d -axis current i_d and the controller state σ remain in the intervals $[-\sqrt{2}I_{rms}^{max}, \sqrt{2}I_{rms}^{max}]$ and $[-\frac{\pi}{2}, \frac{\pi}{2}]$, respectively. Note that the current-limiting property holds for the original nonlinear system and it is also guaranteed independently of the large-signal system faults. The readers can refer to Chapter 3.2 for the current-limiting property and [181] for the controller state limitation, which are realised using nonlinear ultimate boundedness theory.

4.1.3.2 ViSynC integration

In this part, the ViSynC dynamics, which create an interaction between the DC and AC sides via the $V_{dc} \sim \omega$ droop operation, is combined with the remaining system dynamics (4.4)-(4.9) to provide virtual damping and inertia to the system in addition

$x_e = [i_{de} \sigma_e V_{dce}^2 \omega_e \delta_e]^T$, where $\sigma_e \in (-\frac{\pi}{2}, \frac{\pi}{2})$. Then, the Jacobian matrix of the closed-loop system becomes (4.12). As a result, the closed-loop system will be asymptotically stable, if all eigenvalues of the Jacobian matrix (4.12) have negative real parts.

$$J = \begin{bmatrix} -\frac{(r_v + R_f)}{L_f} & \frac{E_{max} \cos \sigma_e}{L_f} & 0 & 0 & 0 \\ A \sin \delta_e & 0 & 0 & 0 & A i_{de} \cos \delta_e \\ -B \cos \delta_e & 0 & 0 & 0 & B i_{de} \sin \delta_e \\ -\frac{B \cos \delta_e}{K_j} & 0 & \frac{K_T}{K_J} & -\frac{K_D}{K_J} & \frac{B i_{de} \sin \delta_e}{K_j} \\ 0 & 0 & 0 & 1 & 0 \end{bmatrix} \quad (4.12)$$

The notations A and B in (4.12) are given as $\frac{3\sqrt{2}cnV_{rms} \cos \sigma_e}{2E_{max}}$ and $\frac{3\sqrt{2}V_{rms}}{C_{dc}}$, respectively. In Figure 4.4, the closed-loop eigenvalue spectrum analysis is realised by adjusting the damping gain K_D between 500 and 3000, the inertia emulation gain K_J between 5 and 20, the DC voltage tracking gain K_T between 0.2 and 10, and the integral gain c between 100 and 10000 using the system and controller parameters given in Table 4.1. The numbers and arrows in Figure 4.4 define the system poles and their directions (either left or right parts of the complex plane with respect to zero) as the controller gains change. For example, while increasing K_D moves the lightly damped poles (2 and 3) towards the left direction on the complex plane, increasing K_J , K_T , and c moves them towards the right direction on the complex plane. Thus, the effectiveness and small-signal stability margins of the proposed controller are proven for broad ranges of the controller gains, which can give clear guidance to the prospective users for their applications.

Table 4.1: DER-based simulated inverter system and controller parameters

Parameters	Values	Parameters	Values
L_f, L_g	2.2mH	S_{max}	990VA
R_f, R_g	0.5Ω	r_v	100Ω
n	0.011	C_{dc}	1mF
ω_g	2π50	V_{dcref}	350V
c	5000	E^*	110V
I_{max}	4.24A	K_T	4
K_j	10	K_D	1000

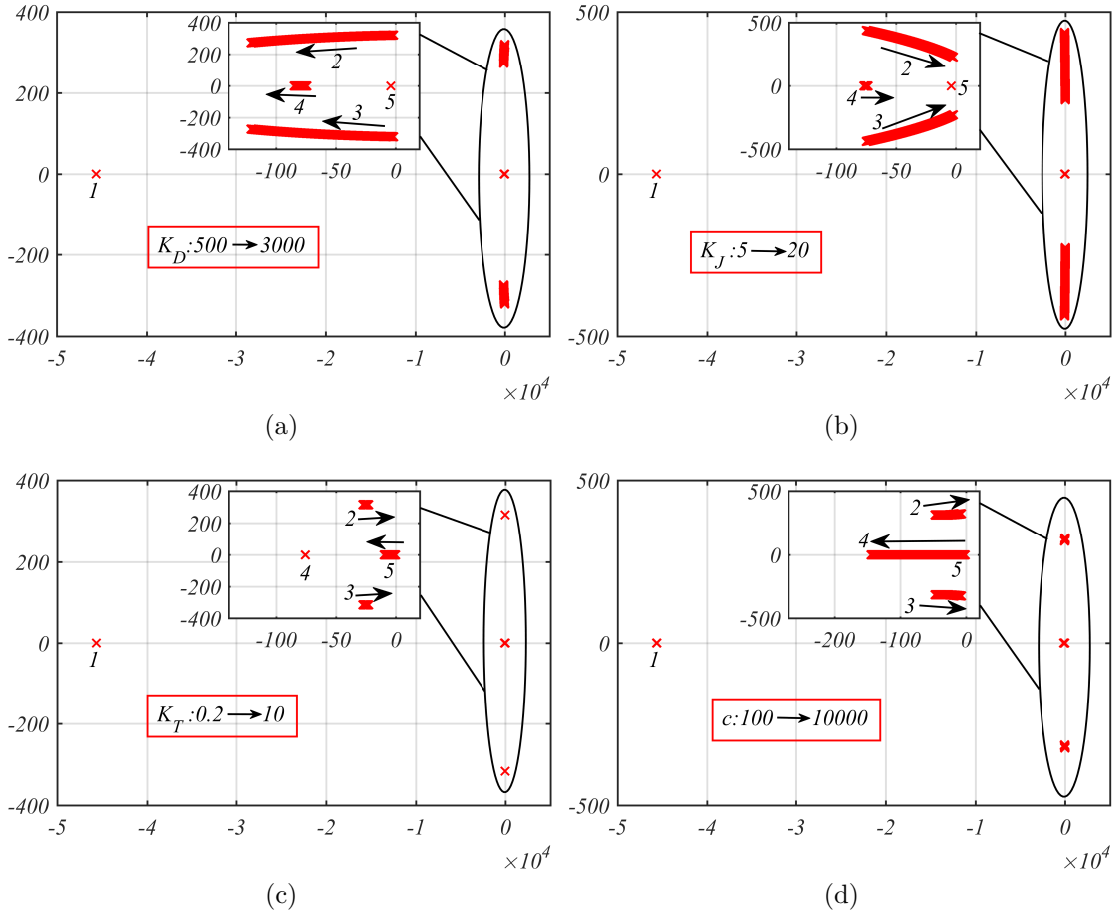


Figure 4.4: Closed-loop eigenvalue spectrum as a function of K_D (a), K_J (b), K_T (c), and c (d).

4.1.5 Simulation results

To verify the proposed controller performance, a DER-sourced VSC connected to the grid via an LC filter and a line, as shown in Figure 4.1, is simulated in the Matlab/Simulink software environment. The system and controller parameters used in the simulations are given in Table 4.1. During the whole operation, the $Q \sim V$ droop control is enabled, and the nominal grid frequency is used. Initially, the DER power P_s is set to 400W and the reactive power set value Q_{set} is taken as 300Var. At $t = 3s$, P_s is increased to 800W, while Q_{set} is kept as 300Var. To emphasize the bidirectional operation of the VSC, at $t = 7s$, P_s is changed to $-500W$, which is the case the DER demands power from the VSC, and at $t = 11s$, P_s is set to 600W. At $t = 15s$, Q_{set} is increased to 500Var to prove the ability of the VSC to provide more reactive power when required. As can be seen in Figure 4.5, the proposed controller regulates the inverter active power to almost equal values of DER power P_s . Since the $Q \sim V$ droop

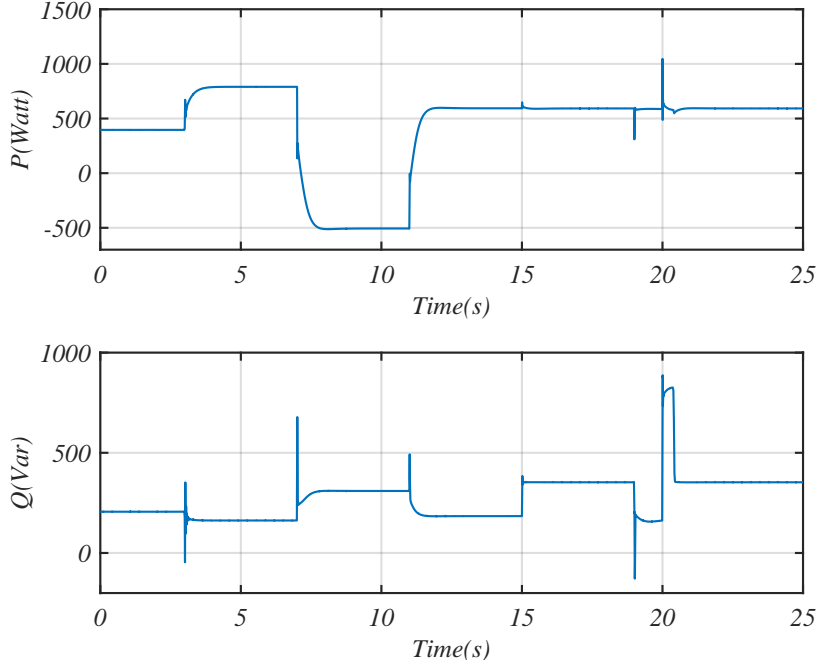


Figure 4.5: Active and reactive power.

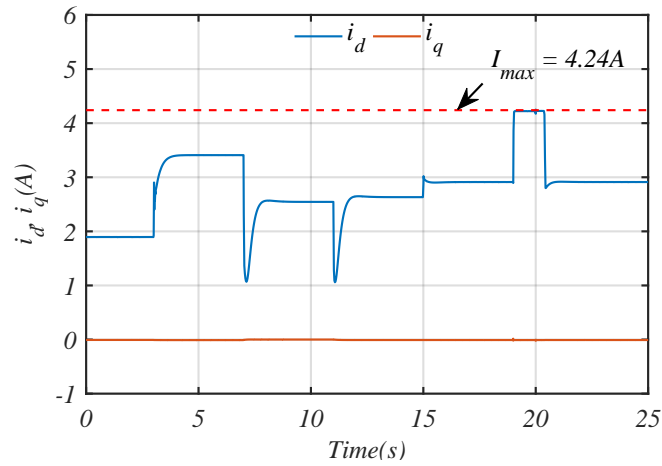


Figure 4.6: Inverter i_d and i_q currents.

operation is enabled, the inverter reactive power is regulated to a lower steady-state value, which can be computed as $\frac{E^* - V_{rms}}{n} + Q_{set}$ to keep the RMS voltage close to its rated value. The RMS voltage is provided, in Figure 4.8, to confirm the steady-state Q values for every operation point change.

To validate the proposed current-limiting property, at $t = 19s$, a $40V$ grid voltage drop is implemented as shown in Figure 4.8, and at $t = 20s$, the grid voltage is recovered. As it is clear in Figure 4.6, the d -axis current goes to its maximum value I_{max} , while q -axis current is kept as zero, which justifies the current-limiting property

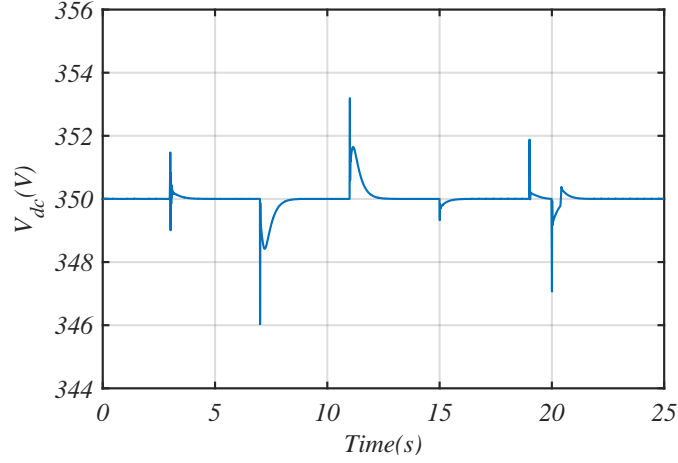


Figure 4.7: DC-link voltage.

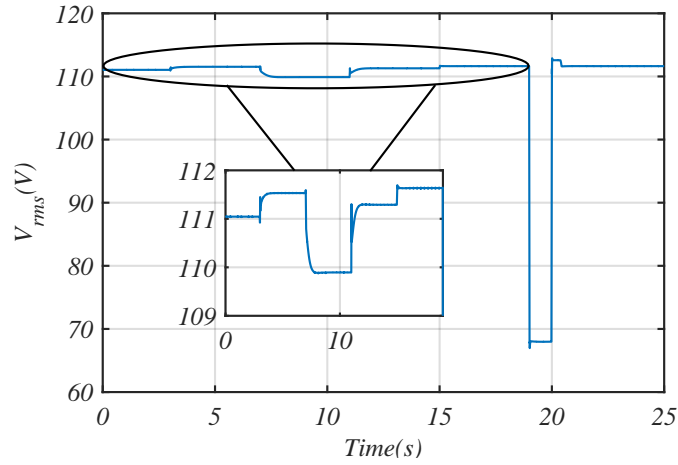


Figure 4.8: RMS voltage.

of the proposed controller. Besides, the system recovery after the fault is completed almost instantly; thus, the controller inherently solves the integrator wind-up problem. In addition, the DC-link voltage is controlled very close to its reference value, even in the transients, to avoid any potential protection trip, as shown in Figure 4.7. The high-frequency transients, which exist in Figures 4.5 and 4.7, can be removed by increasing the damping gain K_D as shown in Figure 4.4.

4.2 Current-limiting virtual synchronous control and stability analysis considering DC-link dynamics

In the previous section, a nonlinear controller that can ensure the current limitation and provide virtual inertia in inverter-based DER applications has been introduced, and preliminary simulation results have been presented. However, rigorous stability analysis and comparison studies with the existing methods have not been realised. In addition, the proposed method has not been implemented in a real-time controller and system. Therefore, in this section, the closed-loop stability of the entire system is rigorously proven using nonlinear singular perturbation theory. Moreover, analytic conditions for the controller parameter selection to guarantee the stability of the entire inverter system with the DC-link dynamics are provided. To prove the effectiveness of the proposed controller and its superior performance compared to the traditional approaches, extensive Matlab/Simulink-based simulations are performed, followed by Typhoon-HIL hardware-in-the loop implementation using a TI microcontroller.

4.2.1 Background and motivations

The behavioral characteristics of the SGs can be mimicked via the droop control approaches, such as conventional, adaptive, robust and universal droop control [88], while physical SG dynamics can be resembled via VSG methods, such as synchronverter, virtual synchronous machine, and synchronous power controller [21]. Although droop control techniques can improve the voltage and frequency control and VSG methods can provide synthetic inertia to balance the system for stability enhancement, both approaches may suffer from the overshoots, current limit violations, and stability problems if a large disturbance, such as a drastic voltage sag, occurs [189, 190]. Therefore, virtual synchronous control (ViSynC) approaches have started to gain attention since they can merge the useful features of the droop control and VSG techniques by utilizing both the DC and AC side system dynamics [116, 117] and offer better disturbance rejection ability compared to the previously mentioned approaches in case of system faults [189].

Opposed to SGs, VSGs are responsible for the reactive power regulation through their separate reactive power control (RPC) loops. Therefore, RPC can have a considerable effect on the system stability under the grid voltage sags due to the shifting of the operating point [190, 191]. Furthermore, inverter current limitation in case of abnormal

system conditions is another important issue for a safe and reliable DG operation and it is generally realised either via switching between different control algorithms [192] in VSGs or by using adaptive saturation methods [116, 130] in ViSynC approaches. Since the current limitation is a critical issue for a reliable power transfer operation in DER applications, considerable research effort is allocated in this topic. Virtual impedance-based methods [99, 128, 155] are one of the main approaches, which can be used for the purpose of current limitation for particular applications. In particular, a virtual impedance-based current-limiting algorithm is proposed for grid-forming converters in [193]. However, this method requires the threshold and maximum current values to be different; hence, it may need higher power rated circuit components for lower power applications. Moreover, the authors in [79] propose a method which has inherent current-limiting property for grid-forming inverters, but no analytic stability condition is provided to guide the prospective users for controller parameter selection, i.e., the stability is guaranteed only for a given set of system parameters and cannot be generalised for any converter. Furthermore, the authors in [118, 120, 194] offer current-limiting algorithms specifically for VSG converters considering various grid and load conditions. Even though the method in [194] can limit the harmonic and inrush fault current, it uses limiters in the control algorithm and requires knowledge of the grid-side line parameters in the control design process. In [118], a method that can limit transient inrush currents in synchronverters is proposed. However, this method does not include stability analysis and it may be difficult to implement since there are many algorithm changes. An MPC based fault current limiter is proposed in [120], which offers satisfactory results, but significantly increases the computational cost of the controller implementation.

To this end, the previously mentioned techniques do not offer a rigorous stability analysis, cannot guarantee the desired instantaneous current limitation at all times, including large transients, cannot ensure that the system will recover to its stable operating points after a large disturbance due to unresolved integrator windup issue, and may eventually lead to system instability [124]. To address the integrator windup issue and guarantee the closed-loop system stability, the bounded integral control (BIC) concept has been proposed in [167], and applied to synchronverters [109] and three-phase rectifiers [171]. Recently, as an enhancement to the original BIC, a state-limiting PI (sl-PI) controller [181], which introduces less controller states and leads to easier implementation, has been proposed and applied to three-phase inverters [152]. However, all of these applications assume constant DC input voltage dynamics and ignore the effect of variable DC voltage on the system stability.

The main contributions offered in this part of the thesis are outlined in the following: 1) the DC-link dynamics are incorporated into the existing three-phase grid-connected inverter dynamics, which is also equipped with sl-PI controller, to build a more realistic nonlinear system model, provide virtual inertia and damping to the system, and achieve bidirectional power transfer opposed to [109, 171] and [152], which assume a constant DC voltage; 2) the current-limiting property is guaranteed for the instantaneous values of the current instead of the reference values without employing saturation based methods contrary to [116, 130] and [194] and without assuming small-signal stability as in virtual impedance and saturation unit based methods [99, 128, 155]; 3) the closed-loop stability of the entire system is proven using singular perturbation theory instead of root locus or bode diagram methods as in [79, 118, 194] for the first time for three-phase inverters fed by RESs, and analytic stability and system parameter selection conditions are provided to guide the prospective users; 4) comprehensive comparison studies with the commonly-used current-limiting techniques considering the effect of well-known clamping anti-windup method are performed via Matlab/Simulink software; and 5) extensive Hardware-In-the-Loop (HIL) results using a Typhoon-HIL device and a TI F28379D launchpad are presented to prove the effectiveness of the proposed approach compared to state-of-the-art current-limiting algorithms.

4.2.2 Closed-loop stability analysis

Since the system modeling, proposed nonlinear controller, RMS current limitation, and ViSynC integration parts are similar with Chapter 4.1, these are omitted here. As clearly explained in Chapter 4.1, the proposed controller can ensure a desired RMS current-limitation of the inverter based on the sl-PI control structure. However, the stability of the closed-loop system including the DC link dynamics has not been proven yet. Opposed to conventional approaches that use root locus analysis which investigates the stability of an inverter system for a specific set of parameters, here, singular perturbation theory [57, 164] will be used to obtain analytic stability conditions that can also inform the controller parameter selection (e.g. relationship between virtual inertia and damping values).

4.2.2.1 Closed-loop system

By considering (4.7), (4.8), (4.10), (4.11) and $\dot{\delta} = \omega - \omega_g$, and omitting the i_q dynamics (4.9) from the system since $i_q(t) = 0, \forall t \geq 0$, the closed-loop system can be formed as

$$\begin{bmatrix} \dot{i}_d \\ \dot{\sigma} \end{bmatrix} = \begin{bmatrix} L_f^{-1}(r_v + R_f)(-i_d + \sqrt{2}I_{rms}^{max} \sin \sigma) \\ cE_{max}^{-1} [(E^* - V_{rms}) - n(Q - Q_{set})] \cos \sigma \end{bmatrix} \quad (4.13)$$

$$\begin{bmatrix} \dot{V}_{dc}^2 \\ \dot{\omega} \\ \dot{\delta} \end{bmatrix} = \begin{bmatrix} C_{dc}^{-1}(2P_s - 3\sqrt{2}V_{rms}i_d \cos \delta) \\ C_{dc}^{-1}K_J^{-1}(2P_s - 3\sqrt{2}V_{rms}i_d \cos \delta \\ + C_{dc}(K_T(V_{dc}^2 - V_{dcref}^2) + K_D(\omega_g - \omega))) \\ \omega - \omega_g \end{bmatrix} \quad (4.14)$$

For the above system, consider the following assumption.

Assumption 1 (Time-scale separation): The parameters of the equations (4.7), (4.8), and (4.10) should satisfy

$$\max \left\{ \frac{L_f}{r_v + R_f}, \frac{1}{c} \right\} \ll C_{dc} \quad (4.15)$$

Assumption 1 is necessary in order to separate the equations (4.7) and (4.8) from the ViSynC dynamics (4.10), (4.11), and $\dot{\delta} = \omega - \omega_g$ for a simple closed-loop stability analysis. Note that Assumption 1 can be easily satisfied by choosing the appropriate values for the controller parameters (r_v and c), which can be accomplished by the control operator, compared to the system parameters (L_f and C_{dc}). To ensure the time-scale separation, C_{dc} should have much larger values than $\max \left\{ \frac{L_f}{r_v + R_f}, \frac{1}{c} \right\}$, e.g., at least ten times larger as a rule of thumb. As an example, one can check that this condition is satisfied in the system parameters provided in the simulation and HIL implementation cases (Table 4.2).

Consider an equilibrium point $x_e = [i_{de} \ \sigma_e \ V_{dce}^2 \ \omega_e \ \delta_e]^T$ obtained from (4.13)-(4.14) at the steady state where $\sigma_e \in (-\frac{\pi}{2}, \frac{\pi}{2})$. By setting $\epsilon = \frac{1}{\min \left\{ \frac{r_v + R_f}{L_f}, c \right\}}$, there exist $\gamma_a \geq 0$ and $\gamma_b \geq 0$ such that $\frac{r_v + R_f}{L_f} = (1/\epsilon) + \gamma_a$ and $c = (1/\epsilon) + \gamma_b$. Thus, (4.13) can be rewritten as

$$\begin{bmatrix} \epsilon \dot{i}_d \\ \epsilon \dot{\sigma} \end{bmatrix} = \begin{bmatrix} 1 + \epsilon \gamma_a & 0 \\ 0 & 1 + \epsilon \gamma_b \end{bmatrix} \begin{bmatrix} (-i_d + \sqrt{2}I_{rms}^{max} \sin \sigma) \\ E_{max}^{-1} [(E^* - V_{rms}) - n(Q - Q_{set})] \cos \sigma \end{bmatrix}. \quad (4.16)$$

Thus, the closed-loop system equations (4.14) and (4.16) can be written in the form of

$$\dot{x} = f(x, z) \quad (4.17)$$

$$\epsilon \dot{z} = g(x, z, \epsilon) \quad (4.18)$$

$$x = \begin{bmatrix} V_{dc}^2 - V_{dce}^2 \\ \omega - \omega_e \\ \delta - \delta_e \end{bmatrix} \quad z = \begin{bmatrix} i_d - i_{de} \\ \sigma - \sigma_e \end{bmatrix}.$$

For the arbitrarily large values of the virtual resistor r_v and integral gain c , which are the controller parameters, the ϵ value is small and, thus, (4.17)-(4.18) can be examined as a singularly perturbed system through the two-time-scale analysis [164]. The system (4.16) is called as boundary layer, because it represents the immediate vicinity of a bounding surface as mentioned in [164, 195].

4.2.2.2 Boundary layer analysis

Considering f, g are continuously differentiable in the domain $(x, z, \epsilon) \in D_x \times D_z \times [0, \epsilon_0]$, when the system and controller parameters are selected according to Assumption 1, then $\epsilon \rightarrow 0$ and, based on singular perturbation theory, g will have an algebraic form of $0 = g(x, z)$. The roots of the system can be calculated as

$$\begin{aligned} \bar{i}_d &= \sqrt{2} I_{rms}^{max} \sin \bar{\sigma} \\ \bar{\sigma} &= \sin^{-1} \left(\frac{1}{3V_{rms} \sin \delta I_{rms}^{max}} \left(\frac{V_{rms} - E^*}{n} - Q_{set} \right) \right) \end{aligned} \quad (4.19)$$

These roots can be assigned as $z = h(x)$ with $\bar{i}_{de} \in [-\sqrt{2} I_{rms}^{max}, \sqrt{2} I_{rms}^{max}]$, and $\bar{\sigma}_e \in (-\frac{\pi}{2}, \frac{\pi}{2})$, such that $h(0) = 0$. Thus, the roots can also be regarded as the equilibrium points of the nonlinear systems (4.13) and (4.14). Exponential stability at the origin can be examined using the boundary layer system Jacobian matrix as below

$$J_1 = \begin{bmatrix} -\frac{(r_v + R_f)}{L_f} & \frac{E_{max} \cos \bar{\sigma}}{L_f} \\ \frac{3c}{\sqrt{2} E_{max}} n \cos \bar{\sigma} V_{rms} \sin \delta & 0 \end{bmatrix} \quad (4.20)$$

The characteristic equation of the system (4.20)

$$\lambda^2 + \frac{(r_v + R_f)}{L_f} \lambda - \frac{3\sqrt{2} c n \cos^2 \bar{\sigma} V_{rms} \sin \delta}{2L_f} = 0 \quad (4.21)$$

By applying the Routh-Hurwitz criterion, in order for all eigenvalues to have negative real parts, the following two stability conditions are obtained:

$$\sin \delta < 0 \quad (4.22)$$

$$\bar{\sigma} \in \left(-\frac{\pi}{2}, \frac{\pi}{2}\right) \quad (4.23)$$

Although (4.23) can be guaranteed by the proposed controller and the equilibrium point under consideration, condition (4.22) will be investigated in the sequel.

4.2.2.3 Reduced system analysis

The reduced model can be found by replacing the roots \bar{i}_d and $\bar{\sigma}$ in (4.14) as

$$\begin{bmatrix} \dot{V}_{dc}^2 \\ \dot{\omega} \\ \dot{\delta} \end{bmatrix} = \begin{bmatrix} C_{dc}^{-1} \left(2P_s - 2 \cot \delta \left(\frac{V_{rms} - E^*}{n} - Q_{set} \right) \right) \\ C_{dc}^{-1} K_J^{-1} \left(2P_s - 2 \cot \delta \left(\frac{V_{rms} - E^*}{n} - Q_{set} \right) \right) \\ + C_{dc} (K_T (V_{dc}^2 - V_{dcref}^2) + K_D (\omega_g - \omega)) \\ \omega - \omega_g \end{bmatrix} \quad (4.24)$$

The model (4.24) is usually called as quasi-steady-state model, since \bar{i}_d and $\bar{\sigma}$ introduce a velocity $[\dot{\bar{i}}_d \ \dot{\bar{\sigma}}] = \epsilon^{-1}g$ being very large when ϵ is small and $g \neq 0$, inducing a rapid convergence to a root $h(V_{dc}^2, \omega, \delta)$, which is also the equilibrium of the boundary layer system.

Considering (4.24), the equilibrium point vector of the reduced system $x_e = [V_{dce}^2 \ \omega_e \ \delta_e]$ can be computed as

$$a) V_{dce}^2 = V_{dcref}^2 \quad (4.25)$$

$$b) \omega_e = \omega_g \quad (4.26)$$

$$c) \delta_e = \cot^{-1} \left(\frac{P_s}{\left(\frac{V_{rms} - E^*}{n} - Q_{set} \right)} \right) \quad (4.27)$$

To investigate the reduced model closed-loop stability, its Jacobian matrix is given below

$$J_2 = \begin{bmatrix} 0 & 0 & \frac{2}{C_{dc} \sin^2 \delta_e} \left(\frac{V_{rms} - E^*}{n} - Q_{set} \right) \\ \frac{K_T}{K_J} & -\frac{K_D}{K_J} & \frac{2}{C_{dc} K_J \sin^2 \delta_e} \left(\frac{V_{rms} - E^*}{n} - Q_{set} \right) \\ 0 & 1 & 0 \end{bmatrix}. \quad (4.28)$$

The characteristic equation of the system (4.28) can be obtained as

$$\lambda^3 + \frac{K_D}{K_J} \lambda^2 - \frac{2 \left(\frac{V_{rms} - E^*}{n} - Q_{set} \right)}{C_{dc} K_J \sin^2 \delta_e} \lambda - \frac{2 K_T \left(\frac{V_{rms} - E^*}{n} - Q_{set} \right)}{C_{dc} K_J \sin^2 \delta_e} = 0 \quad (4.29)$$

By employing the Routh-Hurwitz criterion, for all system eigenvalues to have negative real parts, the following three stability conditions are obtained:

$$\frac{K_D}{K_J} > 0 \quad (4.30)$$

$$\left(\frac{V_{rms} - E^*}{n} - Q_{set} \right) < 0 \quad (4.31)$$

$$K_D > K_J K_T \quad (4.32)$$

Since the gains K_D and K_J are positive, condition (4.30) always holds. Condition (4.32) can be guaranteed with the choice of ViSynC gains and it also gives guidance to the users for the appropriate gain selection. In order to ensure that the system will have sufficient damping to avoid undesired oscillations, it is recommended to choose the gains considering $K_D \gg K_J K_T$ (at least ten times bigger as a rule of thumb). Finally, conditions (4.31) and (4.22) can be combined considering (4.27) and following intervals for the power angle can be derived,

$$\pi(2n - 1) < \delta_e < \frac{\pi}{2}(4n - 1) \quad n \in \mathbb{Z} \quad (4.33a)$$

$$\frac{\pi}{2}(4n - 1) < \delta_e < 2\pi n \quad n \in \mathbb{Z} \quad (4.33b)$$

Equation (4.33a) is valid when the DER power (P_s) is positive, while equation (4.33b) shows the case when P_s is negative, underlining that stability can be guaranteed for a bidirectional flow of the real power, as required in energy storage devices. Note also that (4.33a) and (4.33b) validate condition (4.22) for the desired equilibrium point, as originally required.

Remark: Figure 4.9 is plotted considering (4.27) and gives a guidance on selecting the DER power (P_s) and reactive power set value (Q_{set}) for various values of V_{rms} to guarantee the conditions (4.22) and (4.31), using the HIL system parameters provided in Table 4.2.

Therefore, based on the above conditions, the matrices J_1 and J_2 are Hurwitz, and there exist $\eta_1 > 0$ and $\eta_2 > 0$ and domains $\tilde{D}_z = \{z \in \mathbb{R}^2, \|z\|_2 < \eta_1\}$, where $\tilde{D}_z \subseteq D_z$ and $\tilde{D}_x = \{x \in \mathbb{R}^3, \|x\|_2 < \eta_2\}$, where $\tilde{D}_x \subseteq D_x$, such that both the boundary layer model (4.18) and reduced system (4.17) are exponentially stable at the origin.

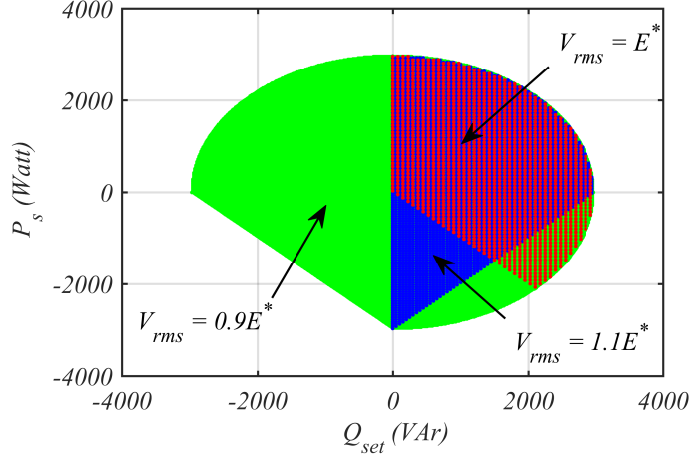


Figure 4.9: Regions for selecting P_s and Q_{set} to ensure closed-loop stability.

To this end, according to Theorem 11.4 in [164], there exists ϵ^* such that for all $\epsilon < \epsilon^*$, the equilibrium point $x_e = [i_{de} \ \sigma_e \ V_{dce}^2 \ \omega_e \ \delta_e]^T$ of (4.17)-(4.18) with $i_{de} \in [-\sqrt{2}I_{rms}^{max}, \sqrt{2}I_{rms}^{max}]$ and $\sigma_e \in (-\frac{\pi}{2}, \frac{\pi}{2})$ is exponentially stable; thus completing the stability analysis of the entire system.

It should be underlined that since the final stability conditions are found using the Routh-Hurwitz criterion under the worst-case scenarios (i.e., if these conditions hold, then stability is certainly guaranteed), the provided conditions represent the sufficient conditions to guarantee closed-loop system stability and not necessary conditions. Therefore, if the conditions hold, the system will be stable, but if they do not hold, this does not necessarily mean that the system will be certainly led to instability. Besides, it is important to mention that filter capacitor and grid-side line dynamics have been ignored in the system analysis, and their effects on system stability require further research.

4.2.3 Comparison with the existing methods

In this part, comparison simulation studies based on Matlab/Simulink are realised to justify the theoretical analysis and underline the superior features of the proposed controller scheme compared to the existing approaches. In particular, the current-limiting capability and effect of the ViSynC gains on the dynamic system performance are investigated by comparing the proposed method and original method [116], which uses an adaptive current limitation algorithm. The power system and controller parameters are given in Table 4.2. In the following part, the comparison test scenarios are explained in detail.

Table 4.2: DER-based inverter system and controller parameters for comparison and HIL studies

Parameters	Values	Parameters	Values
Power System Parameters			
L_f	5.8 mH	L_g	2.2 mH
R_f, R_g	0.5 Ω	V_{dcref}	350 V
ω_g	2 π 50 rad/s	C_f	1 μ F
Simulation		HIL	
S	990 VA	S	2970 VA
E^*	155 V	E^*	110 V
I_{rms}^{max}	3 A	I_{rms}^{max}	9 A
C_{dc}	1000 μ F	C_{dc}	2000 μ F
Proposed Controller Parameters			
Simulation		HIL	
n	0.0314 V/VAr	n	0.0037 V/VAr
r_v	200 Ω	r_v	30 Ω
c	15000	c	20000
Existing ViSynC Parameters			
k_{pi}, k_{ii}	0.5, 12	k_{pv}, k_{iv}	0.02, 0.2
K_Q	0.1 V/VAr	V_{qref}	100 V
R_v	0.05 Ω	L_v	0.5 mH
DC-link Controller Parameters			
Simulation		HIL	
K_T	4 Nm/V ²	K_T	4 Nm/V ²
K_J	10 kgm ²	K_J	10 kgm ²
K_D	2500 Nms	K_D	3000 Nms
Comparison HIL Parameters			
RCS		CSA	
k_{pi}, k_{ii}	10, 50	k_{pi}, k_{ii}	10, 50
k_{pv}, k_{iv}	10, 100	k_{pv}, k_{iv}	10, 100

Scenario I: The simulation starts with 600 W DER input power (P_s) and 400 VAr reactive power reference (Q_{set}). Then, at $t = 4s$, P_s is increased to 800 W, at $t = 8s$, P_s is changed to -500 W to demonstrate the bidirectional active power flow capability of the proposed approach, and at $t = 12s$, P_s is recovered to 600 W. Finally, at $t = 16s$, 40% balanced grid voltage sag is applied and cleared at $t = 17s$. The simulation ends at $t = 20s$. Figure 4.10 illustrates this scenario for various values of inertia (K_J) gains. For the original system [116], clamping anti-windup technique is applied in the inner voltage and current PI controllers as mentioned in [130]. The upper (a, b, c, d) subfigures in Figure 4.10 show that the original controller [116] can lead to inaccurate reactive power control due to the saturated PI controllers in the inner voltage loop when the DER source demands power, aggressive transients, and current limit

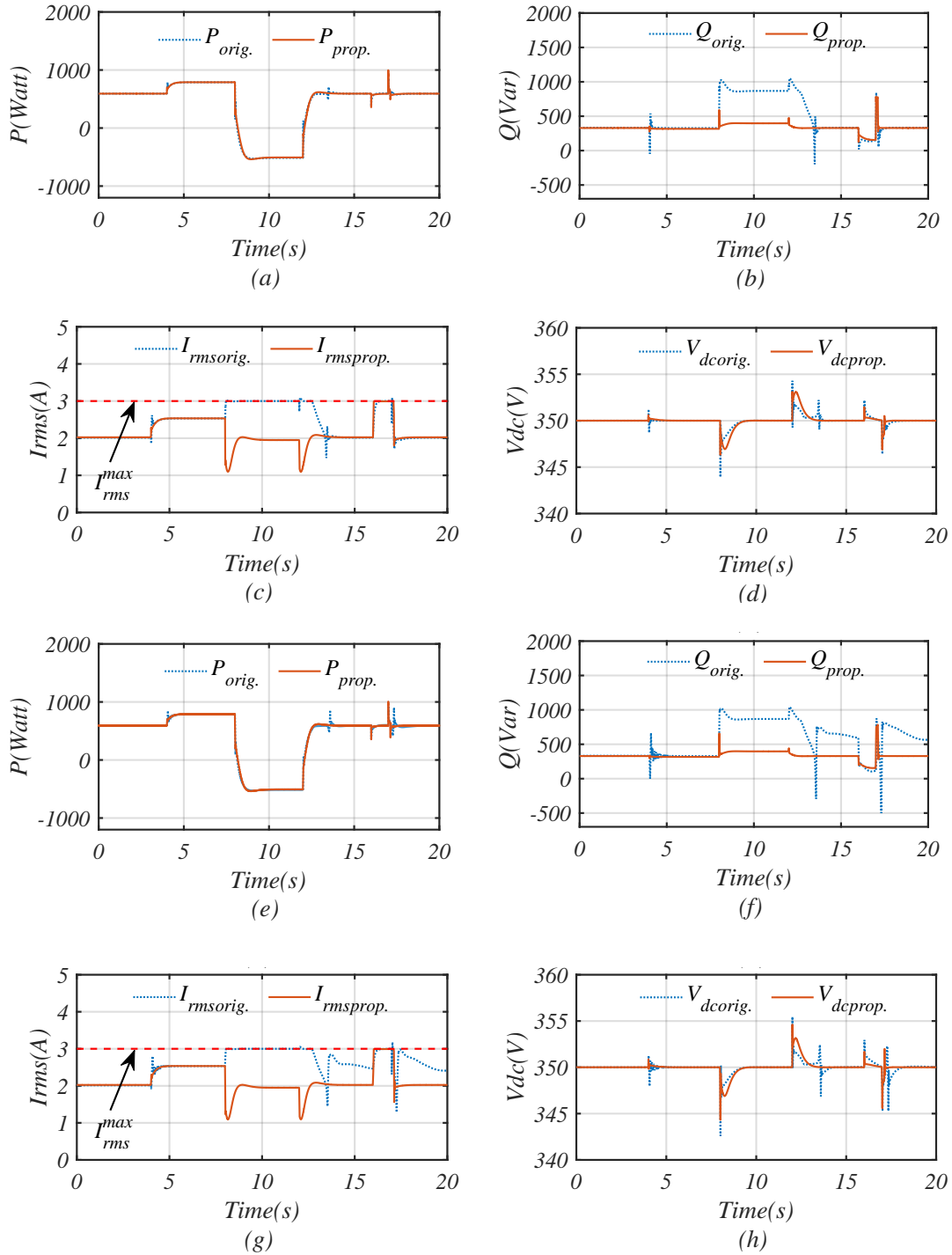


Figure 4.10: Performance comparison of the original [116] and the proposed controller. (a), (b), (c), and (d) with $K_J = 10 \text{ kgm}^2$, (e), (f), (g), and (h) with $K_J = 50 \text{ kgm}^2$, while $K_T = 4 \text{ Nm/V}^2$ and $K_D = 2500 \text{ Nms}$.

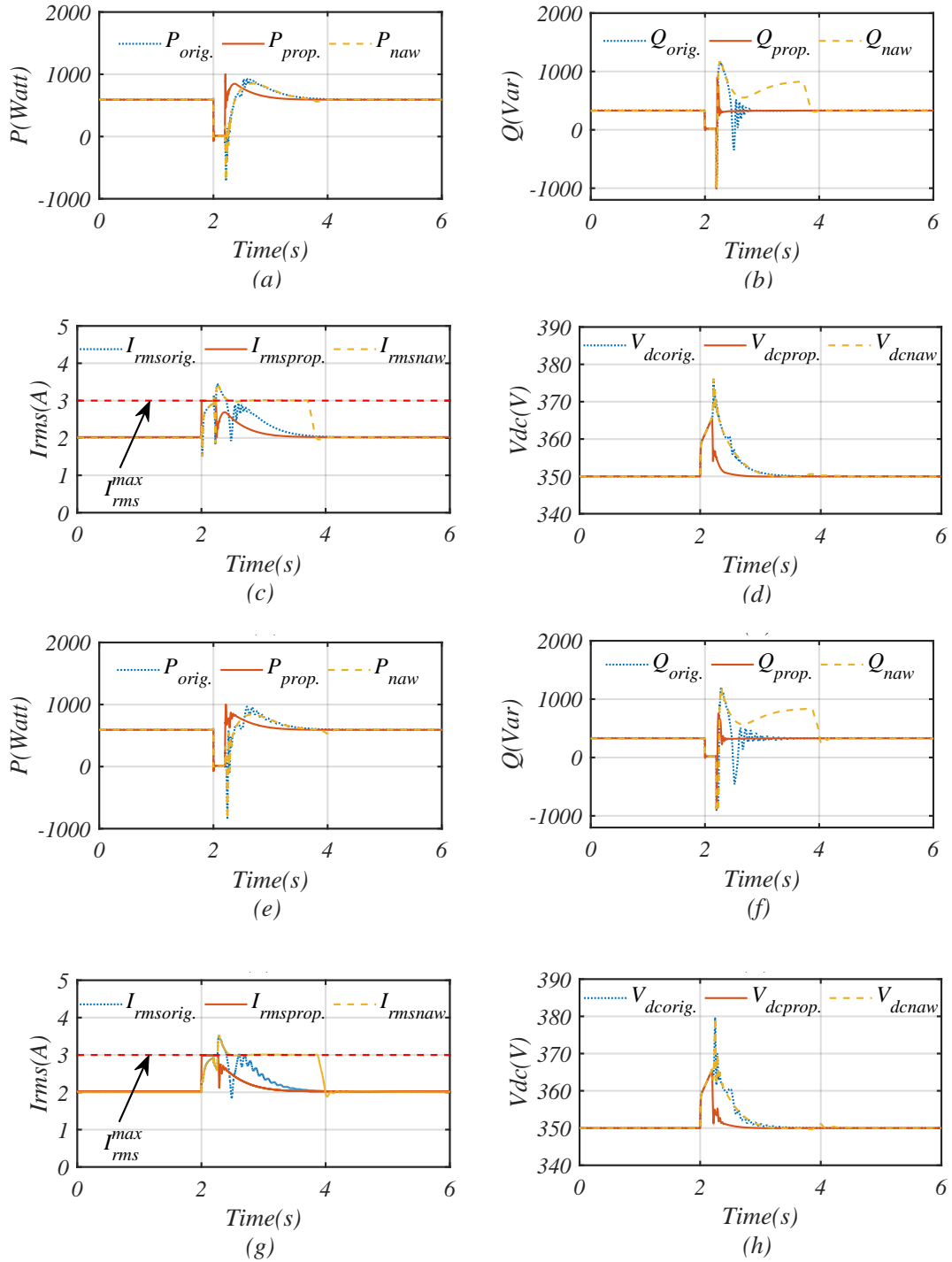


Figure 4.11: Performance comparison of the original [116], with (orig.) and without (naw) anti-windup techniques, and the proposed controller in case of a short-circuit (a), (b), (c), and (d) with $K_J = 10 \text{ kgm}^2$, (e), (f), (g), and (h) with $K_J = 50 \text{ kgm}^2$, while $K_T = 4 \text{ Nm/V}^2$ and $K_D = 2500 \text{ Nms}$.

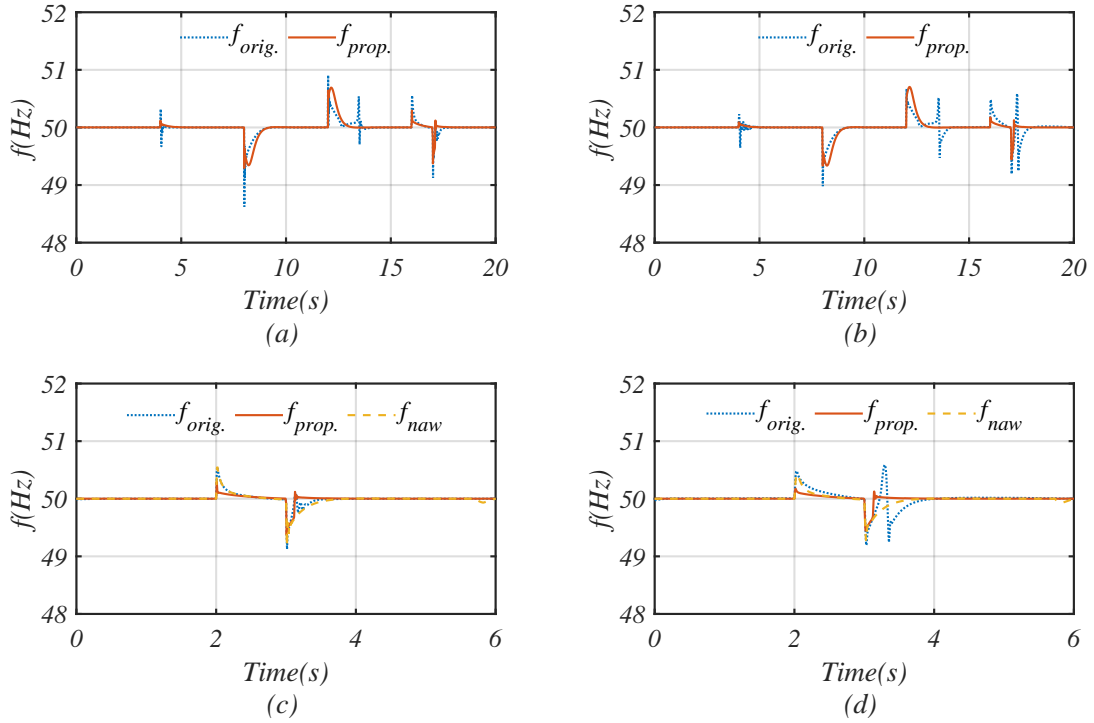


Figure 4.12: Frequency comparison of the original [116], with (orig.) and without (naw) anti-windup techniques, and the proposed controller in case of entire scenario (a) with $K_J = 10 \text{ kgm}^2$ (b) with $K_J = 50 \text{ kgm}^2$, and in case of a 40% balanced grid fault (c) with $K_J = 10 \text{ kgm}^2$ (d) with $K_J = 50 \text{ kgm}^2$, while $K_T = 4 \text{ Nm/V}^2$ and $K_D = 2500 \text{ Nms}$.

violation, while the proposed controller can ensure smooth transients and current limitation at all times as the ViSynC gains are chosen according to the stability conditions. Although increasing K_J can decrease the frequency fluctuation due to higher inertia provision as in Figure 4.12, it can have detrimental effects on the original controller performance as presented in the lower subfigures (e, f, g, h) in Figure 4.10, while the proposed controller can always guarantee smooth and safe operation.

Scenario II: This part focuses on the effect of severe grid voltage sags to the performance of the proposed method and original controller with and without anti-windup techniques when the ViSynC gains vary. The simulation starts with $600 \text{ W } P_s$ and $400 \text{ VAR } Q_{set}$. Then, at $t = 2 \text{ s}$, a short-circuit grid fault is applied and cleared at $t = 2.2 \text{ s}$. The simulation ends at $t = 6 \text{ s}$. Figure 4.11 depicts that the proposed approach shows better performance compared to the original controller, which is either equipped or not-equipped with the anti-windup techniques, by limiting the RMS inverter current at all times and guaranteeing a smooth and fast transient responses.

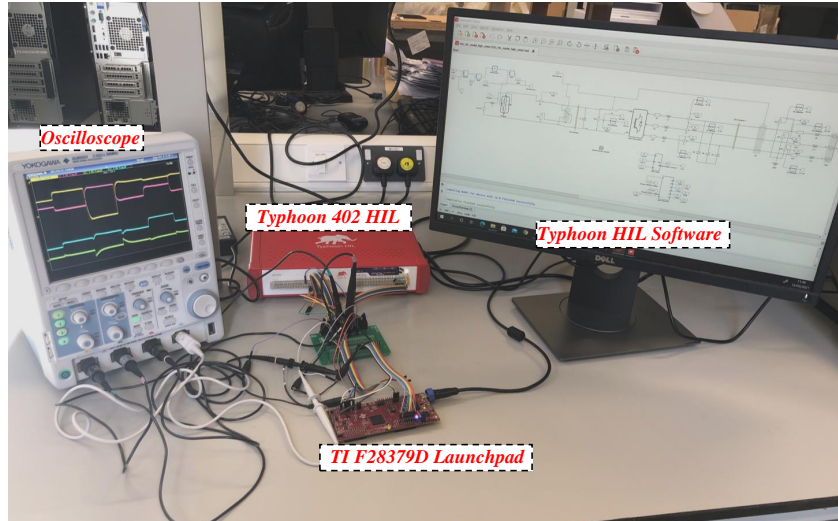


Figure 4.13: HIL experimental setup.

Moreover, Figure 4.12 illustrates the frequency damping ability of the proposed approach compared to the original controller. As can be understood from the frequency performances of both the entire case (Scenario I) in Figures 4.12 (a) and (b) and 40% balanced voltage sag case in Figures 4.12 (c) and (d), the proposed approach leads to lower amplitude frequency oscillations when the inertia gain (K_J) increases. To this end, the superior performance of the proposed method is verified for a number of cases with extensive simulation results compared to the existing methods.

4.2.4 Experimental studies

In this part, the effectiveness of the proposed method is examined and its advantages compared to the existing state-of-the-art current-limiting methods are demonstrated via hardware-in-the-loop studies.

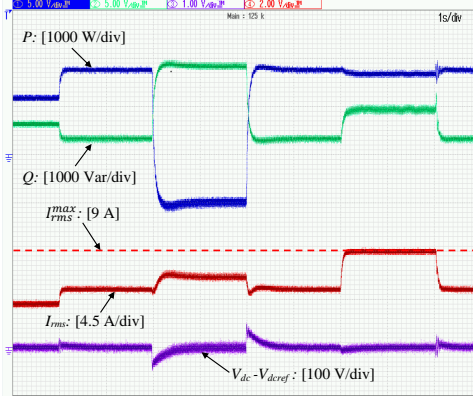
4.2.4.1 Hardware-in-the-loop (HIL) results

In order to verify the dynamic performance of the proposed controller and validate the theoretical stability analysis, a DER-sourced three-phase inverter connected to grid is designed using Typhoon-HIL 402 device and the control algorithms, as shown in Figure 4.3, are implemented in the TI F28379D launchpad. It is important to note that the hardware component is the controller and power system part is implemented in the Typhoon-HIL device as shown in Figure 4.13. Both the controller sampling and PWM switching frequencies are 20 kHz, while the remained system and controller parameters are provided in Table. 4.2. It should be emphasized here that in a real implementation

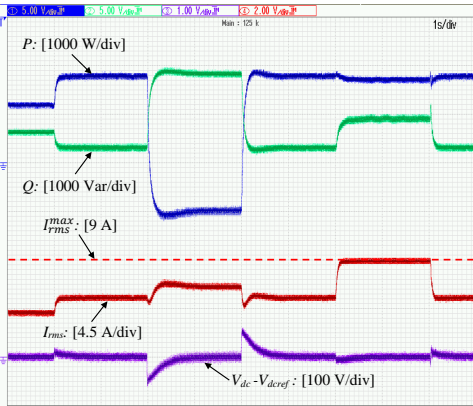
of the proposed controller, phase-lead low-pass filter can be added to the PCC voltage measurements to overcome small delay and noise issues caused by the inclusion of the feedforward terms in the control algorithm (see [162]).

The following scenario is carried out through HIL implementation. The operation starts with the values of 1200 W DER input power (P_s) and 1200 VAr reactive power reference (Q_{set}). At $t = 1s$, P_s is increased to 1800 W, which represents a demand rise in the grid side, at $t = 3s$, P_s is changed to -1000 W to test the bidirectional power transfer ability of the proposed method, and at $t = 5s$, P_s is recovered to 1800 W. In order to verify the integrator windup-free operation and current-limiting property under a considerable system fault, at $t = 7s$, a 40% balanced grid voltage sag is applied, and at $t = 9s$, the fault is cleared. The operation ends at $t = 10s$. Note that since the $Q \sim V$ droop is always enabled during the operation, reactive power is not regulated to exact Q_{set} values to support the grid voltage.

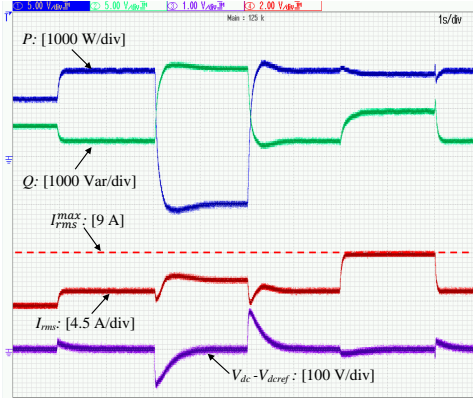
As can be seen in Figures 4.14 and 4.15, the proposed control scheme can rapidly regulate both the active and reactive power and limit the inverter RMS current without any controller saturation even after a grid voltage sag. In order to guide the prospective users about the ViSynC gain selections, Figure 4.14 illustrates the effect of various damping gain (K_D) values on the system behavior, while Figure 4.15 demonstrates the influence of inertia (K_J) and DC voltage tracking (K_T) gains on the dynamic system performance. The results are taken by considering constant $K_J = 10 \text{ kgm}^2$ and $K_T = 4 \text{ Nm/V}^2$ and variable K_D in Figure 4.14. Although increasing K_D can decrease the steady state system oscillations as shown in Figure 4.14a and 4.14b, it increases DC voltage (V_{dc}) fluctuation when the DER source demands power as in Figure 4.14c. Therefore, K_D is chosen as 3000 Nms while taking the results in Figure 4.15. Choosing large K_J values can cause surges in oscillation magnitudes as shown in Figure 4.15a and 4.15b, while selecting large K_T gain can lead to faster dynamic response. The transient performance of the proposed current-limiting method is illustrated through instantaneous inverter current and PCC voltage waveforms in Figure 4.16 when $P_s = 1800$ W. While Figure 4.16a shows that the inverter currents are limited during the grid fault appearance, Figure 4.16b also demonstrates that there is no current limit violation during the grid fault recovery. It is important to note that due to the four available channels in the oscilloscope, one phase PCC voltage (v_a) and three-phase inverter currents (i_a, i_b, i_c) are shown in Figure 4.16. However, since the balanced grid fault is applied, the other voltage phases follow the same voltage drop as phase a. In order to test the proposed controller performance under grid frequency (ω_g) changes, by selecting $K_T = 4 \text{ Nm/V}^2$, $K_J = 10 \text{ kgm}^2$, $K_D = 3000 \text{ Nms}$, and the frequency



(a) Time response of P , Q , I_{rms} and V_{dc} when $K_D = 2000$ Nms

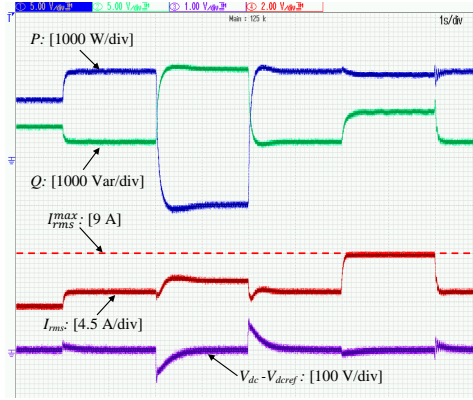


(b) Time response of P , Q , I_{rms} and V_{dc} when $K_D = 3000$ Nms

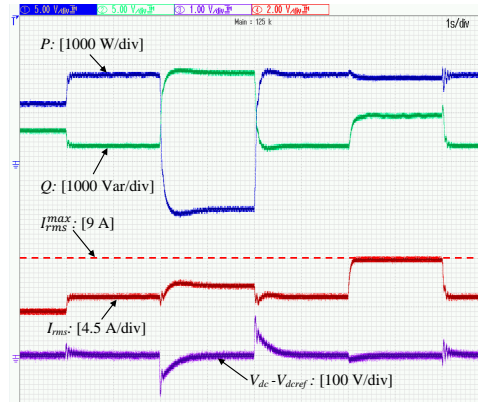


(c) Time response of P , Q , I_{rms} and V_{dc} when $K_D = 5000$ Nms

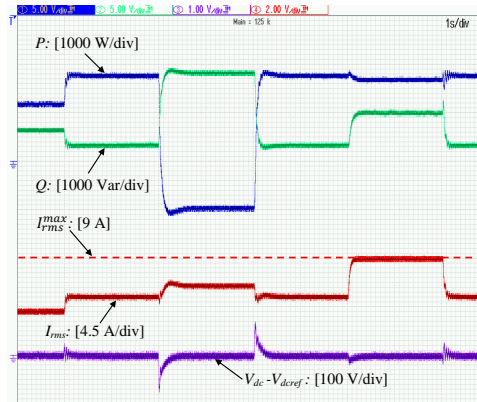
Figure 4.14: HIL results of a DER-sourced inverter under the proposed controller with different K_D gains.



(a) Time response of P , Q , I_{rms} and V_{dc} when $K_T = 4 \text{ Nm/V}^2$ and $K_J = 20 \text{ kgm}^2$

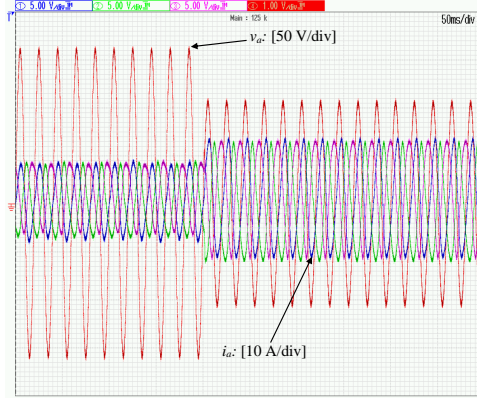


(b) Time response of P , Q , I_{rms} and V_{dc} when $K_T = 4 \text{ Nm/V}^2$ and $K_J = 50 \text{ kgm}^2$

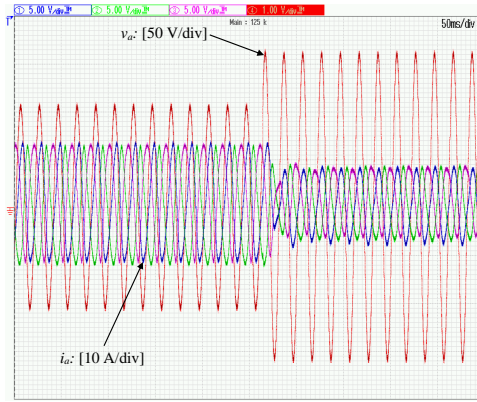


(c) Time response of P , Q , I_{rms} and V_{dc} when $K_T = 10 \text{ Nm/V}^2$ and $K_J = 30 \text{ kgm}^2$

Figure 4.15: HIL results of a DER-sourced inverter under the proposed controller with different K_J and K_T gains.



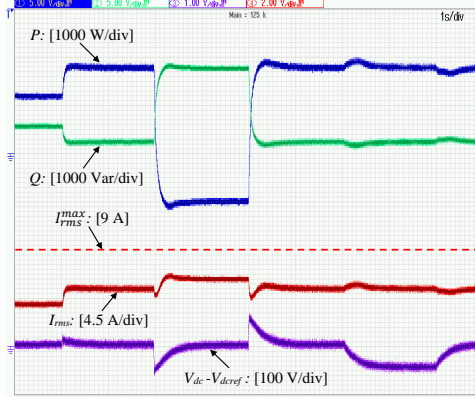
(a) Three-phase instantaneous inverter currents (i_{abc}) and PCC voltage (v_a) waveforms when the grid fault occurs



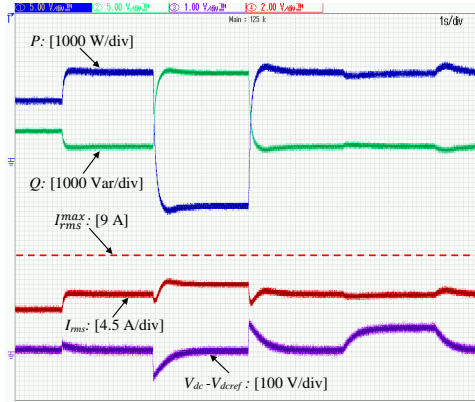
(b) Three-phase instantaneous inverter currents (i_{abc}) and PCC voltage (v_a) waveforms when the grid fault is cleared

Figure 4.16: HIL results of a DER-sourced inverter under the proposed controller in case of a balanced voltage sag (a) $110\text{ V} \rightarrow 70\text{ V}$ and recovery (b) $70\text{ V} \rightarrow 110\text{ V}$.

weighting coefficient $m = 0.1$ as explained in Chapter 2.2.5, an other HIL scenario is realised in Figure 4.17. By keeping the other changes same with the previous results, at $t = 7\text{ s}$, the grid frequency is decreased to 49 Hz in Figure 4.17a and increased to 51 Hz in Figure 4.17b, and at $t = 9\text{ s}$, the grid frequency comes back to its nominal value. Thus, it is justified that the proposed controller maintains the system stability and provides virtual inertia via $V_{dc} \sim \omega$ coupling as proven in the previous part. Furthermore, the boundary of ViSynC gain selection is verified to prove the validity of stability condition (4.32) in Figure 4.18. Figure 4.18a shows that the system becomes oscillatory in both transients and steady-state when the gains are chosen close to the stability boundary, while Figure 4.18b demonstrates that the system loses its stability



(a) Time response of P , Q , I_{rms} and V_{dc} in case of grid frequency drop



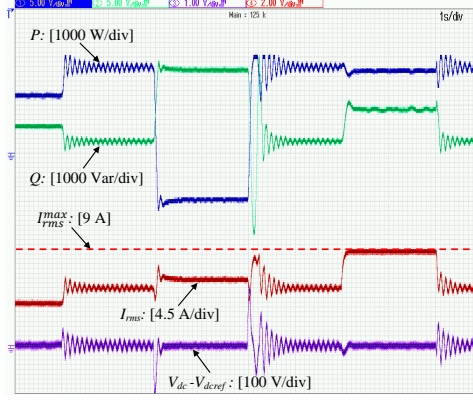
(b) Time response of P , Q , I_{rms} and V_{dc} in case of grid frequency swell

Figure 4.17: HIL results of a DER-sourced inverter under the proposed controller when the grid frequency (ω_g) changes.

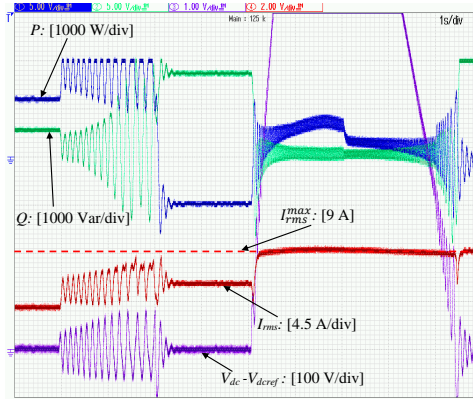
if the gains violate inequality (4.32). However, in both oscillatory and unstable cases, the proposed method limits the inverter current without the need of algorithm change and saturation blocks as seen in Figure 4.18. As a result, it is verified that the proposed approach can limit the RMS inverter current without any dependence on the ViSynC gains, and the selection of the ViSynC gains K_J , K_D and K_T in order to satisfy the stability condition (4.32) further supports the theoretic analysis presented in this work.

4.2.4.2 Comparison studies via HIL results

In this part, the superior features of the proposed method are emphasized by comparing it with two state-of-the-art current-limiting algorithms. The methods, which are used for comparison, are reference current saturation (RCS) [26] and d -axis priority based-



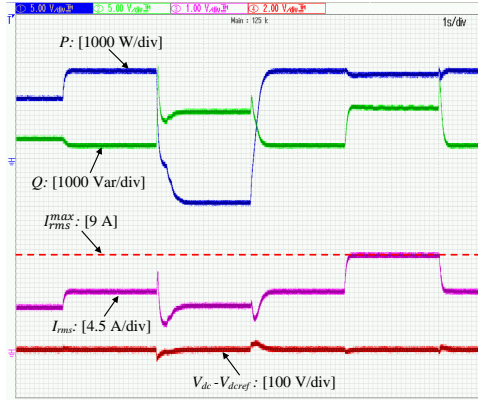
(a) Time response of P , Q , I_{rms} and V_{dc} when $K_D = 3000$ Nms, $K_J = 200$ kgm², and $K_T = 10$ Nm/V²



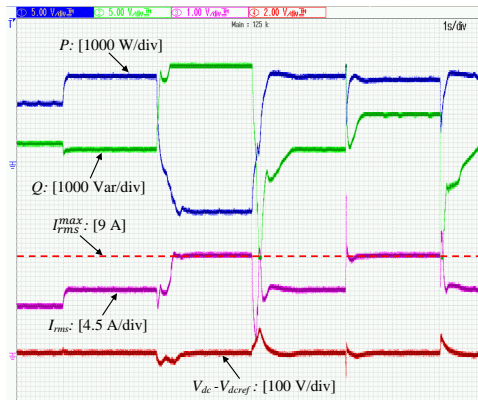
(b) Time response of P , Q , I_{rms} and V_{dc} when $K_D = 3000$ Nms, $K_J = 200$ kgm², and $K_T = 20$ Nm/V²

Figure 4.18: HIL results of a DER-sourced inverter under the proposed controller when the stability condition (4.32) is tested.

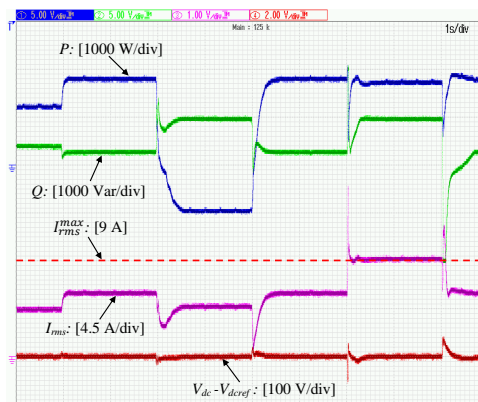
current saturation algorithm (CSA) [123] as explained in Chapter 2.3.1 in detail. The motivations for choosing RCS and d -axis priority based-CSA for comparison studies are; the former is the most commonly used current limitation method, and the latter is an emerging current limitation technique employed in virtual inertia applications. The system and controller parameters are provided in Table 4.2. The same system scenario with the Section 4.2.4.1 is implemented in this part. Even though the proposed method is stable for smaller damping gain (K_D), since the comparison methods need very high damping gain for stability, a larger damping gain ($K_D = 30000$ Nms) is used while taking the results for all three controllers. As shown in Figure 4.19, although all three methods maintain the stable operation of the system, only the proposed method can always guarantee the desired current-limiting property and damped system response, as shown in Figure 4.19a. Both the d -axis priority based-CSA and RCS violate the



(a) Time response of P , Q , I_{rms} and V_{dc} when the proposed controller is used



(b) Time response of P , Q , I_{rms} and V_{dc} when the d -axis priority based-current saturation algorithm in [123] is used



(c) Time response of P , Q , I_{rms} and V_{dc} when the reference current saturation method in [26] is used

Figure 4.19: HIL comparison results of a DER-sourced inverter under proposed and conventional current-limiting methods ([26] and [123]) when $K_D = 30000$ Nms, $K_J = 10$ kgm², and $K_T = 10$ Nm/V².

current limit (9 A), when the grid fault occurs and is cleared as can be seen in Figures 4.19b and 4.19c, respectively. Besides, when the P_s value is changed from positive to negative and from negative to positive, d -axis priority based-CSA method leads to an oscillatory response as illustrated in Figure 4.19b. Thus, it is verified that the proposed method can guarantee the current limitation and closed-loop system stability, when the gains are selected to satisfy (4.32), while the other methods fail to provide those properties throughout the entire operation.

4.3 Conclusions

In this Chapter, by considering the DC-link system dynamics, improved control techniques for grid-connected and RES-fed three-phase inverters were designed, rigorous stability analysis was realised, and extensive HIL results were provided to test the effectiveness of the proposed methods.

In the first section, an improved nonlinear controller is proposed for DER-sourced grid-connected VSCs. The proposed scheme uses DC-link voltage dynamics for inertia emulation and guarantees reliable operation under the balanced grid faults by limiting the inverter current. The current-limiting property is ensured via nonlinear control theory without using any saturation units or adaptive scheme for the first time for VI-based VSCs. Moreover, the entire system stability is investigated through small-signal analysis. The effectiveness of the proposed approach is verified with comprehensive simulation results. In the second section, the method proposed in the first section was further investigated and the closed-loop system stability has been rigorously proven using the singular perturbation theory, while analytic stability conditions, which guide the users for controller gain and reference power selections, were provided. The proposed method has been compared with the state-of-the-art current-limiting methods, and its superior features have been highlighted with extensive simulation studies. The stability conditions and dynamic performance of the proposed controller were also verified via comprehensive HIL results and compared to the existing techniques.

Chapter 5

Avoiding circulating current in AC microgrids

In order to provide higher-level power to both local loads and the utility grid, power electronic inverters (PEIs) are generally connected in parallel. Although the overload issue of inverter devices can be alleviated in parallel operations, circulating current or power problems can occur and lead to undesired circuit component heating, power inefficiency, and system instability, as mentioned in Chapter 2.3.2. Therefore, in this chapter, an AC microgrid consisting of paralleled three-phase inverters is investigated, and a nonlinear droop controller is proposed [196]. The purpose of the proposed controller is twofold: i) to avoid circulating power among the paralleled inverters and ii) to guarantee a current-limiting property at each inverter in both stand-alone and grid-connected modes, as well as during the transition between them. Contrary to the existing methods that utilize saturation blocks to limit the reference current value, the proposed controller limits the instantaneous value of the current even after extreme faults, i.e., short-circuits in both grid-connected and stand-alone cases. Moreover, after incorporating the proposed controller dynamics into the system, the entire microgrid small-signal stability analysis is investigated. In order to validate the effectiveness of the proposed controller, a microgrid, which includes three parallel three-phase inverters, is being tested via Matlab/Simulink software, and extensive simulation results are provided.

5.1 Background and motivations

Parallel operation of PEIs is preferred in microgrid applications, as the semiconductor components used in the PEIs have limited power ratings [197]. Although parallel

PEI operation has the advantage to avoid overloading individual inverters by achieving power and load sharing via droop control [11, 197], it can lead to undesired circulating power [126] and current [198] flows, especially in the GC to SA or SA to GC transitions and short-circuit faults, between different inverter units. Due to their simple logic and implementation, many droop control algorithms, such as virtual impedance-based droop, adaptive and robust droop [88], universal droop [93], and their improved versions [199, 200] have been proposed in the last decade. However, the droop method has an inherent inability to accurately share the load and power in parallel inverter applications in case of different line parameters without a control algorithm switch.

Ensuring the system stability in GC and SA operations and achieving smooth mode transitions are two critical issues for a reliable MG operation. In general, those issues can be achieved via various compensation methods, such as virtual impedance, droop coefficient, and control algorithm changes [201, 202]. However, the mentioned methods may lead to unacceptable voltage, frequency, and current fluctuations [203], which can damage the inverters, activate the protection relays, and eventually cause system instability.

In order to guarantee fail-safe operation and avoid transient instability phenomenon under large system faults, such as short-circuits, in RES or MG applications, every inverter in the system should be equipped with current-limiting algorithms [128, 130]. Besides, undesired circulating power between parallel inverters can lead to component overheating, reduced efficiency, instability [198], and DC-link voltage increase [125]. This issue is examined for SA mode parallel inverters in [198] via feeder impedance compensation and in [125] using proportional-derivative (PD) DC-link voltage controllers. Recently, a bounded integral controller (BIC) has been proposed and used to limit the system current of parallel inverters in SA mode [197]. However, GC operation and SA to GC or GC to SA transitions for parallel inverters have not been examined yet. Therefore, there is a need for a controller that can ensure the current-limiting property and prevent circulating power issues at the same time in parallel-connected DER operations. By integrating the universal droop control dynamics into the sl-PI controller and using a proportional DC-link controller, a simple method is proposed to achieve current limitation and maintain the DC-link voltage under the given limits at all times, including SA to GC and GC to SA transitions, and short-circuits in both SA and GC modes, in parallel three-phase inverter applications. Moreover, the small-signal stability of the entire closed-loop system equipped with the proposed controller is investigated. This process is explained step-by-step in the sequel.

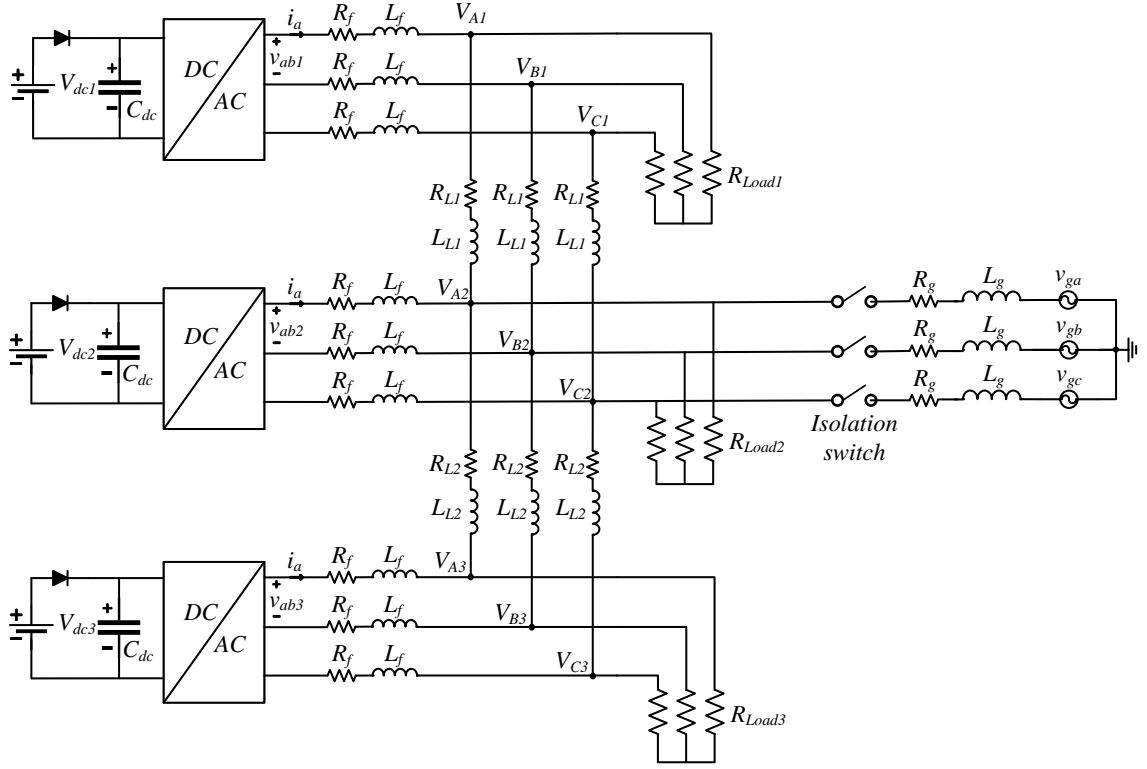


Figure 5.1: The microgrid system under consideration.

5.2 Microgrid modeling

The system under consideration is a microgrid, which includes three parallel three-phase inverters connected to individual loads and a point of common coupling (PCC) via L filters and lines, as depicted in Figure 5.1. The considered system topology is similar to [125], however, here, the grid-side is also regarded to examine the GC operation and transitions. The filter parasitic resistance and inductance are described as R_f and L_f , while the line inductances and resistances between the inverters are shown as L_{L1} , L_{L2} , R_{L1} , R_{L2} , respectively. Individual resistive loads for each inverter are denoted as R_{Load1} , R_{Load2} , and R_{Load3} . The line between the PCC and main grid has a resistance R_g and an inductance L_g , while grid-side abc frame voltages are denoted as v_{ga} , v_{gb} , and v_{gc} , respectively. The DC side of the inverters includes a DC-source, a diode, and a capacitor (C_{dc}) as adopted in [205]. Common frame inverter voltages are given as V_{Ai} , V_{Bi} , and V_{Ci} , where i denotes the inverter number. Following the analysis

from [204], the local frame inverter dq voltages are obtained as

$$\begin{bmatrix} V_{di} \\ V_{qi} \end{bmatrix} = \begin{bmatrix} V_{Di} \cos \delta_i + V_{Qi} \sin \delta_i \\ -V_{Di} \sin \delta_i + V_{Qi} \cos \delta_i \end{bmatrix}, \quad (5.1)$$

where $\delta_i = \theta_i - \theta_{com}$ denotes the phase angle difference between the inverter and common point. Then, the dynamic equations for each inverter in the local dq frame are given as

$$L_f \frac{di_{di}}{dt} = -R_f i_{di} + \omega_i L_f i_{qi} - V_{di} + V_{di} \quad (5.2)$$

$$L_f \frac{di_{qi}}{dt} = -R_f i_{qi} - \omega_i L_f i_{di} - V_{qi} + V_{qi} \quad (5.3)$$

where i_{di}, i_{qi} and V_{di}, V_{qi} represent the local dq frame inverter currents and voltages, while $\omega_i = \dot{\theta}_i$ is the angular frequency of the inverter. Hence, using (5.1) and local frame inverter currents, the inverter active and reactive power can be calculated as

$$\begin{aligned} P_i &= \frac{3}{2} [\cos \delta_i (V_{Di} i_{di} + V_{Qi} i_{qi}) + \sin \delta_i (V_{Qi} i_{di} - V_{Di} i_{qi})] \\ Q_i &= \frac{3}{2} [\cos \delta_i (V_{Qi} i_{di} - V_{Di} i_{qi}) - \sin \delta_i (V_{Di} i_{di} + V_{Qi} i_{qi})]. \end{aligned} \quad (5.4)$$

As can be seen from (5.4), the power equations include nonlinear terms. Therefore, any control effort including the widely accepted droop and PI controls will make the closed-loop system nonlinear. In that case, since the linear controllers may not guarantee the stable and reliable operation, especially under large system faults, i.e., short-circuits and transitions, nonlinear controllers should be designed. To this end, in the following part, a nonlinear controller is proposed to guarantee the current-limiting property for each inverter at all times, including the large system faults, while also preventing the circulating power via the DC-link voltage control.

Remark: Although the filter inductances and parasitic resistances of the inverters are given as equal in the system modelling, they can have different values in practice. In that case, only the numerical values in the Jacobian matrix will change. However, the current-limiting and circulating power prevention properties offered in this section will still hold for the microgrid.

5.3 The proposed current-limiting and DC-link controllers

In this part, the design steps for the proposed controller are explained in detail. With the application of universal droop control, the current-limiting property is achieved by embedding $P \sim V$ droop equations into the nonlinear sl-PI controller and the circulating power issue is resolved with the integration of proportional DC-link controller into the $Q \sim -\omega$ droop equations. Local inverter current is aligned with the d -axis for a simple implementation and closed-loop stability analysis as in [152], opposed to the common approaches [26], which align the inverter voltage with the d -axis. Thus, the inverter side local dq frame voltages (before the filter) are designed as control inputs and take the form

$$V_{di} = V_{dli} + E_{maxi} \sin \sigma_i - r_{vi} i_{di} - \omega_i L_f i_{qi} \quad (5.5)$$

$$V_{qi} = V_{qli} - r_{vi} i_{qi} + \omega_i L_f i_{di} \quad (5.6)$$

where E_{maxi} and r_{vi} are the sl-PI controller parameters and denoted as virtual voltage and resistor, respectively. $\omega_i L_f i_{di}$ and $\omega_i L_f i_{qi}$ represent the decoupling terms, and σ_i is the sl-PI controller state, which is designed to include $P \sim V$ droop dynamics as below

$$\dot{\sigma}_i = \frac{c_i}{E_{maxi}} \left[(\sqrt{2}E^* - V_{maxi}) - n_i(P_i - P_{seti}) \right] \cos \sigma_i \quad (5.7)$$

where c_i is the positive sl-PI controller gain. As proven in [181], if the initial condition of the controller state σ_i is selected as $\sigma_{i0} \in [-\frac{\pi}{2}, \frac{\pi}{2}]$, it is guaranteed that $\sigma_i(t) \in [-\frac{\pi}{2}, \frac{\pi}{2}] \forall t \geq 0$. Besides, contrary to traditional saturated PI controllers, the anti-windup property is inherently achieved with the proposed method, since the integration is decelerated near the maximum values, i.e., when $\sigma_i \rightarrow \pm \frac{\pi}{2}$, $\dot{\sigma}_i \rightarrow 0$.

Furthermore, the $P \sim V$ droop control is realised via regulating $(\sqrt{2}E^* - V_{maxi}) - n_i(P_i - P_{seti})$ to zero with the integration property of the sl-PI controller. In the droop expression, $\sqrt{2}E^*$ defines the nominal maximum common frame inverter voltage, V_{maxi} is the maximum common frame inverter voltage computed as $V_{maxi} = \sqrt{V_{Di}^2 + V_{Qi}^2}$, P_{seti} and n_i are the active power reference value and the active power droop coefficient, respectively.

The closed-loop system dynamics can be obtained by replacing the controller

dynamics (5.5)-(5.6) into the system dynamics (5.2)-(5.3) as below

$$L_f \frac{di_{di}}{dt} = -(R_f + r_{vi})i_{di} + E_{maxi} \sin \sigma_i \quad (5.8)$$

$$L_f \frac{di_{qi}}{dt} = -(R_f + r_{vi})i_{qi} \quad (5.9)$$

As one can understand from (5.9), if initially $i_{qi}(0) = 0$, then $i_{qi}(t) = 0, \forall t \geq 0$. Thus, the analytic solution of (5.9) is obtained as $i_{qi}(t) = i_{qi}(0)e^{-\frac{(R_f+r_{vi})}{L_f}t}$. To this end, in order to guarantee the inverter current limitation, the sl-PI controller parameters can be chosen as $E_{maxi} = (r_{vi} + R_f)I_{di}^{max}$, where $I_{di}^{max} = \sqrt{2}I_{rmsi}^{max}$ and I_{rmsi}^{max} is the RMS current limit provided by the inverter producers. Particularly, d -axis current i_{di} and the sl-PI controller state σ_i remain in the intervals $[-\sqrt{2}I_{rmsi}^{max}, \sqrt{2}I_{rmsi}^{max}]$ and $[-\frac{\pi}{2}, \frac{\pi}{2}] \forall t \geq 0$, respectively as proven in [151]. It is important to note that the current limitation is ensured for the original nonlinear system and independently of the large-signal system faults, including short-circuits and transitions. It is suggested that the readers refer to [181] for the controller state-limiting property proven via nonlinear control theory. Since it is proven that q -axis inverter current is always zero, the power expressions (5.4) can be simplified as

$$\begin{aligned} P_i &= \frac{3}{2} (V_{Di} \cos \delta_i + V_{Qi} \sin \delta_i) i_{di} \\ Q_i &= \frac{3}{2} (V_{Qi} \cos \delta_i - V_{Di} \sin \delta_i) i_{di}. \end{aligned} \quad (5.10)$$

The angular frequency dynamics, which are necessary for abc to dq transformations are designed to include $Q \sim -\omega$ and proportional DC-link controller as

$$\omega_i = \omega^* + m_i (Q_i - Q_{seti} - k_{pi}(V_{dci} - V_{dcref})) \quad (5.11)$$

where ω^* , m_i , Q_{seti} , k_{pi} , and V_{dcref} are the nominal angular frequency, reactive power droop coefficient, reactive power set value, DC-link proportional controller gain, and reference DC-link voltage, respectively.

5.4 Closed-loop small-signal stability analysis

Although the current-limiting property for the parallel-operated three-phase inverters is ensured in the previous part, the closed-loop stability of the entire system equipped with the proposed controller has not been investigated yet. Hence, here, the main focus

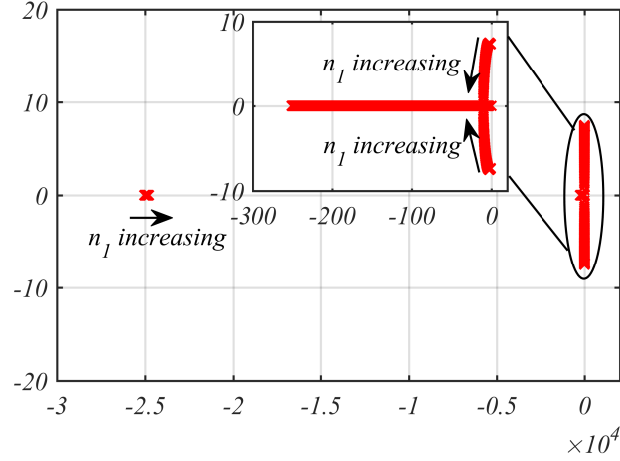


Figure 5.2: Closed-loop eigenvalue spectrum of inverter 1 as a function of active power droop coefficient $n_1 : \frac{0.01\sqrt{2}E^*}{S_{max}} \leq n_1 \leq \frac{0.3\sqrt{2}E^*}{S_{max}}$

Table 5.1: Simulated AC-MG system and controller parameters

Parameters	Values	Parameters	Values	Parameters	Values
P_{set1}	20kW	P_{set2}	10kW	P_{set3}	6.5kW
Q_{set1}	0VAR	Q_{set2}	0VAR	Q_{set3}	0VAR
R_{Load1}	25Ω	R_{Load2}	20Ω	R_{Load3}	38Ω
L_f	2mH	R_f	0.1Ω	n	0.00104
m	1.047×10^{-4}	E^*	220V	f^*	50Hz
V_{dcref}	750V	R_1	0.23Ω	L_1	0.32mH
R_2	0.35Ω	L_2	1.85mH	k_p	30
C_{dc}	1.1mF	m_L	6.5×10^{-4}	c	50000
ω^*	$2\pi f^*$	r_v	50Ω	I_d^{max}	67.276A
R_g	0.5Ω	L_g	2.2mH	S_{max}	30kVA

is to examine the stability of i number of parallel inverters. Since it is ensured with the controller design that the q -axis inverter current is zero at all times, (5.9) can be omitted from the closed-loop system analysis as it has been already investigated, separately. In order to provide a simple stability framework, the line and capacitor dynamics are ignored in this section. Considering (5.7)-(5.8), $\dot{\delta}_i = \omega_i - \omega_{com}$, and DC-link voltage dynamics in [205], the closed-loop state vector is constructed as $x_i = [i_{di} \ \sigma_i \ V_{dci} \ \delta_i]^T$. Root locus analysis can be realised for the entire system by calculating the equilibrium points using (5.7), (5.8), and (5.11) as $x_{ei} = [i_{dei} \ \sigma_{ei} \ V_{dcei} \ \delta_{ei}]^T$, where $\sigma_{ei} \in (-\frac{\pi}{2}, \frac{\pi}{2})$, and by linearizing (5.7)-(5.8) and (5.10)-(5.11) and considering constant (or piecewise constant) PCC voltage V_{maxi} . Thus, the closed-loop system Jacobian matrix can be computed as (5.12) for every inverter i . As a result, the asymptotic stability of the given equilibrium point of the closed-loop system will be guaranteed, if all system

eigenvalues are in left half plane.

$$J_i = \begin{bmatrix} -\frac{(r_{vi}+R_f)}{L_f} & \frac{E_{maxi} \cos \sigma_{ei}}{L_f} & 0 & 0 \\ -A_i B_i & 0 & 0 & -A_i C_i i_{dei} \\ \frac{3m_L}{C_{dc}} B_i & 0 & 0 & \frac{3m_L i_{dei}}{C_{dc}} C_i \\ \frac{3m_i}{2} C_i & 0 & -m_i k_p & -\frac{3m_i i_{dei}}{2} B_i \end{bmatrix}_{4i \times 4i} \quad (5.12)$$

where $A_i = \frac{3c_i n_i \cos \sigma_{ei}}{2E_{maxi}}$, $B_i = (V_{Di} \cos \delta_{ei} + V_{Qi} \sin \delta_{ei})$, $C_i = (V_{Qi} \cos \delta_{ei} - V_{Di} \sin \delta_{ei})$, and m_L is the V_{dc} linearization coefficient and can be calculated as $\frac{1}{2V_{dcref}}$ as explained in [205].

In Figure 5.2, the eigenvalue spectrum of closed-loop system for inverter 1 is demonstrated by changing the active power droop coefficient n_1 between 1% and 30%. The system and controller parameters used to plot the eigenvalue spectrum are given in Table 5.1. As it is clear from Figure 5.2, all eigenvalues are in left half plane. Similarly, one can test the eigenvalue spectrum of the other two inverters and realise that all eigenvalues are also located at the left half plane. Thus, the considered equilibrium point of the closed-loop system is asymptotically stable.

5.5 Simulation results

In order to test the proposed current-limiting controller performance, a microgrid, which has three parallel-connected three-phase inverters as in [125] and [204] is designed in the Matlab/Simulink software. Contrary to [125] and [204], which have examined only SA inverter operation and have not considered the current limitation issue, here, both the GC case and the SA to GC and GC to SA transitions are investigated. Simulated system and controller parameters are provided in Table 5.1. The simulation starts in SA case (isolation switch is open) and the system is quickly regulated to the steady-state values as shown in Figures 5.3 and 5.4 without any over-current problem as seen in Figures 5.5 and 5.6.

Between $t = 0.5s$ and $t = 0.6s$, 0.01Ω load is connected in parallel to R_{Load1} to test the SA case short-circuit performance of the proposed controller. Although there is a transient peak in the reactive powers (Figure 5.4), the frequencies (Figure 5.7), and the maximum voltages (Figure 5.9) at the fault recovery time instant, those do not affect the current-limiting property as illustrated in Figures 5.5 and 5.6. Even after a large fault, the system responds very quickly and almost immediately reaches to the steady-state. At $t = 1s$, isolation switch is closed and grid connection is realised. As

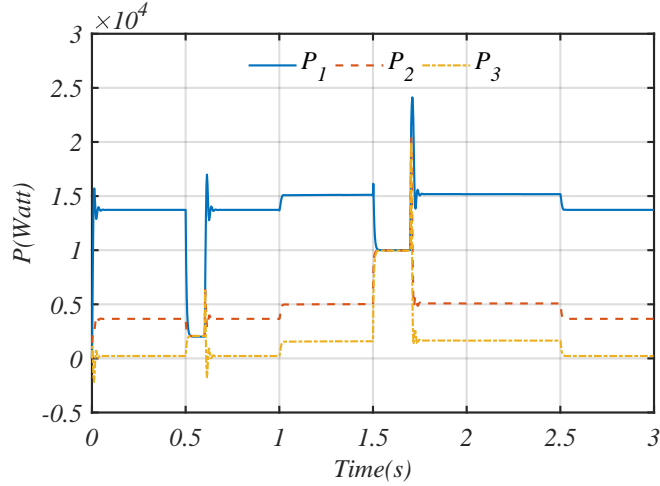


Figure 5.3: Active power outputs of three parallel-connected three-phase inverters

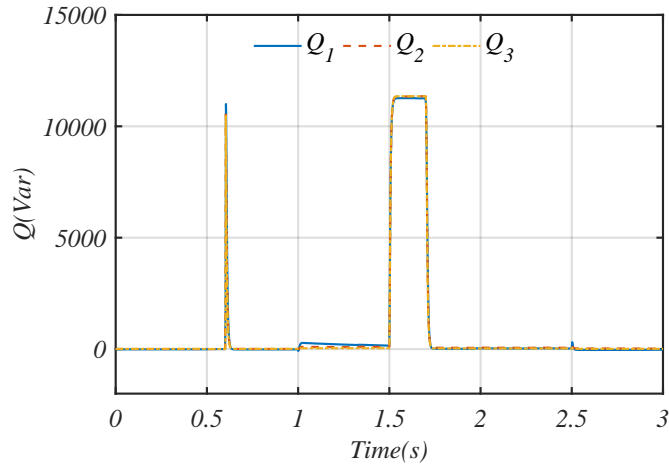


Figure 5.4: Reactive power outputs of three parallel-connected three-phase inverters

can be seen from Figures 5.6, 5.7, and 5.9, no current, frequency, and voltage overshoot is induced and connection is achieved very smoothly. Between $t = 1.5s$ and $t = 1.7s$, a grid short-circuit fault is applied to the system. Even in this extreme fault, the current-limiting property holds as shown in Figures 5.5 and 5.6. It is important to note that voltage peaks can appear during the transients of short-circuit faults in both SA and GC cases as shown in Figure 5.9. This issue should be considered if the application requires lower voltage peaks, and hardware or software filters can be used to avoid them. In that case, further stability analysis may be required to understand how the microgrid will be affected. Figure 5.6 justifies that the inverter current is aligned to d -axis ($i_{qi} = 0$) and this property is not influenced by the large system faults. DC voltage of the inverters is provided in Figure 5.8. The transient changes in the DC-link voltages

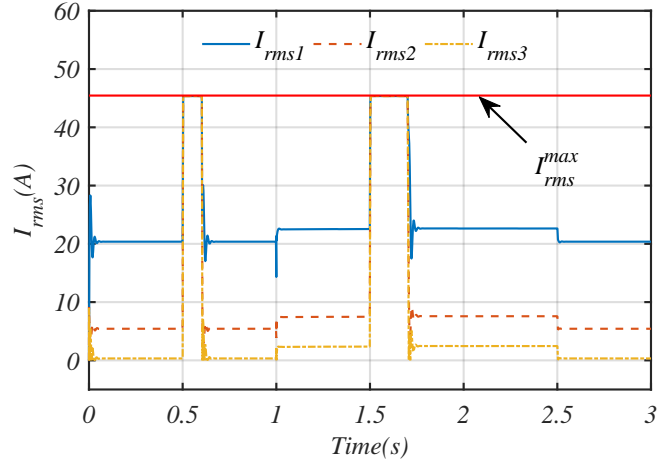


Figure 5.5: RMS currents of three parallel-connected three-phase inverters

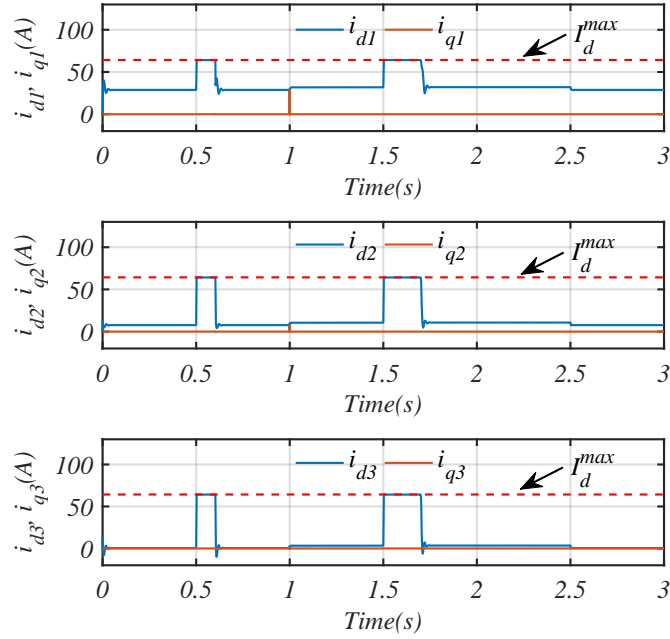


Figure 5.6: dq frame currents of three parallel-connected three-phase inverters

are also acceptable, since the circuit components can tolerate small overshoots. At $t = 2.5s$, GC to SA transition is conducted, and all figures support that the transition is achieved smoothly without any over-current or voltage encounters. At $t = 3s$, the simulation ends. If one wants to check the steady-state values of active powers and voltages according to the $P \sim V$ droop equation, zoomed maximum voltage in Figure 5.9 can be used as a reference. To this end, the effectiveness of proposed controller is demonstrated with extensive simulation studies under several different scenarios that include both normal and faulty conditions.

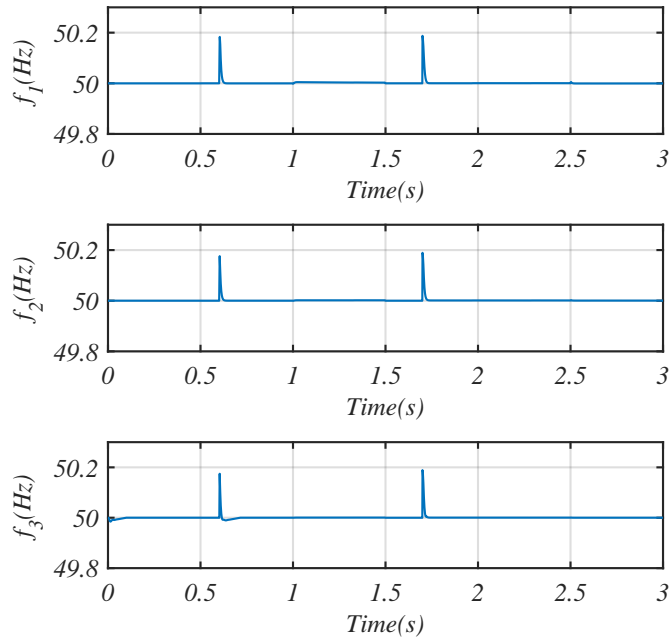


Figure 5.7: Frequencies of three parallel-connected three-phase inverters

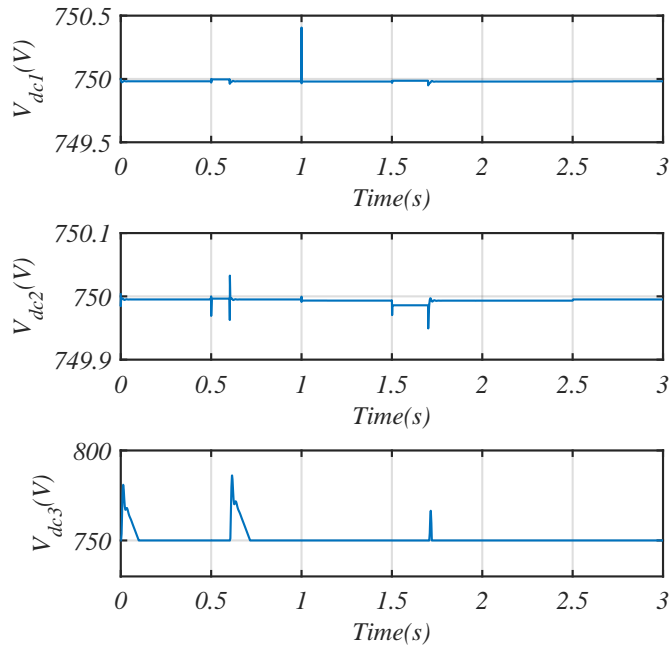


Figure 5.8: DC voltages of three parallel-connected three-phase inverters

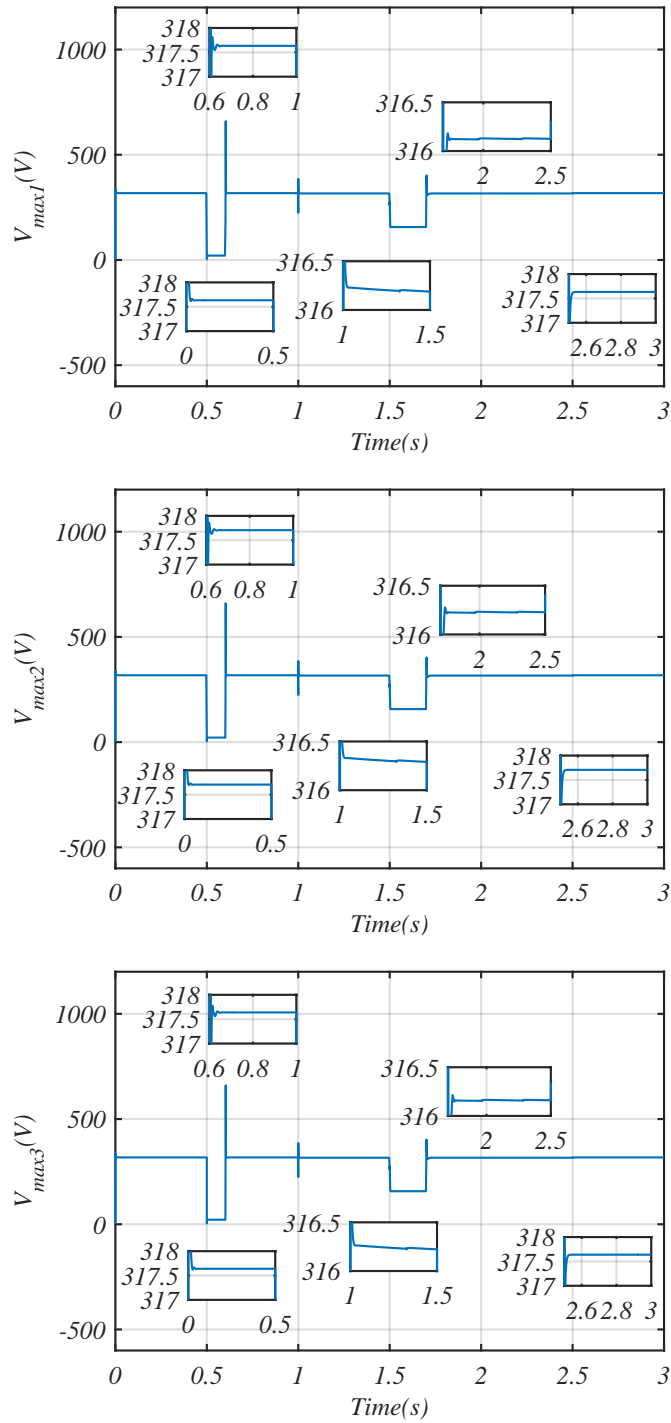


Figure 5.9: The maximum value of the PCC voltages of three parallel-connected three-phase inverters

5.6 Conclusions

In this Chapter, a nonlinear droop controller is proposed for parallel operated three-phase inverters. The proposed method can limit the inverter current via the sl-PI controller and prevent circulating power via DC-link voltage control at all times, including short-circuit in SA and GC cases, and transitions. The closed-loop stability is investigated using small-signal modeling and root locus analysis of the system has been demonstrated. The proposed controller performance is verified through extensive simulation results.

Chapter 6

Conclusions and future work

6.1 Conclusions

Since the main components of conventional grid systems, which are synchronous generators, are gradually being replaced by renewable energy resources, power balance, voltage and frequency stability, active and reactive power control should be ensured by the control algorithms of power converter devices to enable reliable and sustainable future power grid operations. Besides, power converters are semiconductor switch-based devices, and they should be protected against high currents and undesired circulating powers. Therefore, in this thesis, the main aim has been to propose advanced control techniques for three-phase inverter-based DER systems and microgrids by considering both grid-connected and islanded applications. The developed control schemes can guide the potential users in their power converter designs and therefore contribute to the renewable energy integration efforts.

In the design process of these advanced controllers, the recently proposed bounded integral control and state-limiting PI control concepts have been formulated to implement virtual synchronous control and droop controllers, such as traditional droop ($P \sim \omega/Q \sim V$) and inverse droop ($P \sim V/Q \sim -\omega$). The reason of employing different droop control techniques was to demonstrate that the proposed controllers can work independently of the output impedances of the power converters. Thus, the users can have the opportunity of choosing whichever droop relationship they need for their specific applications.

The proposed methods have been arranged to achieve accurate power control, current limitation, virtual inertia emulation, and circulating current prevention. The closed-loop stability of the three-phase inverter systems have been analytically examined and they have been verified via simulation and experimental studies under severe

system faults, such as voltage sags and short-circuits. Although various grid fault cases have been tested in validation studies, the stability analysis has been conducted assuming a stiff grid throughout the thesis. Furthermore, the applicability of inverter devices equipped with the proposed techniques to the modern power networks has been demonstrated considering up-to-date grid code requirements. In the following part, the main contributions offered in every chapter of this thesis have been outlined.

Chapter 3 was divided into three sections, and every section focused on designing advanced nonlinear controllers to solve specific issues in three-phase grid-connected inverters. In the first section, motivated by the bounded integral control concept, a nonlinear current-limiting droop controller for a three-phase inverter connected to the grid through an LCL filter was proposed. The controller design steps and analytic current-limiting proof were clearly explained. Active and reactive power regulation, droop control, and grid-side current limitation capabilities of the proposed controller were verified via extensive simulation results. In the second section, the main aim was to design a novel nonlinear PLL-less current-limiting controller for a three-phase grid-connected inverter employing bounded integral control concept. Considering the nonlinear dynamics of the system, the current-limiting property was proven for the inverter current using nonlinear control theory. Besides, the closed-loop system stability was investigated via small-signal analysis. The voltage and frequency support abilities of the proposed controller and its stability properties were validated via detailed simulation results. In the first two sections, although the system stability was examined at some level, analytic stability conditions were not provided, and experimental studies were not realised. Therefore, in the third section, using the state-limiting PI control structure, which introduces less controller state and leads to easier controller implementation, a novel nonlinear current-limiting droop controller for three-phase grid-connected inverters was proposed as an improvement to the method introduced in section two. The inverter RMS current was proven to be limited for the first time through a rigorous analysis based on invariant set theory without requiring saturation units. A detailed mathematical proof of the closed-loop asymptotic system stability was presented to provide useful guidance on the selection of the controller parameters for the control implementation. The superior features offered by the proposed controller compared to the existing current-limiting methods were emphasized via extensive comparison studies. The theoretical contributions and the effectiveness of the proposed control scheme were confirmed using an experimental setup under both normal and faulty grid conditions.

In Chapter 4, the DC-link voltage dynamics were integrated into the three-phase

inverter system to provide virtual inertia for power balance and stability improvement. This chapter was composed of two sections. In the first section, an improved nonlinear controller was proposed to guarantee reliable DER operation under the balanced grid faults both by limiting the inverter current and by considering the DC-link voltage dynamics for inertia emulation. The current-limiting property was ensured for the first time for virtual inertia integrated inverters. The system stability was investigated through small-signal analysis, and the effectiveness of the proposed approach was verified with extensive simulation results. However, rigorous closed-loop stability analysis and experimental results were not provided. Therefore, in the second section, the method introduced in the previous section was further investigated. The RMS current-limiting property was guaranteed during the entire operation, even under severe balanced voltage sags, independently from the controller and DC-link dynamics without the need for an algorithm change or saturation units. The closed-loop system stability was rigorously proven using the singular perturbation theory, while analytic stability conditions, which guide the potential users for controller gain, reference power, and system parameter selections, were provided. The proposed method has been compared with the state-of-the-art current-limiting methods, and its superior features have been highlighted with extensive simulation studies. The stability conditions and dynamic performance of the proposed controller were also verified via comprehensive HIL results and compared to the existing techniques.

In Chapter 5, a nonlinear droop controller was proposed for parallel-connected three-phase inverters. The proposed method can limit the inverter current via the state-limiting PI controller and prevent circulating power via DC-link voltage control at all times, including short-circuits in SA and GC cases and transitions. The closed-loop stability was examined using small-signal analysis, and the root locus of the system was provided. The proposed controller performance was verified through extensive simulation results.

6.2 Future work

Although several control algorithm related issues of three-phase grid-connected inverters and microgrids have been addressed, theoretically proven, and experimentally tested in this thesis, future studies can focus to further extend the proposed methods. In the following part, some suggestions for future research directions have been provided.

- The methods proposed in Chapter 3 have not considered the unbalanced grid fault cases, which can occur due to the various load characteristics in future

power networks. Therefore, it might be useful to investigate the unbalanced fault cases both theoretically and experimentally.

- While testing the methods offered in this thesis, the effect of the grid-side line has not been experimentally examined. Although the proposed controllers can ensure current-limiting property independently of the line parameters, current and voltage waveforms can be distorted due to line characteristics. In future studies, the lines with different short-circuit ratios can be considered, and their effect on system stability can be investigated.
- In Chapter 4, virtual synchronous control and state-limiting PI controller have been combined to provide virtual inertia and current limitation capabilities to the DER applications. In order to further explore the dynamic properties of state-limiting PI controller in VSG applications, it can be combined with other VSG methods, such as virtual oscillator control and virtual synchronous machines.
- In Chapter 5, the line and load dynamics have not been included in the stability analysis for simplicity. Besides, in the islanded case, only the resistive load was used, but in reality, complex loads, such as constant power loads, can exist. Therefore, in future studies, full system model can be considered with the line and complex load dynamics, and interesting stability conditions can be obtained. Finally, the proposed method can be experimentally tested for further validation.
- The dynamic properties of both bounded integral and state-limiting PI controllers can be further explored to employ them as synchronization algorithms in grid-connected applications.
- The methods proposed in this thesis focused only on the primary level of hierarchical control structure. Higher-level controllers with low bandwidth communication structures can be designed for optimal power transfer purposes.

Bibliography

- [1] Qing-Chang Zhong, "Introduction," *Power Electronics-Enabled Autonomous Power Systems: Next Generation Smart Grids*, IEEE, 2020, pp.1-10, doi: 10.1002/9781118803516.ch1.
- [2] J. Rifkin, *The Third Industrial Revolution: How Lateral Power Is Transforming Energy, the Economy, and the World*, Palgrave Macmillan, 2011.
- [3] Q. Xu, *Decentralized control and stability analysis for isolated microgrids*, PhD dissertation, Nanyang Technological University, Singapore, 2018.
- [4] D. K. Molzahn et al., "A Survey of Distributed Optimization and Control Algorithms for Electric Power Systems," *IEEE Transactions on Smart Grid*, vol. 8, no. 6, pp. 2941-2962, Nov. 2017, doi: 10.1109/TSG.2017.2720471.
- [5] F. Lamnabhi-Lagarrigue et al., "Systems & Control for the future of humanity, research agenda: Current and future roles, impact and grand challenges," *Annual Reviews in Control*, vol. 43, pp. 1–64, 2017, doi: 10.1016/j.arcontrol.2017.04.001.
- [6] H. Farhangi, "The path of the smart grid," *IEEE Power and Energy Magazine*, vol. 8, no. 1, pp. 18-28, January-February 2010, doi: 10.1109/MPE.2009.934876.
- [7] V. C. Gungor et al., "Smart Grid Technologies: Communication Technologies and Standards," *IEEE Transactions on Industrial Informatics*, vol. 7, no. 4, pp. 529-539, Nov. 2011, doi: 10.1109/TII.2011.2166794.
- [8] J. Rocabert, A. Luna, F. Blaabjerg and P. Rodríguez, "Control of Power Converters in AC Microgrids," *IEEE Transactions on Power Electronics*, vol. 27, no. 11, pp. 4734-4749, Nov. 2012, doi: 10.1109/TPEL.2012.2199334.
- [9] R. H. Lasseter, "MicroGrids," *2002 IEEE Power Engineering Society Winter Meeting. Conference Proceedings (Cat. No.02CH37309)*, 2002, pp. 305-308 vol.1, doi: 10.1109/PESW.2002.985003.

- [10] D. E. Olivares et al., "Trends in Microgrid Control," *IEEE Transactions on Smart Grid*, vol. 5, no. 4, pp. 1905-1919, July 2014, doi: 10.1109/TSG.2013.2295514.
- [11] M. Farrokhabadi et al., "Microgrid Stability Definitions, Analysis, and Examples," *IEEE Transactions on Power Systems*, vol. 35, no. 1, pp. 13-29, Jan. 2020, doi: 10.1109/TPWRS.2019.2925703.
- [12] L. Xiong, X. Liu, Y. Liu and F. Zhuo, "Modeling and stability issues of voltage-source converter dominated power systems: A review," *CSEE Journal of Power and Energy Systems*, doi: 10.17775/CSEEJPES.2020.03590.
- [13] J. M. Guerrero, M. Chandorkar, T. Lee and P. C. Loh, "Advanced Control Architectures for Intelligent Microgrids—Part I: Decentralized and Hierarchical Control," *IEEE Transactions on Industrial Electronics*, vol. 60, no. 4, pp. 1254-1262, April 2013, doi: 10.1109/TIE.2012.2194969.
- [14] H. Han, X. Hou, J. Yang, J. Wu, M. Su and J. M. Guerrero, "Review of Power Sharing Control Strategies for Islanding Operation of AC Microgrids," *IEEE Transactions on Smart Grid*, vol. 7, no. 1, pp. 200-215, Jan. 2016, doi: 10.1109/TSG.2015.2434849.
- [15] A. Vasilakis, I. Zafeiratou, D. T. Lagos and N. D. Hatziargyriou, "The Evolution of Research in Microgrids Control," *IEEE Open Access Journal of Power and Energy*, vol. 7, pp. 331-343, 2020, doi: 10.1109/OAJPE.2020.3030348.
- [16] Y. Han, H. Li, P. Shen, E. A. A. Coelho and J. M. Guerrero, "Review of Active and Reactive Power Sharing Strategies in Hierarchical Controlled Microgrids," *IEEE Transactions on Power Electronics*, vol. 32, no. 3, pp. 2427-2451, March 2017, doi: 10.1109/TPEL.2016.2569597.
- [17] A. Bidram and A. Davoudi, "Hierarchical Structure of Microgrids Control System," *IEEE Transactions on Smart Grid*, vol. 3, no. 4, pp. 1963-1976, Dec. 2012, doi: 10.1109/TSG.2012.2197425.
- [18] M. Chen and X. Xiao, "Hierarchical frequency control strategy of hybrid droop/VSG-based islanded microgrids," *Electric Power System Research*, vol. 155, pp. 131-143, 2018, doi: 10.1016/j.epsr.2017.10.011.
- [19] R. Ofir, U. Markovic, P. Aristidou and G. Hug, "Droop vs. virtual inertia: Comparison from the perspective of converter operation mode," *2018 IEEE Interna-*

- tional Energy Conference (ENERGYCON)*, 2018, pp. 1-6, doi: 10.1109/ENERGYCON.2018.8398752.
- [20] J. Fang, H. Li, Y. Tang and F. Blaabjerg, "On the Inertia of Future More-Electronics Power Systems," *IEEE Journal of Emerging and Selected Topics in Power Electronics*, vol. 7, no. 4, pp. 2130-2146, Dec. 2019, doi: 10.1109/JESTPE.2018.2877766.
- [21] K. S. Ratnam, K. Palanisamy, and G. Yang, "Future low-inertia power systems: Requirements, issues, and solutions - A review," *Renewable and Sustainable Energy Reviews*, vol. 124, no. February, 2020, doi: 10.1016/j.rser.2020.109773.
- [22] P. Unruh, M. Nuschke, P. Strauß, and F. Welck, "Overview on grid-forming inverter control methods," *Energies*, vol. 13, no. 10, 2020, doi: 10.3390/en13102589.
- [23] J. Schiffer, D. Zonetti, R. Ortega, A. M. Stanković, T. Sezi, and J. Raisch, "A survey on modeling of microgrids—From fundamental physics to phasors and voltage sources," *Automatica*, vol. 74, pp. 135–150, 2016, doi: 10.1016/j.automatica.2016.07.036.
- [24] A. Francés, R. Asensi, Ó. García, R. Prieto and J. Uceda, "Modeling Electronic Power Converters in Smart DC Microgrids—An Overview," *IEEE Transactions on Smart Grid*, vol. 9, no. 6, pp. 6274-6287, Nov. 2018, doi: 10.1109/TSG.2017.2707345.
- [25] R. Rosso, X. Wang, M. Liserre, X. Lu and S. Engelken, "Grid-Forming Converters: Control Approaches, Grid-Synchronization, and Future Trends—A Review," *IEEE Open Journal of Industry Applications*, vol. 2, pp. 93-109, 2021, doi: 10.1109/OJIA.2021.3074028.
- [26] N. Pogaku, M. Prodanovic and T. C. Green, "Modeling, Analysis and Testing of Autonomous Operation of an Inverter-Based Microgrid," *IEEE Transactions on Power Electronics*, vol. 22, no. 2, pp. 613-625, March 2007, doi: 10.1109/TPEL.2006.890003.
- [27] M. Rasheduzzaman, J. A. Mueller and J. W. Kimball, "An Accurate Small-Signal Model of Inverter- Dominated Islanded Microgrids Using dq Reference Frame," *IEEE Journal of Emerging and Selected Topics in Power Electronics*, vol. 2, no. 4, pp. 1070-1080, Dec. 2014, doi: 10.1109/JESTPE.2014.2338131.

- [28] H. J. Laaksonen, "Protection Principles for Future Microgrids," *IEEE Transactions on Power Electronics*, vol. 25, no. 12, pp. 2910-2918, Dec. 2010, doi: 10.1109/TPEL.2010.2066990.
- [29] P. T. Manditereza and R. Bansal, "Renewable distributed generation: The hidden challenges - A review from the protection perspective," *Renewable and Sustainable Energy Reviews*, vol. 58, pp. 1457–1465, 2016, doi: 10.1016/j.rser.2015.12.276.
- [30] A. Ipakchi and F. Albuyeh, "Grid of the future," *IEEE Power and Energy Magazine*, vol. 7, no. 2, pp. 52-62, March-April 2009, doi: 10.1109/MPE.2008.931384.
- [31] K. Moslehi and R. Kumar, "A Reliability Perspective of the Smart Grid," *IEEE Transactions on Smart Grid*, vol. 1, no. 1, pp. 57-64, June 2010, doi: 10.1109/TSG.2010.2046346.
- [32] F. Li et al., "Smart Transmission Grid: Vision and Framework," *IEEE Transactions on Smart Grid*, vol. 1, no. 2, pp. 168-177, Sept. 2010, doi: 10.1109/TSG.2010.2053726.
- [33] Q. Zhong, "Power-Electronics-Enabled Autonomous Power Systems: Architecture and Technical Routes," *IEEE Transactions on Industrial Electronics*, vol. 64, no. 7, pp. 5907-5918, July 2017, doi: 10.1109/TIE.2017.2677339.
- [34] X. Fang, S. Misra, G. Xue and D. Yang, "Smart Grid — The New and Improved Power Grid: A Survey," *IEEE Communications Surveys & Tutorials*, vol. 14, no. 4, pp. 944-980, Fourth Quarter 2012, doi: 10.1109/SURV.2011.101911.00087.
- [35] S. Massoud Amin and B. F. Wollenberg, "Toward a smart grid: power delivery for the 21st century," *IEEE Power and Energy Magazine*, vol. 3, no. 5, pp. 34-41, Sept.-Oct. 2005, doi: 10.1109/MPAE.2005.1507024.
- [36] F. Lamnabhi-Lagarrigue et al., "Systems & Control for the future of humanity, research agenda: Current and future roles, impact and grand challenges," *Annual Reviews in Control*, vol. 43, pp. 1–64, 2017, doi: 10.1016/j.arcontrol.2017.04.001.
- [37] B. Kroposki et al., "Achieving a 100% Renewable Grid: Operating Electric Power Systems with Extremely High Levels of Variable Renewable Energy," *IEEE Power and Energy Magazine*, vol. 15, no. 2, pp. 61-73, March-April 2017, doi: 10.1109/MPE.2016.2637122.

- [38] G. T. Heydt, "The Next Generation of Power Distribution Systems," *IEEE Transactions on Smart Grid*, vol. 1, no. 3, pp. 225-235, Dec. 2010, doi: 10.1109/TSG.2010.2080328.
- [39] M. Liserre, T. Sauter and J. Y. Hung, "Future Energy Systems: Integrating Renewable Energy Sources into the Smart Power Grid Through Industrial Electronics," *IEEE Industrial Electronics Magazine*, vol. 4, no. 1, pp. 18-37, March 2010, doi: 10.1109/MIE.2010.935861.
- [40] A. Q. Huang, "Power Semiconductor Devices for Smart Grid and Renewable Energy Systems," *Proceedings of the IEEE*, vol. 105, no. 11, pp. 2019-2047, Nov. 2017, doi: 10.1109/JPROC.2017.2687701.
- [41] Y. Yan, Y. Qian, H. Sharif and D. Tipper, "A Survey on Smart Grid Communication Infrastructures: Motivations, Requirements and Challenges," *IEEE Communications Surveys & Tutorials*, vol. 15, no. 1, pp. 5-20, First Quarter 2013, doi: 10.1109/SURV.2012.021312.00034.
- [42] Y. Khayat et al., "On the Secondary Control Architectures of AC Microgrids: An Overview," *IEEE Transactions on Power Electronics*, vol. 35, no. 6, pp. 6482-6500, June 2020, doi: 10.1109/TPEL.2019.2951694.
- [43] J. M. Guerrero, J. C. Vasquez, J. Matas, L. G. de Vicuna and M. Castilla, "Hierarchical Control of Droop-Controlled AC and DC Microgrids—A General Approach Toward Standardization," *IEEE Transactions on Industrial Electronics*, vol. 58, no. 1, pp. 158-172, Jan. 2011, doi: 10.1109/TIE.2010.2066534.
- [44] W. Feng et al., "A review of microgrid development in the United States – A decade of progress on policies, demonstrations, controls, and software tools," *Applied Energy*, vol. 228, no. June, pp. 1656–1668, 2018, doi: 10.1016/j.apenergy.2018.06.096.
- [45] C. Cecati, C. Citro and P. Siano, "Combined Operations of Renewable Energy Systems and Responsive Demand in a Smart Grid," *IEEE Transactions on Sustainable Energy*, vol. 2, no. 4, pp. 468-476, Oct. 2011, doi: 10.1109/TSTE.2011.2161624.
- [46] A. M. Bouzid, J. M. Guerrero, A. Cheriti, M. Bouhamida, P. Sicard, and M. Benghanem, "A survey on control of electric power distributed generation systems for microgrid applications," *Renewable and Sustainable Energy Reviews*, vol. 44, pp. 751–766, 2015, doi: 10.1016/j.rser.2015.01.016.

- [47] A. Gupta, S. Doolla and K. Chatterjee, "Hybrid AC–DC Microgrid: Systematic Evaluation of Control Strategies," *IEEE Transactions on Smart Grid*, vol. 9, no. 4, pp. 3830–3843, July 2018, doi: 10.1109/TSG.2017.2727344.
- [48] R. Zamora and A. K. Srivastava, "Controls for microgrids with storage: Review, challenges, and research needs," *Renewable and Sustainable Energy Reviews*, vol. 14, no. 7, pp. 2009–2018, 2010, doi: 10.1016/j.rser.2010.03.019.
- [49] A. Hirsch, Y. Parag, and J. Guerrero, "Microgrids: A review of technologies, key drivers, and outstanding issues," *Renewable and Sustainable Energy Reviews*, vol. 90, no. September 2017, pp. 402–411, 2018, doi: 10.1016/j.rser.2018.03.040.
- [50] W. Feng et al., "A review of microgrid development in the United States – A decade of progress on policies, demonstrations, controls, and software tools," *Applied Energy*, vol. 228, no. June, pp. 1656–1668, 2018, doi: 10.1016/j.apenergy.2018.06.096.
- [51] E. Planas, J. Andreu, J. I. Gárate, I. Martínez De Alegría, and E. Ibarra, "AC and DC technology in microgrids: A review," *Renewable and Sustainable Energy Reviews*, vol. 43, pp. 726–749, 2015, doi: 10.1016/j.rser.2014.11.067.
- [52] Qing-Chang Zhong; Tomas Hornik, "Introduction," *Control of Power Inverters in Renewable Energy and Smart Grid Integration*, IEEE, 2012, pp.1-61, doi: 10.1002/9781118481806.ch1.
- [53] M. Forouzesh, Y. P. Siwakoti, S. A. Gorji, F. Blaabjerg and B. Lehman, "Step-Up DC–DC Converters: A Comprehensive Review of Voltage-Boosting Techniques, Topologies, and Applications," *IEEE Transactions on Power Electronics*, vol. 32, no. 12, pp. 9143–9178, Dec. 2017, doi: 10.1109/TPEL.2017.2652318.
- [54] A. Francés, R. Asensi, Ó. García, R. Prieto and J. Uceda, "Modeling Electronic Power Converters in Smart DC Microgrids—An Overview," *IEEE Transactions on Smart Grid*, vol. 9, no. 6, pp. 6274–6287, Nov. 2018, doi: 10.1109/TSG.2017.2707345.
- [55] J. C. Vasquez, J. M. Guerrero, M. Savaghebi, J. Eloy-Garcia and R. Teodorescu, "Modeling, Analysis, and Design of Stationary-Reference-Frame Droop-Controlled Parallel Three-Phase Voltage Source Inverters," *IEEE Transactions on Industrial Electronics*, vol. 60, no. 4, pp. 1271–1280, April 2013, doi: 10.1109/TIE.2012.2194951.

- [56] M. Karimi-Ghartemani, "Universal Integrated Synchronization and Control for Single-Phase DC/AC Converters," *IEEE Transactions on Power Electronics*, vol. 30, no. 3, pp. 1544-1557, March 2015, doi: 10.1109/TPEL.2014.2304459.
- [57] M. Kabalan, P. Singh and D. Niebur, "Nonlinear Lyapunov Stability Analysis of Seven Models of a DC/AC Droop Controlled Inverter Connected to an Infinite Bus," *IEEE Transactions on Smart Grid*, vol. 10, no. 1, pp. 772-781, Jan. 2019, doi: 10.1109/TSG.2017.2752146.
- [58] N. Mohan, T. M. Undeland, and W. P. Robbins, "*Power Electronics - Converters, Applications and Design*," 3rd ed. John Wiley & Sons, 2002.
- [59] Q. Xu, N. Vafamand, L. Chen, T. Dragičević, L. Xie and F. Blaabjerg, "Review on Advanced Control Technologies for Bidirectional DC/DC Converters in DC Microgrids," *IEEE Journal of Emerging and Selected Topics in Power Electronics*, vol. 9, no. 2, pp. 1205-1221, April 2021, doi: 10.1109/JESTPE.2020.2978064.
- [60] T. Dragičević, X. Lu, J. C. Vasquez and J. M. Guerrero, "DC Microgrids—Part I: A Review of Control Strategies and Stabilization Techniques," *IEEE Transactions on Power Electronics*, vol. 31, no. 7, pp. 4876-4891, July 2016, doi: 10.1109/TPEL.2015.2478859.
- [61] H. Athari, M. Niroomand, and M. Ataei, "Review and Classification of Control Systems in Grid-tied Inverters," *Renewable and Sustainable Energy Reviews*, vol. 72, no. September 2016, pp. 1167–1176, 2017, doi: 10.1016/j.rser.2016.10.030.
- [62] Q. Zhong and G. Weiss, "Synchronverters: Inverters That Mimic Synchronous Generators," *IEEE Transactions on Industrial Electronics*, vol. 58, no. 4, pp. 1259-1267, April 2011, doi: 10.1109/TIE.2010.2048839.
- [63] X. Lu, J. Wang, J. M. Guerrero and D. Zhao, "Virtual-Impedance-Based Fault Current Limiters for Inverter Dominated AC Microgrids," in *IEEE Transactions on Smart Grid*, vol. 9, no. 3, pp. 1599-1612, May 2018, doi: 10.1109/TSG.2016.2594811.
- [64] C. Bao, X. Ruan, X. Wang, W. Li, D. Pan and K. Weng, "Step-by-Step Controller Design for LCL-Type Grid-Connected Inverter with Capacitor–Current-Feedback Active-Damping," *IEEE Transactions on Power Electronics*, vol. 29, no. 3, pp. 1239-1253, March 2014, doi: 10.1109/TPEL.2013.2262378.

- [65] M. A. Hossain, H. R. Pota, W. Issa, and M. J. Hossain, "Overview of AC microgrid controls with inverter-interfaced generations," *Energies*, vol. 10, no. 9, pp. 1–27, 2017, doi: 10.3390/en10091300.
- [66] K. Zeb et al., "A comprehensive review on inverter topologies and control strategies for grid connected photovoltaic system," *Renewable and Sustainable Energy Reviews*, vol. 94, no. June, pp. 1120–1141, 2018, doi: 10.1016/j.rser.2018.06.053.
- [67] T. Dragičević, S. Vazquez and P. Wheeler, "Advanced Control Methods for Power Converters in DG Systems and Microgrids," *IEEE Transactions on Industrial Electronics*, vol. 68, no. 7, pp. 5847–5862, July 2021, doi: 10.1109/TIE.2020.2994857.
- [68] R. H. Lasseter, Z. Chen and D. Pattabiraman, "Grid-Forming Inverters: A Critical Asset for the Power Grid," *IEEE Journal of Emerging and Selected Topics in Power Electronics*, vol. 8, no. 2, pp. 925–935, June 2020, doi: 10.1109/JESTPE.2019.2959271.
- [69] E. Planas, A. Gil-De-Muro, J. Andreu, I. Kortabarria, and I. Martínez De Alegría, "General aspects, hierarchical controls and droop methods in microgrids: A review," *Renewable and Sustainable Energy Reviews*, vol. 17, pp. 147–159, 2013, doi: 10.1016/j.rser.2012.09.032.
- [70] E. Unamuno and J. A. Barrena, "Hybrid ac/dc microgrids — Part II : Review and classification of control strategies," *Renewable and Sustainable Energy Reviews*, vol. 52, pp. 1123–1134, 2015.
- [71] Y. A. I. Mohamed and A. A. Radwan, "Hierarchical Control System for Robust Microgrid Operation and Seamless Mode Transfer in Active Distribution Systems," *IEEE Transactions on Smart Grid*, vol. 2, no. 2, pp. 352–362, June 2011, doi: 10.1109/TSG.2011.2136362.
- [72] X. Lu, J. M. Guerrero, K. Sun, J. C. Vasquez, R. Teodorescu and L. Huang, "Hierarchical Control of Parallel AC-DC Converter Interfaces for Hybrid Microgrids," *IEEE Transactions on Smart Grid*, vol. 5, no. 2, pp. 683–692, March 2014, doi: 10.1109/TSG.2013.2272327.
- [73] B. K. Poolla, D. Groß and F. Dörfler, "Placement and Implementation of Grid-Forming and Grid-Following Virtual Inertia and Fast Frequency Response," *IEEE Transactions on Power Systems*, vol. 34, no. 4, pp. 3035–3046, July 2019, doi: 10.1109/TPWRS.2019.2892290.

- [74] K. Shi, H. Ye, W. Song and G. Zhou, "Virtual Inertia Control Strategy in Microgrid Based on Virtual Synchronous Generator Technology," *IEEE Access*, vol. 6, pp. 27949-27957, 2018, doi: 10.1109/ACCESS.2018.2839737.
- [75] J. Kim, S. H. Lee and J. Park, "Inertia-Free Stand-Alone Microgrid—Part II: Inertia Control for Stabilizing DC-Link Capacitor Voltage of PMSG Wind Turbine System," *IEEE Transactions on Industry Applications*, vol. 54, no. 5, pp. 4060-4068, Sept.-Oct. 2018, doi: 10.1109/TIA.2018.2840083.
- [76] X. Luo et al., "Review of voltage and frequency grid code specifications for electrical energy storage applications," *Energies*, vol. 11, no. 5, 2018, doi: 10.3390/en11051070.
- [77] E. M. G. Rodrigues, G. J. Osório, R. Godina, A. W. Bizuayehu, J. M. Lujano-Rojas, and J. P. S. Catalão, "Grid code reinforcements for deeper renewable generation in insular energy systems," *Renewable and Sustainable Energy Reviews*, vol. 53, pp. 163–177, 2016, doi: 10.1016/j.rser.2015.08.047.
- [78] X. He, H. Geng, R. Li and B. C. Pal, "Transient Stability Analysis and Enhancement of Renewable Energy Conversion System During LVRT," *IEEE Transactions on Sustainable Energy*, vol. 11, no. 3, pp. 1612-1623, July 2020, doi: 10.1109/TSTE.2019.2932613.
- [79] S. Yazdani, M. Ferdowsi, M. Davari and P. Shamsi, "Advanced Current-Limiting and Power-Sharing Control in a PV-Based Grid-Forming Inverter Under Unbalanced Grid Conditions," *IEEE Journal of Emerging and Selected Topics in Power Electronics*, vol. 8, no. 2, pp. 1084-1096, June 2020, doi: 10.1109/JESTPE.2019.2959006.
- [80] L. Xiong et al., "Static Synchronous Generator Model: A New Perspective to Investigate Dynamic Characteristics and Stability Issues of Grid-Tied PWM Inverter," *IEEE Transactions on Power Electronics*, vol. 31, no. 9, pp. 6264-6280, Sept. 2016, doi: 10.1109/TPEL.2015.2498933.
- [81] F. Milano, F. Dörfler, G. Hug, D. J. Hill and G. Verbič, "Foundations and Challenges of Low-Inertia Systems (Invited Paper)," *2018 Power Systems Computation Conference (PSCC)*, 2018, pp. 1-25, doi: 10.23919/PSCC.2018.8450880.

- [82] U. Tamrakar, D. Shrestha, M. Maharjan, B. Bhattarai, T. Hansen, and R. Tonkoski, "Virtual Inertia: Current Trends and Future Directions," *Applied Sciences*, vol. 7, no. 7, p. 654, 2017, doi: 10.3390/app7070654.
- [83] T. Ackermann, T. Prevost, V. Vittal, A. J. Roscoe, J. Matevosyan and N. Miller, "Paving the Way: A Future Without Inertia Is Closer Than You Think," *IEEE Power and Energy Magazine*, vol. 15, no. 6, pp. 61-69, Nov.-Dec. 2017, doi: 10.1109/MPE.2017.2729138.
- [84] Qing-Chang Zhong, "Synchronized and Democratized (SYNDEM) Smart Grid," *Power Electronics-Enabled Autonomous Power Systems: Next Generation Smart Grids*, IEEE, 2020, pp.11-34, doi: 10.1002/9781118803516.ch2.
- [85] Q. Zhong, Y. Wang and B. Ren, "Connecting the Home Grid to the Public Grid: Field Demonstration of Virtual Synchronous Machines," *IEEE Power Electronics Magazine*, vol. 6, no. 4, pp. 41-49, Dec. 2019, doi:10.1109/MPEL.2019.2946700.
- [86] T. V. Van et al., "Virtual synchronous generator: An element of future grids," *2010 IEEE PES Innovative Smart Grid Technologies Conference Europe (ISGT Europe)*, 2010, pp. 1-7, doi: 10.1109/ISGTEUROPE.2010.5638946.
- [87] K. Y. Yap, C. R. Sarimuthu, and J. M. Y. Lim, "Virtual inertia-based inverters for mitigating frequency instability in grid-connected renewable energy system: A Review," *Applied Sciences*, vol. 9, no. 24, 2019, doi: 10.3390/app9245300.
- [88] U. B. Tayab, M. A. Bin Roslan, L. J. Hwai, and M. Kashif, "A review of droop control techniques for microgrid," *Renewable and Sustainable Energy Reviews*, vol. 76, no. November 2016, pp. 717–727, 2017, doi: 10.1016/j.rser.2017.03.028.
- [89] S. D'Arco and J. A. Suul, "Virtual synchronous machines — Classification of implementations and analysis of equivalence to droop controllers for microgrids," *2013 IEEE Grenoble Conference*, 2013, pp. 1-7, doi: 10.1109/PTC.2013.6652456.
- [90] D. Chen, Y. Xu and A. Q. Huang, "Integration of DC Microgrids as Virtual Synchronous Machines Into the AC Grid," *IEEE Transactions on Industrial Electronics*, vol. 64, no. 9, pp. 7455-7466, Sept. 2017, doi: 10.1109/TIE.2017.2674621.
- [91] J. W. Simpson-Porco, F. Dörfler, and F. Bullo, "Synchronization and power sharing for droop-controlled inverters in islanded microgrids," *Automatica*, vol. 49, no. 9, pp. 2603–2611, 2013, doi: 10.1016/j.automatica.2013.05.018.

- [92] Q. Zhong, "Robust Droop Controller for Accurate Proportional Load Sharing Among Inverters Operated in Parallel," *IEEE Transactions on Industrial Electronics*, vol. 60, no. 4, pp. 1281-1290, April 2013, doi: 10.1109/TIE.2011.2146221.
- [93] Q. Zhong and Y. Zeng, "Universal Droop Control of Inverters with Different Types of Output Impedance," *IEEE Access*, vol. 4, pp. 702-712, 2016, doi: 10.1109/ACCESS.2016.2526616.
- [94] Qing-Chang Zhong; Tomas Hornik, "Parallel Operation of Inverters," *Control of Power Inverters in Renewable Energy and Smart Grid Integration*, IEEE, 2012, pp.297-333, doi: 10.1002/9781118481806.ch19.
- [95] Y. Gui, X. Wang and F. Blaabjerg, "Vector Current Control Derived from Direct Power Control for Grid-Connected Inverters," *IEEE Transactions on Power Electronics*, vol. 34, no. 9, pp. 9224-9235, Sept. 2019, doi: 10.1109/TPEL.2018.2883507.
- [96] Q. Zhong and D. Boroyevich, "A droop controller is intrinsically a phase-locked loop," *IECON 2013 - 39th Annual Conference of the IEEE Industrial Electronics Society*, 2013, pp. 5916-5921, doi: 10.1109/IECON.2013.6700105.
- [97] Jia Liu, Y. Miura and T. Ise, "Dynamic characteristics and stability comparisons between virtual synchronous generator and droop control in inverter-based distributed generators," *2014 International Power Electronics Conference (IPEC-Hiroshima 2014 - ECCE ASIA)*, 2014, pp. 1536-1543, doi: 10.1109/IPEC.2014.6869789.
- [98] J. Kim, J. M. Guerrero, P. Rodriguez, R. Teodorescu and K. Nam, "Mode Adaptive Droop Control with Virtual Output Impedances for an Inverter-Based Flexible AC Microgrid," *IEEE Transactions on Power Electronics*, vol. 26, no. 3, pp. 689-701, March 2011, doi: 10.1109/TPEL.2010.2091685.
- [99] J. He and Y. W. Li, "Analysis, Design, and Implementation of Virtual Impedance for Power Electronics Interfaced Distributed Generation," *IEEE Transactions on Industry Applications*, vol. 47, no. 6, pp. 2525-2538, Nov.-Dec. 2011, doi: 10.1109/TIA.2011.2168592.
- [100] H. Beck and R. Hesse, "Virtual synchronous machine," *2007 9th International Conference on Electrical Power Quality and Utilisation*, 2007, pp. 1-6, doi: 10.1109/EPQU.2007.4424220.

- [101] O. Mo, S. D'Arco and J. A. Suul, "Evaluation of Virtual Synchronous Machines with Dynamic or Quasi-Stationary Machine Models," *IEEE Transactions on Industrial Electronics*, vol. 64, no. 7, pp. 5952-5962, July 2017, doi: 10.1109/TIE.2016.2638810.
- [102] S. Khan, B. Bletterie, A. Anta, and W. Gawlik, "On small signal frequency stability under virtual inertia and the role of PLLs," *Energies*, vol. 11, no. 9, pp. 1–18, 2018, doi: 10.3390/en11092372.
- [103] H. Miao, F. Mei, Y. Yang, H. Chen, and J. Zheng, "A comprehensive VSM control strategy designed for unbalanced grids," *Energies*, vol. 12, no. 6, 2019, doi: 10.3390/en12061169.
- [104] Q. Zhong, "Virtual Synchronous Machines: A unified interface for grid integration," *IEEE Power Electronics Magazine*, vol. 3, no. 4, pp. 18-27, Dec. 2016, doi: 10.1109/MPEL.2016.2614906.
- [105] S. Shinnaka, "A Robust Single-Phase PLL System with Stable and Fast Tracking," *IEEE Transactions on Industry Applications*, vol. 44, no. 2, pp. 624-633, March-april 2008, doi: 10.1109/TIA.2008.916750.
- [106] L. Zhang, L. Harnefors and H. Nee, "Power-Synchronization Control of Grid-Connected Voltage-Source Converters," *IEEE Transactions on Power Systems*, vol. 25, no. 2, pp. 809-820, May 2010, doi: 10.1109/TPWRS.2009.2032231.
- [107] Q. Zhong, P. Nguyen, Z. Ma and W. Sheng, "Self-Synchronized Synchronverters: Inverters Without a Dedicated Synchronization Unit," *IEEE Transactions on Power Electronics*, vol. 29, no. 2, pp. 617-630, Feb. 2014, doi: 10.1109/TPEL.2013.2258684.
- [108] Q. C. Zhong, "Synchronized and Democratized Smart Grids To Underpin The Third Industrial Revolution," *IFAC-Papers OnLine*, vol. 50, no. 1, pp. 3592–3597, 2017, doi: 10.1016/j.ifacol.2017.08.699.
- [109] Q. -C. Zhong, G. C. Konstantopoulos, B. Ren and M. Krstic, "Improved Synchronverters with Bounded Frequency and Voltage for Smart Grid Integration," in *IEEE Transactions on Smart Grid*, vol. 9, no. 2, pp. 786-796, March 2018, doi: 10.1109/TSG.2016.2565663.

- [110] B. B. Johnson, S. V. Dhople, A. O. Hamadeh and P. T. Krein, "Synchronization of Parallel Single-Phase Inverters with Virtual Oscillator Control," *IEEE Transactions on Power Electronics*, vol. 29, no. 11, pp. 6124-6138, Nov. 2014, doi: 10.1109/TPEL.2013.2296292.
- [111] B. B. Johnson, S. V. Dhople, J. L. Cale, A. O. Hamadeh and P. T. Krein, "Oscillator-Based Inverter Control for Islanded Three-Phase Microgrids," *IEEE Journal of Photovoltaics*, vol. 4, no. 1, pp. 387-395, Jan. 2014, doi: 10.1109/JPHOTOV.2013.2280953.
- [112] D. Raisz, T. T. Thai and A. Monti, "Power Control of Virtual Oscillator Controlled Inverters in Grid-Connected Mode," *IEEE Transactions on Power Electronics*, vol. 34, no. 6, pp. 5916-5926, June 2019, doi: 10.1109/TPEL.2018.2868996.
- [113] M. Sinha, F. Dörfler, B. B. Johnson and S. V. Dhople, "Uncovering Droop Control Laws Embedded Within the Nonlinear Dynamics of Van der Pol Oscillators," *IEEE Transactions on Control of Network Systems*, vol. 4, no. 2, pp. 347-358, June 2017, doi: 10.1109/TCNS.2015.2503558.
- [114] Z. Shi, J. Li, H. I. Nurdin and J. E. Fletcher, "Comparison of Virtual Oscillator and Droop Controlled Islanded Three-Phase Microgrids," *IEEE Transactions on Energy Conversion*, vol. 34, no. 4, pp. 1769-1780, Dec. 2019, doi: 10.1109/TEC.2019.2922447.
- [115] B. B. Johnson, M. Sinha, N. G. Ainsworth, F. Dörfler and S. V. Dhople, "Synthesizing Virtual Oscillators to Control Islanded Inverters," *IEEE Transactions on Power Electronics*, vol. 31, no. 8, pp. 6002-6015, Aug. 2016, doi: 10.1109/TPEL.2015.2497217.
- [116] L. Huang et al., "A Virtual Synchronous Control for Voltage-Source Converters Utilizing Dynamics of DC-Link Capacitor to Realize Self-Synchronization," *IEEE Journal of Emerging and Selected Topics in Power Electronics*, vol. 5, no. 4, pp. 1565-1577, Dec. 2017, doi: 10.1109/JESTPE.2017.2740424.
- [117] C. Arghir and F. Dörfler, "The Electronic Realization of Synchronous Machines: Model Matching, Angle Tracking, and Energy Shaping Techniques," *IEEE Transactions on Power Electronics*, vol. 35, no. 4, pp. 4398-4410, April 2020, doi: 10.1109/TPEL.2019.2939710.

- [118] Z. Shuai, W. Huang, C. Shen, J. Ge and Z. J. Shen, "Characteristics and Restraining Method of Fast Transient Inrush Fault Currents in Synchronverters," *IEEE Transactions on Industrial Electronics*, vol. 64, no. 9, pp. 7487-7497, Sept. 2017, doi: 10.1109/TIE.2017.2652362.
- [119] T. L. Vandoorn, B. Meersman, L. Degroote, B. Renders and L. Vandeveldel, "A Control Strategy for Islanded Microgrids with DC-Link Voltage Control," *IEEE Transactions on Power Delivery*, vol. 26, no. 2, pp. 703-713, April 2011, doi: 10.1109/TPWRD.2010.2095044.
- [120] J. Jongudomkarn, J. Liu and T. Ise, "Virtual Synchronous Generator Control with Reliable Fault Ride-Through Ability: A Solution Based on Finite-Set Model Predictive Control," *IEEE Journal of Emerging and Selected Topics in Power Electronics*, vol. 8, no. 4, pp. 3811-3824, Dec. 2020, doi: 10.1109/JESTPE.2019.2942943.
- [121] B. Wei, J. M. Guerrero, J. C. Vásquez and X. Guo, "A Circulating-Current Suppression Method for Parallel-Connected Voltage-Source Inverters with Common DC and AC Buses," *IEEE Transactions on Industry Applications*, vol. 53, no. 4, pp. 3758-3769, July-Aug. 2017, doi: 10.1109/TIA.2017.2681620.
- [122] Z. Xueguang, C. Jiaming, M. Yan, W. Yijie and X. Dianguo, "Bandwidth Expansion Method for Circulating Current Control in Parallel Three-phase PWM Converter Connection System," *IEEE Transactions on Power Electronics*, vol. 29, no. 12, pp. 6847-6856, Dec. 2014, doi: 10.1109/TPEL.2014.2311046.
- [123] T. Qoria, F. Gruson, F. Colas, X. Kestelyn, and X. Guillaud, "Current limiting algorithms and transient stability analysis of grid-forming VSCs," *Electric Power System Research*, vol. 189, no. 691800, 2020, doi: 10.1016/j.epsr.2020.106726.
- [124] N. Bottrell and T. C. Green, "Comparison of Current-Limiting Strategies During Fault Ride-Through of Inverters to Prevent Latch-Up and Wind-Up," *IEEE Transactions on Power Electronics*, vol. 29, no. 7, pp. 3786-3797, July 2014, doi: 10.1109/TPEL.2013.2279162.
- [125] W. Issa, F. Al-Naemi, G. Konstantopoulos, S. Sharkh, and M. Abusara, "Stability analysis and control of a microgrid against circulating power between parallel inverters," *Energy Procedia*, vol. 157, pp. 1061-1070, 2019, doi: 10.1016/j.egypro.2018.11.273.

- [126] W. R. Issa, A. H. E. Khateb, M. A. Abusara and T. K. Mallick, "Control Strategy for Uninterrupted Microgrid Mode Transfer During Unintentional Islanding Scenarios," *IEEE Transactions on Industrial Electronics*, vol. 65, no. 6, pp. 4831-4839, June 2018, doi: 10.1109/TIE.2017.2772199.
- [127] A. Gkountaras, "Modeling Techniques and Control Strategies for Inverter Dominated Microgrids," PhD dissertation, Universitätsverlag der TU Berlin, Germany, 2017.
- [128] A. D. Paquette and D. M. Divan, "Virtual Impedance Current Limiting for Inverters in Microgrids with Synchronous Generators," *IEEE Transactions on Industry Applications*, vol. 51, no. 2, pp. 1630-1638, March-April 2015, doi: 10.1109/TIA.2014.2345877.
- [129] H. Xin, L. Huang, L. Zhang, Z. Wang and J. Hu, "Synchronous Instability Mechanism of P-f Droop-Controlled Voltage Source Converter Caused by Current Saturation," *IEEE Transactions on Power Systems*, vol. 31, no. 6, pp. 5206-5207, Nov. 2016, doi: 10.1109/TPWRS.2016.2521325.
- [130] L. Huang, H. Xin, Z. Wang, L. Zhang, K. Wu and J. Hu, "Transient Stability Analysis and Control Design of Droop-Controlled Voltage Source Converters Considering Current Limitation," *IEEE Transactions on Smart Grid*, vol. 10, no. 1, pp. 578-591, Jan. 2019, doi: 10.1109/TSG.2017.2749259.
- [131] J. He and Y. W. Li, "An Enhanced Microgrid Load Demand Sharing Strategy," *IEEE Transactions on Power Electronics*, vol. 27, no. 9, pp. 3984-3995, Sept. 2012, doi: 10.1109/TPEL.2012.2190099.
- [132] P. Li, X. Wang, W. Lee and D. Xu, "Dynamic Power Conditioning Method of Microgrid Via Adaptive Inverse Control," *IEEE Transactions on Power Delivery*, vol. 30, no. 2, pp. 906-913, April 2015, doi: 10.1109/TPWRD.2014.2323083.
- [133] J. M. Guerrero, Luis Garcia de Vicuna, J. Matas, M. Castilla and J. Miret, "Output impedance design of parallel-connected UPS inverters with wireless load-sharing control," *IEEE Transactions on Industrial Electronics*, vol. 52, no. 4, pp. 1126-1135, Aug. 2005, doi: 10.1109/TIE.2005.851634.
- [134] H. Yuan, X. Yuan and J. Hu, "Modeling of Grid-Connected VSCs for Power System Small-Signal Stability Analysis in DC-Link Voltage Control Timescale,"

- IEEE Transactions on Power Systems*, vol. 32, no. 5, pp. 3981-3991, Sept. 2017, doi: 10.1109/TPWRS.2017.2653939.
- [135] M. Kabalan, P. Singh and D. Niebur, "Large Signal Lyapunov-Based Stability Studies in Microgrids: A Review," *IEEE Transactions on Smart Grid*, vol. 8, no. 5, pp. 2287-2295, Sept. 2017, doi: 10.1109/TSG.2016.2521652.
- [136] J. Fang, H. Li, Y. Tang and F. Blaabjerg, "Distributed Power System Virtual Inertia Implemented by Grid-Connected Power Converters," *IEEE Transactions on Power Electronics*, vol. 33, no. 10, pp. 8488-8499, Oct. 2018, doi: 10.1109/TPEL.2017.2785218.
- [137] S. Liyanage, Y. Wang, Y. Dong and B. Ren, "Sustainable, Portable, and Efficient Electricity Delivery (SPEED): Design, Control, and Testing," *IEEE Access*, vol. 8, pp. 73082-73095, 2020, doi: 10.1109/ACCESS.2020.2987556.
- [138] J. M. Guerrero et al., "Distributed Generation: Toward a New Energy Paradigm," *IEEE Industrial Electronics Magazine*, vol. 4, no. 1, pp. 52-64, March 2010, doi: 10.1109/MIE.2010.935862.
- [139] M. S. Kim, R. Haider, G. J. Cho, C. H. Kim, C. Y. Won, and J. S. Chai, "Comprehensive review of islanding detection methods for distributed generation systems," *Energies*, vol. 12, no. 5, pp. 1–21, 2019, doi: 10.3390/en12050837.
- [140] F. Katiraei, R. Iravani, N. Hatziargyriou and A. Dimeas, "Microgrids management," *IEEE Power and Energy Magazine*, vol. 6, no. 3, pp. 54-65, May-June 2008, doi: 10.1109/MPE.2008.918702.
- [141] R. Majumder, "Some Aspects of Stability in Microgrids," *IEEE Transactions on Power Systems*, vol. 28, no. 3, pp. 3243-3252, Aug. 2013, doi: 10.1109/TPWRS.2012.2234146.
- [142] J. Fang, P. Lin, H. Li, Y. Yang and Y. Tang, "An Improved Virtual Inertia Control for Three-Phase Voltage Source Converters Connected to a Weak Grid," *IEEE Transactions on Power Electronics*, vol. 34, no. 9, pp. 8660-8670, Sept. 2019, doi: 10.1109/TPEL.2018.2885513.
- [143] S. M. Tayebi, H. Hu and I. Batarseh, "Advanced DC-Link Voltage Regulation and Capacitor Optimization for Three-Phase Microinverters," *IEEE Transactions on Industrial Electronics*, vol. 66, no. 1, pp. 307-317, Jan. 2019, doi: 10.1109/TIE.2018.2823700.

- [144] Y. Huang, X. Zhai, J. Hu, D. Liu and C. Lin, "Modeling and Stability Analysis of VSC Internal Voltage in DC-Link Voltage Control Timescale," *IEEE Journal of Emerging and Selected Topics in Power Electronics*, vol. 6, no. 1, pp. 16-28, March 2018, doi: 10.1109/JESTPE.2017.2715224.
- [145] S. D'Arco, J. A. Suul and O. B. Fosso, "Control system tuning and stability analysis of Virtual Synchronous Machines," *2013 IEEE Energy Conversion Congress and Exposition*, 2013, pp. 2664-2671, doi: 10.1109/ECCE.2013.6647045.
- [146] X. Wang and F. Blaabjerg, "Harmonic Stability in Power Electronic-Based Power Systems: Concept, Modeling, and Analysis," *IEEE Transactions on Smart Grid*, vol. 10, no. 3, pp. 2858-2870, May 2019, doi: 10.1109/TSG.2018.2812712.
- [147] Y. Gui, X. Wang, H. Wu and F. Blaabjerg, "Voltage-Modulated Direct Power Control for a Weak Grid-Connected Voltage Source Inverters," *IEEE Transactions on Power Electronics*, vol. 34, no. 11, pp. 11383-11395, Nov. 2019, doi: 10.1109/TPEL.2019.2898268.
- [148] M. A. Awal and I. Husain, "Unified Virtual Oscillator Control for Grid-Forming and Grid-Following Converters," *IEEE Journal of Emerging and Selected Topics in Power Electronics*, vol. 9, no. 4, pp. 4573-4586, Aug. 2021, doi: 10.1109/JESTPE.2020.3025748.
- [149] Y. Wang, B. Ren and Q. -C. Zhong, "Bounded UDE-Based Controller for Input Constrained Systems with Uncertainties and Disturbances," *IEEE Transactions on Industrial Electronics*, vol. 68, no. 2, pp. 1560-1570, Feb. 2021, doi: 10.1109/TIE.2020.2969069.
- [150] S. Dedeoglu and G. C. Konstantopoulos, "Three-Phase Grid-Connected Inverters Equipped with Nonlinear Current-Limiting Control," *2018 UKACC 12th International Conference on Control (CONTROL)*, 2018, pp. 38-43, doi: 10.1109/CONTROL.2018.8516764.
- [151] S. Dedeoglu and G. C. Konstantopoulos, "PLL-Less Three-Phase Droop-Controlled Inverter with Inherent Current-Limiting Property," *IECON 2019 - 45th Annual Conference of the IEEE Industrial Electronics Society*, 2019, pp. 4013-4018, doi: 10.1109/IECON.2019.8927219.
- [152] S. Dedeoglu, G. C. Konstantopoulos and A. G. Paspatis, "Grid-Supporting Three-Phase Inverters with Inherent Root Mean Square Current Limitation Under Bal-

- anced Grid Voltage Sags," *IEEE Transactions on Industrial Electronics*, vol. 68, no. 11, pp. 11379-11389, Nov. 2021, doi: 10.1109/TIE.2020.3034860.
- [153] J. M. Carrasco et al., "Power-Electronic Systems for the Grid Integration of Renewable Energy Sources: A Survey," *IEEE Transactions on Industrial Electronics*, vol. 53, no. 4, pp. 1002-1016, June 2006, doi: 10.1109/TIE.2006.878356.
- [154] "The grid code," *National Grid Electricity Transmission PLC*, London, U.K., Tech. Rep., Dec. 2010.
- [155] J. M. Guerrero, J. Matas, L. Garcia de Vicuna, M. Castilla and J. Miret, "Decentralized Control for Parallel Operation of Distributed Generation Inverters Using Resistive Output Impedance," *IEEE Transactions on Industrial Electronics*, vol. 54, no. 2, pp. 994-1004, April 2007, doi: 10.1109/TIE.2007.892621.
- [156] X. Tang, W. Deng and Z. Qi, "Investigation of the Dynamic Stability of Microgrid," *IEEE Transactions on Power Systems*, vol. 29, no. 2, pp. 698-706, March 2014, doi: 10.1109/TPWRS.2013.2285585.
- [157] R. Majumder, B. Chaudhuri, A. Ghosh, R. Majumder, G. Ledwich and F. Zare, "Improvement of Stability and Load Sharing in an Autonomous Microgrid Using Supplementary Droop Control Loop," *IEEE Transactions on Power Systems*, vol. 25, no. 2, pp. 796-808, May 2010, doi: 10.1109/TPWRS.2009.2032049.
- [158] Y. A. I. Mohamed and E. F. El-Saadany, "Adaptive Decentralized Droop Controller to Preserve Power Sharing Stability of Paralleled Inverters in Distributed Generation Microgrids," *IEEE Transactions on Power Electronics*, vol. 23, no. 6, pp. 2806-2816, Nov. 2008, doi: 10.1109/TPEL.2008.2005100.
- [159] E. Lenz, D. J. Pagano and J. Pou, "Bifurcation Analysis of Parallel-Connected Voltage-Source Inverters with Constant Power Loads," *IEEE Transactions on Smart Grid*, vol. 9, no. 6, pp. 5482-5493, Nov. 2018, doi: 10.1109/TSG.2017.2668381.
- [160] L. Zaccarian and A. R. Teel, "Nonlinear scheduled anti-windup design for linear systems," *IEEE Transactions on Automatic Control*, vol. 49, no. 11, pp. 2055-2061, Nov. 2004, doi: 10.1109/TAC.2004.837539.
- [161] S. Tarbouriech, M. Turner, "Anti-windup design: An overview of some recent advances and open problems", *IET Control Theory & Applications*, vol. 3, no. 1, pp. 1-19, Jan. 2009.

- [162] Q. -C. Zhong and G. C. Konstantopoulos, "Current-Limiting Droop Control of Grid-Connected Inverters," *IEEE Transactions on Industrial Electronics*, vol. 64, no. 7, pp. 5963-5973, July 2017, doi: 10.1109/TIE.2016.2622402.
- [163] G. C. Konstantopoulos, Q. Zhong and W. Ming, "PLL-Less Nonlinear Current-Limiting Controller for Single-Phase Grid-Tied Inverters: Design, Stability Analysis, and Operation Under Grid Faults," *IEEE Transactions on Industrial Electronics*, vol. 63, no. 9, pp. 5582-5591, Sept. 2016, doi: 10.1109/TIE.2016.2564340.
- [164] H. K. Khalil, *Nonlinear Systems*, Upper Saddle River, NJ, USA: Prentice Hall.
- [165] Qing-Chang Zhong; Tomas Hornik, "Preliminaries," *Control of Power Inverters in Renewable Energy and Smart Grid Integration*, IEEE, 2012, pp.63-78, doi: 10.1002/9781118481806.ch2.
- [166] R. Teodorescu, M. Liserre, and P. Rodriguez, *Grid Converters for Photovoltaic and Wind Power Systems*, Chichester, West Sussex, UK:Wiley, 2011.
- [167] G. C. Konstantopoulos, Q. -C. Zhong, B. Ren and M. Krstic, "Bounded Integral Control of Input-to-State Practically Stable Nonlinear Systems to Guarantee Closed-Loop Stability," *IEEE Transactions on Automatic Control*, vol. 61, no. 12, pp. 4196-4202, Dec. 2016, doi: 10.1109/TAC.2016.2552978.
- [168] M. Ashabani, F. D. Freijedo, S. Golestan and J. M. Guerrero, "Inducverters: PLL-Less Converters with Auto-Synchronization and Emulated Inertia Capability," *IEEE Transactions on Smart Grid*, vol. 7, no. 3, pp. 1660-1674, May 2016, doi: 10.1109/TSG.2015.2468600.
- [169] N. Jaalam, N. A. Rahim, A. H. A. Bakar, C. K. Tan, and A. M. A. Haidar, "A comprehensive review of synchronization methods for grid-connected converters of renewable energy source," *Renewable and Sustainable Energy Reviews*, vol. 59, pp. 1471-1481, 2016, doi: 10.1016/j.rser.2016.01.066.
- [170] F. Blaabjerg, R. Teodorescu, M. Liserre and A. V. Timbus, "Overview of Control and Grid Synchronization for Distributed Power Generation Systems," *IEEE Transactions on Industrial Electronics*, vol. 53, no. 5, pp. 1398-1409, Oct. 2006, doi: 10.1109/TIE.2006.881997.
- [171] Q. Zhong and G. C. Konstantopoulos, "Current-Limiting Three-Phase Rectifiers," *IEEE Transactions on Industrial Electronics*, vol. 65, no. 2, pp. 957-967, Feb. 2018, doi: 10.1109/TIE.2017.2696483.

- [172] X. Meng, J. Liu and Z. Liu, "A Generalized Droop Control for Grid-Supporting Inverter Based on Comparison Between Traditional Droop Control and Virtual Synchronous Generator Control," *IEEE Transactions on Power Electronics*, vol. 34, no. 6, pp. 5416-5438, June 2019, doi: 10.1109/TPEL.2018.2868722.
- [173] S. A. Khajehoddin, M. Karimi-Ghartemani and M. Ebrahimi, "Grid-Supporting Inverters with Improved Dynamics," *IEEE Transactions on Industrial Electronics*, vol. 66, no. 5, pp. 3655-3667, May 2019, doi: 10.1109/TIE.2018.2850002.
- [174] J. W. Simpson-Porco, F. Dörfler and F. Bullo, "Voltage Stabilization in Microgrids via Quadratic Droop Control," *IEEE Transactions on Automatic Control*, vol. 62, no. 3, pp. 1239-1253, March 2017, doi: 10.1109/TAC.2016.2585094.
- [175] P. Piya, M. Ebrahimi, M. Karimi-Ghartemani and S. A. Khajehoddin, "Fault Ride-Through Capability of Voltage-Controlled Inverters," *IEEE Transactions on Industrial Electronics*, vol. 65, no. 10, pp. 7933-7943, Oct. 2018, doi: 10.1109/TIE.2018.2803765.
- [176] X. Zhao, J. M. Guerrero, M. Savaghebi, J. C. Vasquez, X. Wu and K. Sun, "Low-Voltage Ride-Through Operation of Power Converters in Grid-Interactive Microgrids by Using Negative-Sequence Droop Control," *IEEE Transactions on Power Electronics*, vol. 32, no. 4, pp. 3128-3142, April 2017, doi: 10.1109/TPEL.2016.2570204.
- [177] Y. Yang, F. Blaabjerg and H. Wang, "Low-Voltage Ride-Through of Single-Phase Transformerless Photovoltaic Inverters," *IEEE Transactions on Industry Applications*, vol. 50, no. 3, pp. 1942-1952, May-June 2014, doi: 10.1109/TIA.2013.2282966.
- [178] M. S. El Moursi, W. Xiao and J. L. Kirtley, "Fault ride through capability for grid interfacing large scale PV power plants," *IET Generation, Transmission & Distribution*, vol. 7, no. 9, pp. 1027-1036, Sept. 2013.
- [179] D. Groß and F. Dörfler, "Projected grid-forming control for current-limiting of power converters," *2019 57th Annual Allerton Conference on Communication, Control, and Computing (Allerton)*, 2019, pp. 326-333, doi: 10.1109/ALLERTON.2019.8919856.
- [180] S. Acharya, M. S. El-Moursi, A. Al-Hinai, A. S. Al-Sumaiti and H. H. Zeineldin, "A Control Strategy for Voltage Unbalance Mitigation in an Islanded Microgrid

- Considering Demand Side Management Capability," *IEEE Transactions on Smart Grid*, vol. 10, no. 3, pp. 2558-2568, May 2019, doi: 10.1109/TSG.2018.2804954.
- [181] G. C. Konstantopoulos and P. R. Baldivieso-Monasterios, "State-limiting PID controller for a class of nonlinear systems with constant uncertainties," *International Journal of Robust and Nonlinear Control*, vol. 30, no. 5, pp. 1770–1787, 2020.
- [182] A. T. Alexandridis, "Studying state convergence of input-to-state stable systems with applications to power system analysis," *Energies*, vol. 13, no. 1, Dec. 2019, Art.no. 92.
- [183] IEEE Recommended Practice and Requirements for Harmonic Control in Electric Power Systems," *IEEE Std 519-2014 (Revision of IEEE Std 519-1992)*, June 2014, doi: 10.1109/IEEESTD.2014.6826459.
- [184] M. Liserre, F. Blaabjerg and S. Hansen, "Design and control of an LCL-filter-based three-phase active rectifier," *IEEE Transactions on Industry Applications*, vol. 41, no. 5, pp. 1281-1291, Sept.-Oct. 2005, doi: 10.1109/TIA.2005.853373.
- [185] S. Dedeoglu, G. C. Konstantopoulos and H. Komurcugil, "Current-Limiting VSG for Renewable Energy Applications," *2021 IEEE 30th International Symposium on Industrial Electronics (ISIE)*, 2021, pp. 01-05, doi: 10.1109/ISIE45552.2021.9576298.
- [186] S. Dedeoglu, G. C. Konstantopoulos and H. Komurcugil, "Current-limiting Virtual Synchronous Control and Stability Analysis Considering DC-link Dynamics Under Normal and Faulty Grid Conditions," *IEEE Journal of Emerging and Selected Topics in Power Electronics*, doi: 10.1109/JESTPE.2021.3103830.
- [187] L. Huang, H. Xin, H. Yang, Z. Wang and H. Xie, "Interconnecting Very Weak AC Systems by Multiterminal VSC-HVDC Links with a Unified Virtual Synchronous Control," *IEEE Journal of Emerging and Selected Topics in Power Electronics*, vol. 6, no. 3, pp. 1041-1053, Sept. 2018, doi: 10.1109/JESTPE.2018.2825391.
- [188] I. Sefa, S. Ozdemir, H. Komurcugil, and N. Altin, "Comparative study on Lyapunov-function-based control schemes for single-phase grid-connected voltage-source inverter with LCL filter," *IET Renewable Power Generation*, vol. 11, no. 11, pp. 1473–1482, 2017, doi: 10.1049/iet-rpg.2016.0566.

- [189] F. Dörfler, S. Bolognani, J. W. Simpson-Porco and S. Grammatico, "Distributed Control and Optimization for Autonomous Power Grids," *2019 18th European Control Conference (ECC)*, 2019, pp. 2436-2453, doi: 10.23919/ECC.2019.8795974.
- [190] D. Pan, X. Wang, F. Liu and R. Shi, "Transient Stability of Voltage-Source Converters with Grid-Forming Control: A Design-Oriented Study," *IEEE Journal of Emerging and Selected Topics in Power Electronics*, vol. 8, no. 2, pp. 1019-1033, June 2020, doi: 10.1109/JESTPE.2019.2946310.
- [191] Z. Shuai, C. Shen, X. Liu, Z. Li and Z. J. Shen, "Transient Angle Stability of Virtual Synchronous Generators Using Lyapunov's Direct Method," *IEEE Transactions on Smart Grid*, vol. 10, no. 4, pp. 4648-4661, July 2019, doi: 10.1109/TSG.2018.2866122.
- [192] M. G. Taul, X. Wang, P. Davari and F. Blaabjerg, "Current Limiting Control with Enhanced Dynamics of Grid-Forming Converters During Fault Conditions," *IEEE Journal of Emerging and Selected Topics in Power Electronics*, vol. 8, no. 2, pp. 1062-1073, June 2020, doi: 10.1109/JESTPE.2019.2931477.
- [193] T. Qoria, F. Gruson, F. Colas, G. Denis, T. Prevost and X. Guillaud, "Critical Clearing Time Determination and Enhancement of Grid-Forming Converters Embedding Virtual Impedance as Current Limitation Algorithm," *IEEE Journal of Emerging and Selected Topics in Power Electronics*, vol. 8, no. 2, pp. 1050-1061, June 2020, doi: 10.1109/JESTPE.2019.2959085.
- [194] L. Zhou et al., "Harmonic Current and Inrush Fault Current Coordinated Suppression Method for VSG Under Non-ideal Grid Condition," *IEEE Transactions on Power Electronics*, vol. 36, no. 1, pp. 1030-1042, Jan. 2021, doi: 10.1109/TPEL.2020.3000522.
- [195] A. -C. Braiton, G. C. Konstantopoulos and V. Kadiramanathan, "Current-Limiting Droop Control Design and Stability Analysis for Paralleled Boost Converters in DC Microgrids," *IEEE Transactions on Control Systems Technology*, vol. 29, no. 1, pp. 385-394, Jan. 2021, doi: 10.1109/TCST.2019.2951092.
- [196] S. Dedeoglu and G. C. Konstantopoulos, "Avoiding Circulating Current via Current-Limiting Control in AC Microgrids with Parallel Three-Phase Inverters," *IECON 2021 - 47th Annual Conference of the IEEE Industrial Electronics Society*, 2021, to be published.

- [197] G. C. Konstantopoulos, Q. C. Zhong, B. Ren, and M. Krstic, "Bounded droop controller for parallel operation of inverters," *Automatica*, vol. 53, pp. 320–328, 2015, doi: 10.1016/j.automatica.2015.01.012.
- [198] M. Zhang, B. Song and J. Wang, "Circulating Current Control Strategy Based on Equivalent Feeder for Parallel Inverters in Islanded Microgrid," *IEEE Transactions on Power Systems*, vol. 34, no. 1, pp. 595-605, Jan. 2019, doi: 10.1109/T-PWRS.2018.2867588.
- [199] P. Prabhakaran, Y. Goyal and V. Agarwal, "Novel Nonlinear Droop Control Techniques to Overcome the Load Sharing and Voltage Regulation Issues in DC Microgrid," *IEEE Transactions on Power Electronics*, vol. 33, no. 5, pp. 4477-4487, May 2018, doi: 10.1109/TPEL.2017.2723045.
- [200] B. M. Eid, N. A. Rahim, J. Selvaraj and A. H. El Khateb, "Control Methods and Objectives for Electronically Coupled Distributed Energy Resources in Microgrids: A Review," *IEEE Systems Journal*, vol. 10, no. 2, pp. 446-458, June 2016, doi: 10.1109/JSYST.2013.2296075.
- [201] M. Ganjian-Aboukheili, M. Shahabi, Q. Shafiee and J. M. Guerrero, "Seamless Transition of Microgrids Operation From Grid-Connected to Islanded Mode," *IEEE Transactions on Smart Grid*, vol. 11, no. 3, pp. 2106-2114, May 2020, doi: 10.1109/TSG.2019.2947651.
- [202] X. Meng, X. Liu, M. He, Z. Liu and J. Liu, "A Self-Adaptive Controller for Inverter with Seamless Transfer and Automatic Pre-Synchronization Capability," *IEEE Access*, vol. 8, pp. 105936-105949, 2020, doi: 10.1109/ACCESS.2020.3000268.
- [203] M. N. Arafat, A. Elrayyah and Y. Sozer, "An Effective Smooth Transition Control Strategy Using Droop-Based Synchronization for Parallel Inverters," *IEEE Transactions on Industry Applications*, vol. 51, no. 3, pp. 2443-2454, May-June 2015, doi: 10.1109/TIA.2014.2369826.
- [204] W. Issa, M. Abusara, S. Sharkh and T. Mallick, "A small signal model of an inverter-based microgrid including DC link voltages," *2015 17th European Conference on Power Electronics and Applications (EPE'15 ECCE-Europe)*, 2015, pp. 1-10, doi: 10.1109/EPE.2015.7309119.

- [205] W. R. Issa, M. A. Abusara and S. M. Sharkh, "Control of Transient Power During Unintentional Islanding of Microgrids," *IEEE Transactions on Power Electronics*, vol. 30, no. 8, pp. 4573-4584, Aug. 2015, doi: 10.1109/TPEL.2014.2359792.